Low Noise, Low Power Interface Circuits and Systems for High Frequency Resonant Micro-Gyroscopes

A Dissertation
Presented to
The Academic Faculty

By

Milap Dalal

In Partial Fulfillment
Of the Requirements for the Degree
Doctor of Philosophy in the
School of Electrical and Computer Engineering

Georgia Institute of Technology

August 2012

Low Noise, Low Power Interface Circuits and Systems for High Frequency Resonant Micro-Gyroscopes

Approved by:

Professor Farrokh Ayazi, Advisor
School of Electrical and Computer Engineering
Georgia Institute of Technology

Professor Mark Allen, Co-Advisor
School of Electrical and Computer Engineering
Georgia Institute of Technology

Professor Jennifer Hasler
School of Electrical and Computer Engineering
Georgia Institute of Technology

Professor Maysam Ghovanloo
School of Electrical and Computer Engineering
Georgia Institute of Technology

Professor Pamela Bhatti
School of Electrical and Computer Engineering
Georgia Institute of Technology

Professor Paul Kohl
School of Chemical and Biomolecular Engineering
Georgia Institute of Technology

Date Approved:

06/21/2012

I dedicate this dissertation to my incredible family and friends for their never-ending support, understanding, love, and patience.

ACKNOWLEDGMENTS

I would like to express my appreciation and gratitude to my advisor, Professor Farrokh Ayazi for his guidance and support. I have been honored to work and learn under his supervision throughout my PhD.

I would also like to thank my co-advisor, Professor Mark Allen, and my dissertation defense committee members - Professors Jennifer Hasler, Maysam Ghovanloo, Pamela Bhatti and Paul Kohl for their interest in my work.

This research would not have been possible without the support of my many esteemed colleagues in the Integrated MEMS Laboratory, both past and present. I wish to thank Drs. Houri Johari, Krishna Sundaresan, Reza Abdolvand, and Ajit Sharma for their valuable guidance and direction during my first years as a research assistant, and Jalpa Shah, Dr. Mauricio Pardo, Jenna Fu, Xin Gao, Dr. Ashwin Samarao, Aditi Dutt Chaudhuri, Wang-Kyung Sung, Diego Serrano, Roozbeh Tabrizian, Logan Sorenson, Yaesuk Jeong, Arashk N.-Shirazi, Peng Shao, Mojtaba Hodjat-Shamami, Pantani Liu, Nishanth Mehanathan, and Drs. Wanling Pan and Giorgio Casinovi for all their help during those middle and final years.

Part of the research funding for this thesis was provided by Qualtré, Inc. This work was also supported in part by DARPA under contract #W31P4Q-12-1-0004. I would also like to thank the MOSIS Education Program and TSMC for providing IC fabrication support.

Last but not least, I'd like to thank you, the reader, for giving this thesis its purpose.

TABLE OF CONTENTS

LIST OF TABLES

LIST OF FIGURES

SUMMARY

Micromachined gyroscopes comprise one of the fastest growing segments of the MEMS sensor market. With the integration of gyroscopes and other inertial sensors into mobile hardware combined with the development of new applications for these MEMS devices, the demand for gyroscopes is expected to grow quickly over the next several years. However, as the needs for short-range navigation, gaming, and motion control become more sophisticated, devices must perform equal to or better than previous commercial-grade gyroscopes while reducing sensor cost, power, and size of the sensor. Furthermore, the growth of the MEMS industry has led to a strong push toward developing gyroscopes and inertial sensors than can realize both the small form factor and high-yield wafer-level fabrication of MEMS devices while providing ultra-high navigation-grade system performance.

Today's state-of-the-art rate vibratory gyroscopes use a large proof mass that vibrates at a low resonance frequency (3-30 kHz). At these frequencies, a performance tradeoff is created in which a rate vibratory gyroscope can either offer a large bandwidth (mode-split) or a high resolution (mode-matched), but not both without increasing the mass (and size) of the gyroscope. Consequently, it becomes difficult to maintain the same level of performance while scaling down the device size.

Recently, it was proposed that increasing the operating frequencies of the drive and sense modes of the gyroscope by several orders of magnitude could minimize the mechanical noise of the gyroscope and concurrently maintain a large sensor bandwidth.

This led to the development of the capacitive bulk acoustic wave (BAW) silicon disk gyroscope, a new class of micromachined rate vibratory gyroscopes operating in the frequency range of 1-10MHz with high device bandwidth and shock/vibration tolerance. By scaling the frequency into the MHz regime, BAW gyroscopes are able to provide low mechanical noise without sacrificing the high bandwidth performance required for commercial applications. Additionally, the drive loop of the BAW gyroscope can also be exploited as a timing device that can be integrated in existing commercial systems to provide competitive clock performance to the state-of-the-art using less area and power. This clock can also be used as a timing device for integrated timing + inertial measurement units (TIMUs) to reduce the power consumption of the complete system and noise of the individual sensors.

Although the BAW gyroscope provides significant improvement to sensor bandwidth, shock tolerance, and mechanical noise performance, the high frequency of the BAW gyroscope also creates a larger power demand from the interface electronics. At the same time, the reduction of mechanical noise in high frequency gyroscopes and the push for small, low power gyroscopes with high performance (navigation-grade) shifts the burden of noise minimization from the mechanical element to the interface circuitry.

This dissertation discusses the design and implementation of a CMOS ASIC architecture that interfaces with a high-Q, wide-bandwidth BAW gyroscope and the challenges associated with optimizing the noise performance to achieve navigation-grade levels of sensitivity as the frequency is scaled into the MHz regime. The dissertation begins with an overview of the BAW device and an outline of how the device is fabricated. Mathematical models are derived to describe the operation of the sensor and

are used to generate equivalent electrical circuit models of the gyroscope. A design strategy is then outlined for the ASIC to optimize the drive loop and sense channel for power and noise, and steps toward reducing this noise as the system is pushed to navigation-grade performance are presented that maintain optimum system power consumption.

After analyzing the BAW gyroscope and identifying a strategy for developing the drive and sense interface circuitry, a complete fully-differential ASIC is designed in 0.18μm CMOS to interface with a bulk acoustic wave (BAW) disk gyroscope. As an oscillator, the gyroscope provides an uncompensated clock signal at ~9.64 MHz with a temperature sensitivity of -27 ppm/°C and phase noise of -104 dBc at 1 kHz from carrier. Unlike other gyroscopes, the high frequency and low phase noise of the BAW disk gyroscope drive loop along with its immunity to rate-induced frequency variation allow exploitation of this signal for use on mobile and TIMU platforms, making this sensor ideal for implementation as hybrid rotation sensor + timing device.

To measure rate, a fully-differential sense channel is implemented for the ASIC that incorporates a quadrature compensation technique that allows for continuous-time cancellation of the quadrature component of the input sense current. When the complete ASIC is interfaced with the gyroscope, the sensor shows a measured rate sensitivity of 1.15 mV/^{o}/s with an open-loop bandwidth of 280 Hz and a bias instability of 0.095 ^{o}/s, suitable for the rate-grade performance commonly required for commercial and consumer electronics applications. The system is recorded to have a total power of 1.6 mW and a total area of 0.64 mm^2.

Following the design of the interface ASIC, discussion is provided on the development of CMOS charge pumps for MEMS gyroscopes and other capacitive devices. This dissertation investigates in further detail the requirements for designing and optimizing charge pumps for capacitive MEMS devices. Basic charge pump design is outlined, followed by an overview of techniques that can be used in smaller processes to generate larger polarization voltages from the ASIC.

To complete this thesis, an alternate measurement technique for measuring the rotation rate of the gyroscope is discussed. This technique is based on the phase-shift modulation of the gyroscope output signal when the device is driven with two orthogonal signal inputs and can be easily modified to provide either linear rotation scale factor measurement or a linear calibration curve that can be used to track and adjust the variation of the sensor scale factor over time. The advantages and disadvantages of this scheme over conventional amplitude-modulated readout are outlined and compared, followed by an overview of the calibration technique and a comparison of how closely the calibration measurement tracks the phase-shift readout measurement. Finally, the contributions of this work are outlined, and an overview of future work needed to develop the state-of-the-art is presented.

CHAPTER 1

INTRODUCTION

A gyroscope (Fig. 1-1) is a sensor that measures the rate or orientation of a system. Along with accelerometers, gyroscopes fall under a class of instruments known as inertial sensors [1], which are used to detect and measure any change in a system's state of motion or rest. In the last several years, research and development of these sensors has undergone a renaissance due in large part to two major developments – the explosion of the consumer market for inertial sensors, and strong interest in realizing high-performance devices using MEMS (micro-electromechanical systems) technology.

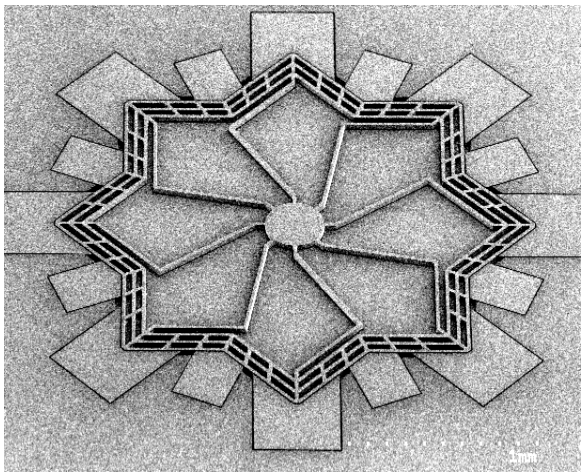

Figure 1-1 – SEM of a MEMS multi-shell resonating star gyroscope [2].

1.1. Applications and Market Demand

Compared to the previous generation of macro-gyroscopes, the benefits of wafer-level batch fabrication and economies of scale have made MEMS gyroscopes and inertial sensors available at a significantly smaller size and lower cost, creating new potentials for

integrating these devices into a variety of novel systems. Consequently, the demand for MEMS gyroscopes has grown significantly in consumer and industrial markets (Fig 1-2). Between 2009-2015, the demand for inertial sensors is expected to grow from $1B to $3.6B [3]. Furthermore, the market for gyroscopes alone is expected to triple from $201M to $722M by 2015, making them one of the largest MEMS products sold commercially today.

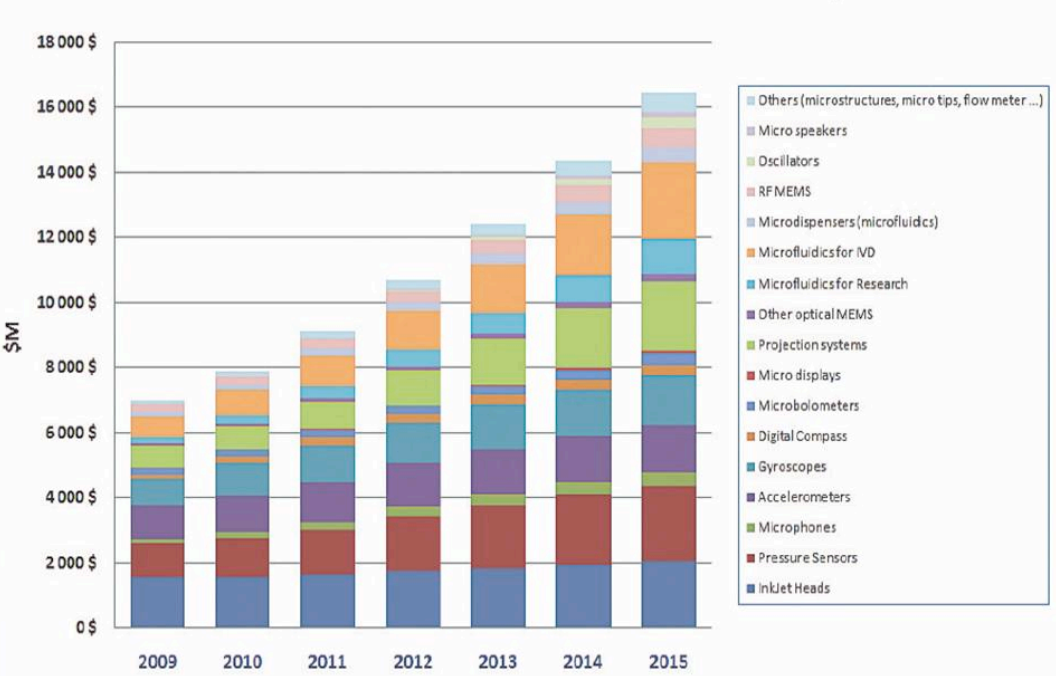

Figure 1-2 – MEMS market forecast, 2009-2015 (in millions) [3].

In recent years, MEMS inertial sensors have benefited from the emergence of gaming and mobile communication platforms, which use the image stabilization, GPS-assisted positioning and navigation, and motion-based functionality offered by 6 DOF inertial measurement units (IMUs) to expand or improve system performance. Due to the heavy competition in these fields, new features and designs are continuously introduced to maintain one product's advantage over its market competitors. However, these modifications cannot compromise the aesthetics or performance of previous generations

of the platform by making it slower, bulkier, or considerably more expensive. Thus, it becomes necessary to reduce the size of each component - the microprocessor, gyro/IMU, battery (if possible), etc – to integrate newer or better technologies into the platform.

In addition to commercial development, the significant cost and size advantages provided by micro-machined rate vibratory gyroscopes have created a strong push toward developing lightweight, low power, MEMS-based navigation-grade sensors. In 2010, the Defense Advanced Research Projects Agency (DARPA) launched the micro-PNT program, which focuses on the development of micro-machined instruments that can be used for precision position, navigation, and timing (PNT) systems [4]. The program seeks novel device fabrication, circuit design, and system integration techniques for "self-contained, chip-scale inertial navigation and precision guidance [4]," with a goal to realize this objective by 2015. If successful, these micro-machined, navigation-grade sensors will open new applications for precision gyroscopes, including dismounted-soldier navigation and navigation of unmanned air and water vehicles.

1.2. MEMS Vibratory Gyroscopes

Most MEMS gyroscopes are classified as MEMS vibratory gyroscopes. Unlike other gyroscope classifications (i.e. optical and mechanical gyroscopes), vibratory gyroscopes do not require any rotating parts and therefore lend themselves well to micron-level miniaturization [5]. MEMS vibratory gyroscopes can be divided into two classes – rate vibratory gyroscopes, which measure the rotation rate of the system, and angular vibratory gyroscopes [6], which directly measure the orientation angle of the device. Although it is possible to achieve high levels of performance using either device, this

thesis will focus exclusively on the development and characterization of high frequency rate vibratory gyroscopes.

MEMS rate vibratory gyroscopes (also referred to as Coriolis rate vibratory gyroscopes, or CVGs) operate based on a principle of Coriolis acceleration, which states that when an object moving (vibrating) in an inertial reference plane is rotated along a second plane, a deflection in motion (acceleration) that is orthogonal to both the axes of vibration and rotation [7] can be measured by a stationary observer. This acceleration can be characterized by

$$\vec{a}_{Coriolis} = 2\vec{v} \times \vec{\Omega} \qquad (1\text{-}1)$$

where v represents the velocity of the inertial reference plane and Ω represents the angular velocity of the rotating system (rate). With CVGs, the vibratory mode that sets v is known as the drive mode, while the secondary mode that is orthogonal to both the drive mode and the axis of rotation and observes the Coriolis signal is referred to as the sense mode.

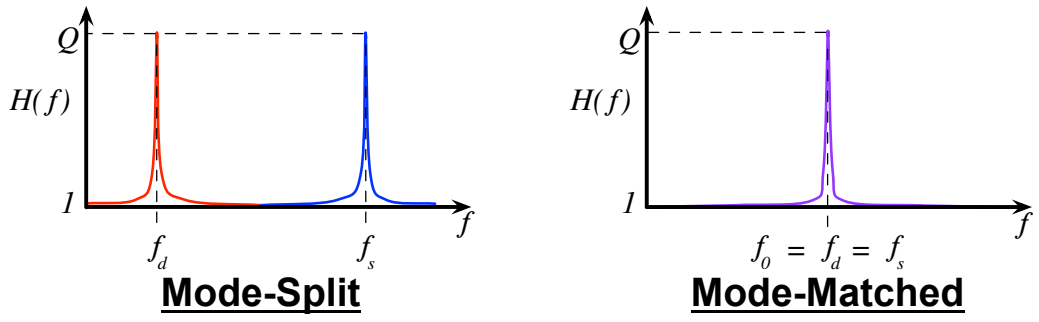

Figure 1-3 – Mode-split versus mode-matched operating modes of vibratory gyroscopes.

Depending on the design, rate vibratory gyroscopes can measure rate through either mode-split [8] or mode-matched [9] operation (Fig. 1-3). In mode-split operation, the resonant sense mode (f_s) of the gyroscope operates at a different frequency than the drive

mode (f_d) [10]. Because the two modes are separated (unmatched), the sense mode acts as an accelerometer and measures a change in displacement when a Coriolis force is applied. Using this methodology, there is a low net transfer of energy between the two modes when a Coriolis force is applied, resulting in a low effective quality factor (Q_{eff}) of the gyroscope. The quality factor can be defined as a measure of the spectral purity of a resonator, characterized by

$$Q = \frac{f_0}{\Delta f} \tag{1-2}$$

where f_0 and Δf represent the frequency and 3-dB bandwidth of the resonance peak, respectively. In a mode-matched gyroscope, the sense and drive modes are designed to operate at the same frequency, giving the sensor Q_{eff}-times higher rotation sensitivity over mode-split gyroscopes [11, 12]. However, because the drive and sense peaks must be matched, the bandwidth of the gyroscope is attenuated. This is a major bottleneck for low-frequency gyroscopes (Table 1-2), as the sensor cannot offer high sensitivity angular rate sensing at low operating frequencies without significantly compromising its operating bandwidth.

1.3. Performance Specifications

Gyroscopes are placed into one of three categories that are defined by the classification criteria presented in Table 1-1. These categories are referred to as rate-grade, tactical-grade, and navigation-grade, respectively. Rate-grade gyroscopes represent devices used in consumer electronics, including digital cameras, gaming and robotic systems [1], and mobile platforms. Higher-end systems used in industrial and healthcare applications require tactical-grade gyroscopes [13, 14]. These applications include gyrocompassing for commercial sea-, land- or air-craft and high-resolution

sensors for medical instrumentation. Inertial- or navigation-grade gyroscopes are typically used for space/defense applications, including missile guidance and vehicle/platform stabilization, which require gyroscopes with ultra-high sensitivity and resolution to minimize positioning error. Tactical- and navigation-grade gyroscopes can also be integrated with high-end accelerometers to form IMUs – 6 degree of freedom (DOF) inertial sensors capable of determining the position of an object based on its speed and movement from a given point over a fixed period of time (dead reckoning). When equipped with a processing unit, IMUs and other multi-DOF inertial sensors can be used for pedestrian and in-door navigation [12], as well as GPS-assisted or GPS-independent positioning for military-guidance systems.

Table 1-1 – Performance requirements for different classes of gyroscopes [3]

Parameter	Rate Grade	Tactical Grade	Inertial (Navigation) Grade
Angle Random Walk ($°/\sqrt{hr}$)	> 0.5	0.5 – 0.05	< 0.001
Bias Drift ($°/hr$)	10 – 1000	0.1 – 10	< 0.01
Scale Factor Accuracy ($\%$)	0.1 – 1	0.01 – 0.1	< 0.001
Full Scale Range ($°/s$)	50 – 1000	> 500	> 400
Max. Shock in 1ms (g)	10^3	$10^3 – 10^4$	$10^3 – 10^4$
Bandwidth (Hz)	> 70	~ 100	~ 100

As stated previously, several performance metrics are tested and measured to characterize the sensor and classify its performance as rate-grade, tactical-grade, or navigation-grade. The following sub-sections explain each parameter in detail.

1.3.1. Resolution

Resolution quantifies the minimum attainable signal that can be distinguished from the total noise equivalent rotation (TNEΩ) of the complete sensor (i.e. the gyroscope integrated with interface electronics), which is given by

$$TNE\Omega = \sqrt{MNE\Omega^2 + ENE\Omega^2} \tag{1-3}$$

MNEΩ and ENEΩ describe the mechanical noise equivalent rotation and electrical noise equivalent rotation, respectively. The MNEΩ is given by

$$MNE\Omega = \frac{1}{q_{drive}} \sqrt{\frac{4k_B T(BW)}{\omega_0 M Q_{eff}}} \tag{1-4}$$

where q_{drive}, k_B, T, ω_0, M, and Q_{eff} are the drive amplitude, Boltzmann's constant, temperature, mass, resonance frequency, and mode-matched Q, respectively. The ENEΩ is given by

$$ENE\Omega = \frac{M d_0^2 \omega_0^2}{2 v_{ac} V_P^2 C_{s0}^2 Q_{eff}^2} I_{noise} \sqrt{BW} \tag{1-5}$$

where d_0, v_{ac}, V_P, C_{s0} and I_{noise} are respectively the sense gap size (at rest), AC drive voltage, polarization voltage, sense capacitance, and input noise current. In order to minimize TNEΩ, the gyroscope should operate with high Q_{eff} (through mode-matched operation) at a frequency where MNEΩ and ENEΩ are equal.

Although not directly listed as a performance specification in Table 1-2, resolution is critical to gyroscope performance. Poor resolution indicates the Coriolis signal cannot be easily distinguished from the noise floor, which affects several metrics. Two of these affected metrics are angle random walk and bias drift.

1.3.1.1. Angle Random Walk

Angle random walk (ARW) describes the average error measured when the rate signal is integrated to track the angle changes of an object (i.e. angle error) [15]. ARW stems from the fact that the white noise present in the rate output has a non-zero mean when integrated over a fixed time interval, even when the gyroscope is at rest.

Consequently, the white noise adds a random component to the angle calculation that increases linearly with the square root of time and cannot be corrected for. Angle random walk and bias drift are typically determined by performing an Allan variance measurement – a well-known method of characterizing and identifying the noise in frequency-based sensors [16]. Additional information on Allan variance measurement and analysis is provided in Appendix B. Angle random walk is typically measured in °/√hr.

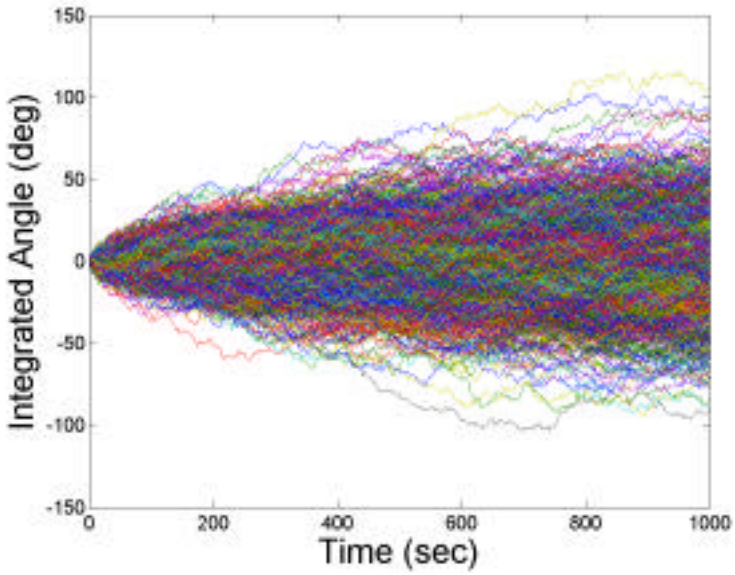

Figure 1-4 – Increase in integrated angle error over time [17].

ARW is an important measure of performance for dead-reckoning navigation and positioning systems because it determines how much larger the error generated from rate integration and angle calculation of the sensor becomes with time (Fig. 1-4). This error increases the deviation between an object's calculated and actual position, which can cause critical problems (particularly for military systems). This error is difficult to minimize through gyro performance alone, as systems using navigation-grade gyroscopes can only reduce position uncertainty to within ~1800km after 1 hour of navigation.

Consequently, new techniques to reduce angle error by reducing integration time through continuous sensor calibration are being researched and developed. These techniques are discussed in Chapter 6.

1.3.1.2. Bias Drift (Bias Instability)

The bias drift of the gyroscope typically refers to the long-term stability of the sensor. It is composed of both systematic components, such as temperature variation and linear acceleration/vibration [18], and noise components subject to random flickering, such as *1/f* noise. The bias drift value extracted from an Allan variance curve represents the best resolution that particular gyroscope can achieve. It is typically measured in °/hr.

1.3.2. Scale Factor and Scale Factor Accuracy

The scale factor of a gyroscope is defined as the ratio between the change in the sensor output voltage to a change in the applied input stimulus (i.e. rotation rate). With analog CVGs, this ratio is expressed as $\frac{V}{^{\circ}/s}$. Scale factor is generally evaluated as the slope of the straight line that can be fitted by the method of least squares to the input-output data [18]. It is dependent upon two factors – the sensitivity of the gyroscope to the applied Coriolis signal and the gain of the interface electronics. If too large a signal is applied or the IC provides too high a gain, the output will saturate or become non-linear. Therefore, it is equally important to characterize the scale factor accuracy (linearity), which is determined by comparing the measured output of each applied rate signal to what is predicted by the line of best fit.

1.3.3. Full-Scale Range (FSR)

Full-scale range refers to the range of input values over which the output is detectable. It is often used to measure the sensor dynamic range by calculating the ratio

between the FSR and the system noise floor. A large variation in the upper and lower detection range is important for systems that sense human motion (i.e. gaming) to capture a broad set of possible movements from the user [12].

There is often some tradeoff between full-scale range and scale factor, as a sensor with a larger scale factor will saturate more quickly and therefore not have as large a FSR as a sensor with a smaller scale factor. However, the FSR can be significantly improved if a closed-loop readout of the sense mode is implemented, in which the Coriolis force is measured by comparing it with an external feedback force [19]. A wide dynamic range in a low-noise gyroscope is highly desirable as it allows the use of a single device with a high level of stability in a broader array of applications, ranging from gaming to navigation [12].

1.3.4. Shock Tolerance

Shock tolerance (measured in *g*) refers to how well the sensor can perform when an outside perturbation is introduced. In the case of gyroscopes and other inertial sensors, the perturbation comes in the form of pressure/acceleration and may be a result of either the operating environment of the sensor or the end-user handling the device. Gyroscopes with a high shock tolerance are a basic requirement for many high-end applications, particularly with military- and space-related systems.

1.3.5. Bandwidth

The bandwidth of a gyroscope determines the response (settling) time of the sensor or the time required for the output to settle to within a certain range of the expected value for an input step function. The bandwidth is given by (1-2), which indicates that a gyroscope with a high Q_{eff} (high resolution) will have a small operating bandwidth.

For rate-grade, tactical-grade, and inertial grade applications, the tradeoff between resolution and bandwidth is a significant issue. Mode-split gyroscopes can offer a large bandwidth, but their low Q makes the Coriolis signal hard to detect above the noise floor, indicating poor resolution. Conversely, traditional–mode-matched gyroscopes have very good resolution due to the benefits of Q-amplification, but at the same time their bandwidth is attenuated because of the small 3-dB bandwidth of the resonance peak.

Table 1-2 presents a list of the current state-of-the-art commercial vibratory gyroscopes and their performance specifications. Currently, MEMS gyroscopes do not meet the ultra-stringent requirements demanded for navigation-grade performance. The noise and bias drift of these gyros result in fast-growing errors in computed orientation, which do not allow for extended periods of navigation critical for most space and defense systems [12].

Table 1-2 – Commercial specifications of state-of-the-art gyroscopes [3]

	LYPR540AH	L3G4200D	MPU6000 /MPU6050	ADXRS453	SMG061	KGY13
Manufacturer	ST Micro	ST Micro	Invensense	ADI	Bosch	Kionix
Max. Sensitivity	3.2[1]	70[2]	131[3]	80[3]	7[1]	5.85[1]
Max. Scale Factor (°/*s*)	1600	2000	2000	±400	±240	±256
Scale Factor Accuracy (*%*)	±1	±2	0.2	±3	±7	±1
Bias Instability (°/*hr*)	-	-	-	16	-	-
Bandwidth (*Hz*)	140	100-800	-	77.5	30	10
Power (*mW*)	32.4	18.3	16.5	19.8	33	18.6
Size (mm^3)	33	17.6	-	320	1047.1	22.5
Degrees-of-Freedom	3-Axis	3-Axis	6-Axis	Z-Axis Only	X-Axis Only	3-Axis
Reference	[8]	[20]	[21]	[22]	[23]	[24]
[1] mV/°/s		***[2] mdegree/s/digit***			***[3] LSB/°/s***	

Realizing a navigation-grade IMU involves significant reduction in the noise contribution from both the mechanical and electrical components of the gyroscope and

accelerometer. The addition of a timing component brings into focus the concept of sensor fusion, in which the sensory and timing data collected from each component of the chipscale IMU with timing (TIMU) can be used to improve the signal quality and overall performance of the individual sensors while reducing the power cost of the entire system. The presence of a high-frequency clock allows multiplexing of the output acceleration and rate signals to reduce system power, and can also be used to digitize and (Kalman) filter each respective signal to reduce the noise of each output signal. Furthermore, the acceleration and rotation data taken from the accelerometer and gyroscope, respectively, can be used to suppress vibration and acceleration or rotation sensitivity from the other components of the TIMU platform.

1.4. Motivation

As discussed throughout this chapter, a broad set of performance criteria are used to qualify gyroscopes for rate-, tactical-, and navigation-grade applications. These criteria have become even more stringent with the rapid growth of gaming and mobile platforms that have pushed the next-generation of rate-grade gyroscopes to become even smaller and cheaper without compromising their performance. Current state-of-the-art rate vibratory gyroscopes use a large mass that vibrates at a low resonance frequency (kHz). From (1-3) and (1-4), it can be determined that the low frequency of resonance results in a high mechanical noise floor, creating a performance tradeoff in which the gyroscope can either offer a large bandwidth (mode-split) or a high resolution (mode-matched), but not both without increasing the mass (and consequently, size) of the gyroscope. This bottleneck ultimately precludes current MEMS inertial sensors from being scaled toward navigation-grade operation.

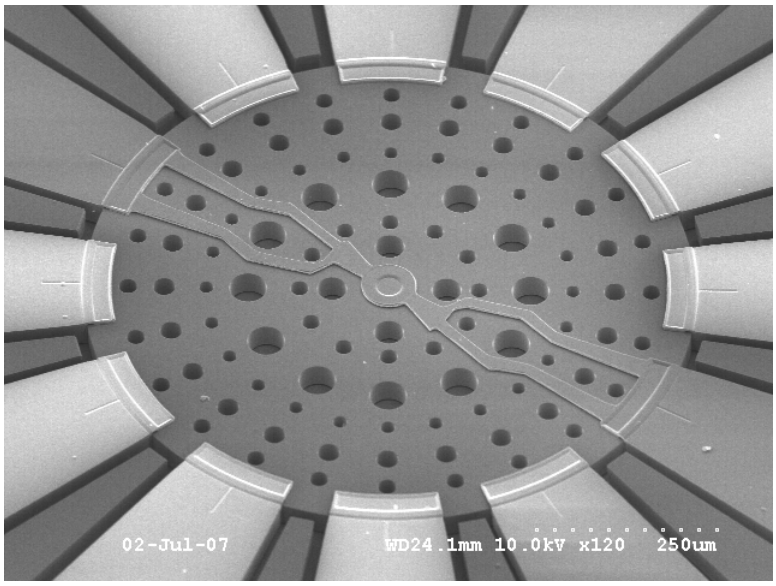

Figure 1-5 – SEM of BAW gyroscope.

It was proposed in [25] that if the drive and sense modes of the gyroscope were shifted several orders of magnitude higher, the mechanical noise in the gyroscope could be minimized while concurrently improving sensor bandwidth and removing the device's sensitivity to environmental and acoustic noise and vibrations [26], making it easier to scale the device to higher levels of performance. This led to development of the bulk acoustic wave (BAW) disk gyroscope (Fig. 1-5), the first high frequency gyroscope reported in literature. In addition to improving sensor resolution and bandwidth, the high frequency of operation of the BAW gyroscope makes it an excellent candidate for use as a timing device. Integrating the clocking and rate sensing onto a single package introduces a smaller, cheaper, and lower power solution to providing the robust functionality needed for commercial electronic platforms compared to what is currently available by incorporating separate timing and rate sensing packaged elements. Furthermore, the timing capabilities provided by the BAW gyroscope can also be used in the development of sensor fusion techniques for improving both noise and power

performance as the gyroscope is integrated into the high-performance, navigation-grade, TIMU platform.

Although the BAW gyroscope provides many benefits to mechanical performance and timing integration, there are certain drawbacks to using such a sensor. For example, the increase in operating frequency results in a larger power demand from the interface electronics. At the same time, the reduction of mechanical noise in HF gyroscopes shifts the burden of noise minimization from the mechanical element to the accompanying circuitry. This dissertation reviews the design, implementation, and optimization of an application specific integrated circuit (ASIC) that will interface with MEMS high-frequency BAW disk gyroscopes. Focus is placed on the noise and power tradeoffs of designing the high frequency ASIC as the system is scaled from rate- and commercial-level performance to high-performance navigation- and inertial-grade systems.

To develop the ASIC, comprehensive mathematical and electrical models of the BAW gyroscope are created and used to develop a low power, low noise CMOS interface architecture to interface with these devices. While designing the ASIC, the challenges associated with optimizing its performance to achieve navigation-level requirements (specifically, by reducing the input referred noise) are discussed. Lastly, an overview of the BAW disk gyroscope's potential as a timing device is investigated and analyzed.

The circuits, systems, and control algorithms developed during the course of this work were designed for and interfaced with a bulk acoustic wave disk gyroscope. With an angle random walk of 0.89 °/√s and a bias drift of 0.1°/s, the BAW sensor is capable of providing rate-grade performance and can thus be implemented in most available commercial and consumer systems today that require rotation sensing. In addition, the

gyroscope can be used as an accurate clock signal, offering a measured TCF of -27 ppm/°C (uncompensated) and phase noise of -104 dBc at 1 kHz from carrier (f_0 = 9.65 MHz), comparable to the state-of-the-art reported in literature.

After demonstrating the rate-grade performance of the BAW disk and identifying techniques to optimize input referred noise and power consumption of the device as it is pushed toward navigation-grade specifications, a 2nd interface scheme is introduced that measures the change in the phase-shift of the gyroscope. Using this technique, it is possible to regularly calibrate the sensor without needing an external rotary stage. As discussed in Section 1.3.1.1 this technique reduces integration time, which consequently reduces angle error and enables more accurate positioning and navigation.

1.5. Thesis Organization

The remainder of this dissertation is organized as follows:

Chapter 2 provides an overview of gyroscope interfacing and discusses how the device is modeled for calculations and simulation. Although most of this discussion is applicable to a wide range of gyroscopes, the work and results reported will focus heavily on high frequency (HF) gyroscope interfacing, specifically the bulk acoustic wave (BAW) disk gyroscope. A brief discussion of the BAW gyroscope design will also be presented in this chapter.

Chapter 3 discusses how discrete and integrated electronics are used to interface with the BAW gyroscope. Details on the design and function of the drive loop and sense channel are outlined, followed by discussion and analysis of the contributions of each block to the ENEΩ of the sensor. This analysis is used to determine how to optimize tradeoff between noise performance and power consumption in sensor design as well as

how to scale the noise down toward navigation-grade specifications while concurrently optimizing power consumption. Following this discussion, strategies to optimize the performance of the test PCB (to reduce noise and improve SNR) are provided in this chapter. The discussion provided in this section can also be used when designing or testing other high- and low-frequency gyroscopes.

In Chapter 4, a hybrid rotation sensor and clock signal is introduced that uses the BAW gyroscope as its sensing/timing element. The noise-optimization techniques discussed in Chapter 3 are implemented, along with architectures for automatic level control of the drive loop and quadrature cancellation architectures of the input sense current. The ASIC discussed in this chapter was fabricated on a TSMC 0.18μm wafer and characterized for performance as both a rotation sensor and a timing device.

Chapter 5 discusses the CMOS implementation of high DC voltage generators (i.e. charge pumps). Challenges to generating high voltages in CMOS processes are presented, followed by techniques that can be used to compensate for any on-chip DC voltage loss. Closed-loop charge pump architectures are also discussed for the purpose of regulating the output DC voltage and minimize its ripple.

Chapter 6 presents an alternate measurement technique for measuring the rotation rate of any 2-degree of freedom vibratory gyroscope. With this scheme, the rotation rate of the gyroscope is measured based on a change in the phase-shift generated by the Coriolis signal rather than an amplitude change. Although it provides similar readout performance when compared to amplitude-readout techniques, the phase-shift readout scheme can also provide a method for calibrating the gyroscope through only minimal modification of the system circuitry. A detailed overview of the phase-shift readout and

calibration schemes is presented, along with a comparison to conventional amplitude readout techniques.

Finally, Chapter 7 provides an overview of the contributions of this work and identifies possible future directions of research in the field of integrated circuits for MEMS gyroscopes.

CHAPTER 2

MODELING OF HIGH FREQUENCY BULK ACOUSTIC WAVE GYROSCOPES

Before a gyroscope interface is designed, models of the device are developed for use in design calculations and simulations. In this chapter, the high-frequency bulk acoustic wave (BAW) gyroscope is introduced, and an outline of device design and operation is given. Additionally, the concepts of mode-matching and quadrature are discussed and used to model the gyroscope mathematically and electrically.

2.1. Bulk Acoustic Wave (BAW) Disk Gyroscopes

CVGs can be classified into one of two groups based on their operating modes [25]: Type-I or Type-II. Type-II gyroscopes use two non-degenerate modes for driving and sensing. These two modes have a large frequency split that requires the application of large DC voltages for matching. On the other hand, Type-I devices utilize two inherently degenerate modes, making their frequency split smaller and easier to tune (i.e. smaller voltages can be applied). Type-II devices include the frame gyroscope and the tuning-fork gyroscope (TFG) while disk-, ring-, shell-, and other uniformly symmetric gyroscopes make up the Type-I architectures (Figure 2-1).

Regardless of its grouping, most reported mode-matched gyroscopes [1, 11, 27] operate at low frequencies (1-100 kHz). At these frequencies, the MNEΩ acts as the principal bottleneck to performance due to contribution from mechanical noise sources such as Brownian motion. In addition, the device's Q is attenuated by factors such as air

damping and thermoelectric damping (TED) [28], indicating the gyroscope must operate at high vacuum (1-10 mTorr) in order to provide high sensitivity.

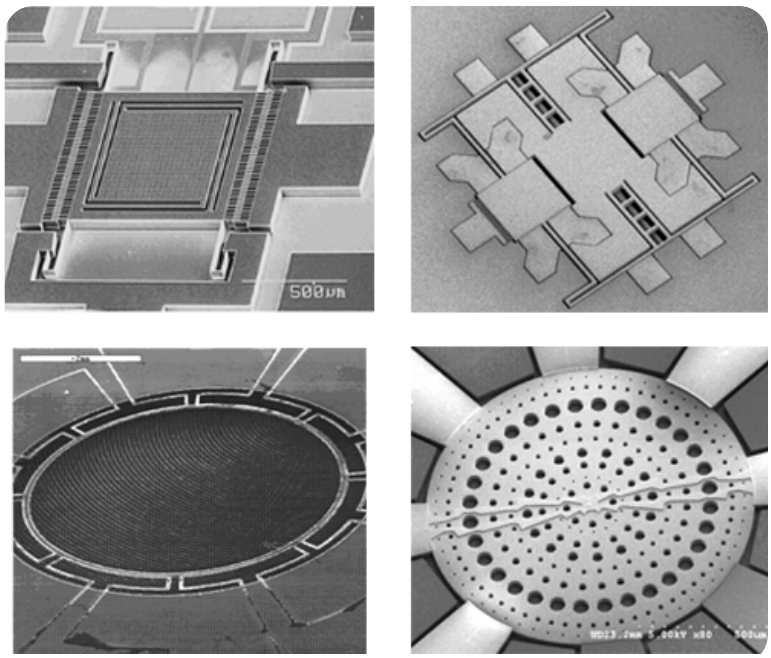

Figure 2-1 – SEM images of Type-I and Type-II gyroscopes. Clockwise from top left: frame gyroscope [29], tuning fork gyroscope (TFG) [30], disk gyroscope [31], ring gyroscope [32].

Based on (1-2)-(1-4), it becomes clear that in order for micro-machined gyroscopes to achieve navigation-grade performance, the TNEΩ must be minimized. This becomes extremely challenging at low frequencies, as the MNEΩ is so large that the sensor resolution is already limited regardless of how well the ASIC is designed. With mass and size limited to exploit the advantages of MEMS fabrication and Q_{eff} limited by the gain-bandwidth tradeoff, the clearest solution to improving performance involves scaling the operating frequency of the gyroscope to a region where MNEΩ = ENEΩ. As shown in Fig. 2-2, as the frequency is scaled from the kHz to the MHz regime, there is a reduction in MNEΩ (along with an increase in ENEΩ). If the frequency is set to where the two components are equal, the TNEΩ will be at relative minimum. Additionally, scaling the

frequency allows the Q_{eff} of the gyroscope to be maintained while simultaneously increasing the operational bandwidth of the sensor.

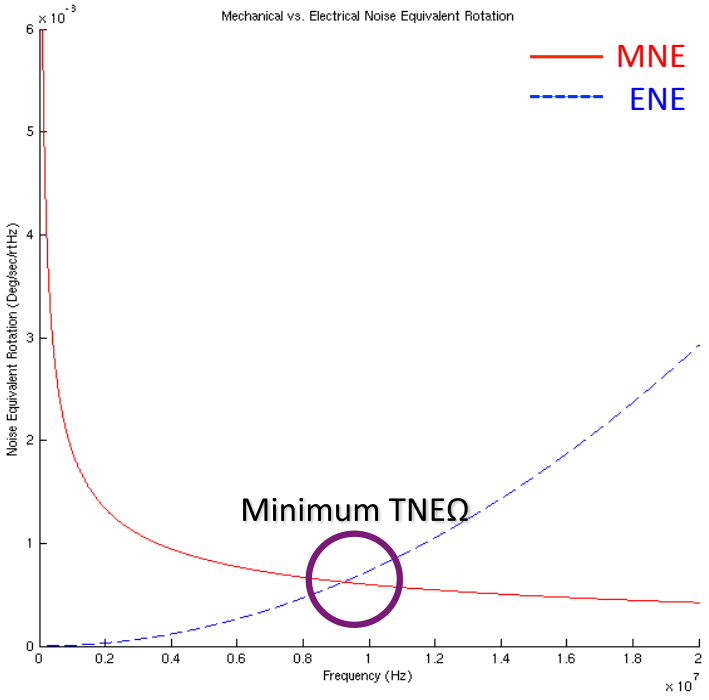

Figure 2-2 – Optimization of TNEΩ by scaling resonance frequency of gyroscope.

The bulk acoustic wave (BAW) disk gyroscope presented in [31, 33-35] is the first reported gyroscope to exploit the advantages of high-frequency operation. The device (Fig. 2-3) is a Type-I degenerate disk structure consisting of a center-supported silicon disk with capacitively-coupled drive, sense, and control (tuning) electrodes. Due to its Type-I degenerate design and bulk-mode operation, the resonance frequency of the BAW gyroscope operates several orders of magnitude higher than other vibratory gyroscopes, reducing sensor MNEΩ along with the sensitivity of the gyroscope to low frequency vibrations and acceleration. At the same time, the small gap sizes between 180-250 nm between the disk and its electrodes reduce the motional impedance of the device, while

the bulk acoustic actuation of the gyroscope results in a high device stiffness and superior shock tolerance for the BAW disk gyroscope when compared to similar sensors.

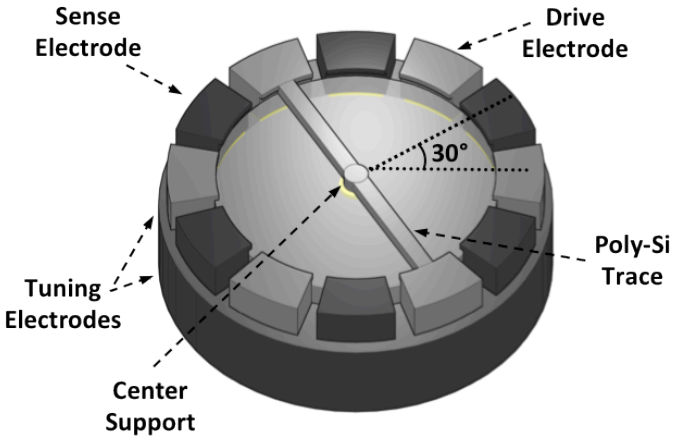

Figure 2-3 – Schematic view of [100] BAW disk gyroscope.

To operate the BAW disk gyroscope, the drive and sense modes are excited into either their primary or secondary degenerative bulk acoustic modes, which both present at frequencies several orders of magnitude higher than other vibratory gyroscopes (1-10 MHz). Electrodes are arranged at the anti-nodes of the resonant drive and sense modes to facilitate mode-matched operation and maximize transduction [31, 33]. Poly-silicon traces (Fig. 2-3) are attached between the center of the disk and one or more control electrodes to provide the disk with a DC polarization (bias) voltage.

To release the disk gyroscope from the underlying substrate, several release holes are patterned and etched throughout the disk. These release holes are placed at the nodes of the drive and sense modes in order to minimize any frequency shift between the two modes (placed spatially every 30° for [100] silicon), but still create a small frequency split between the drive and sense modes. Additionally, imperfections in the release along with other fabrication steps can create a misalignment between the drive and sense modes

and their respective electrodes, introducing further quadrature error. DC tuning voltages must be applied at the proper control electrodes to match the modes of the gyroscope and reduce quadrature in the sensor. Finally, the presence of release holes reduces the stiffness of the device and increases thermo-elastic damping effects, limiting the maximum attainable Q [36].

2.2. The Drive and Sense Modes

Figure 2-4 shows an ANSYS simulation of the degenerate drive and sense modes of a [100] BAW disk gyroscope, the device used throughout this thesis. For the [100] disk, electrodes are placed spatially 30° apart to align with the nodes and antinodes of the two modes. Due to the orthogonality between the direction of vibration (drive) and the direction required to measure Coriolis acceleration (sense), the nodes of the drive mode are aligned with the positive and negative antinodes of the sense mode. Similarly, the antinodes of the drive mode align with the nodes of the sense mode. This orthogonality is mathematically represented by a 90° phase shift between the drive and sense modes.

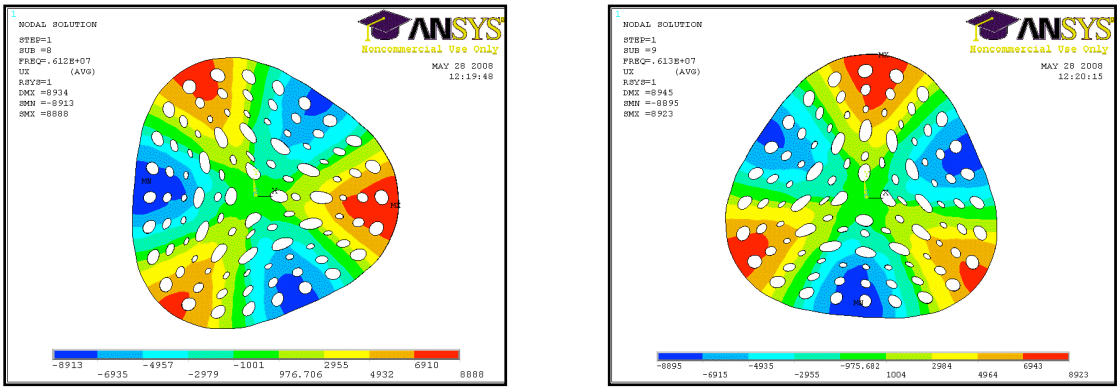

Figure 2-4 – ANSYS simulations of [100] BAW disk gyroscope (left) drive and (right) sense modes. The nodes of each mode are shown in green, while the antinodes are highlighted in red and blue.

Because of the inherent symmetry of the bulk acoustic mode shapes, the gyroscope can be driven and sensed differentially by simultaneously actuating/sensing from the

positive and negative drive/sense electrodes. Differential operation offers several benefits for gyroscopes – at the drive mode, fully-differential amplification of the positive and negative drive signal inputs can double the total ASIC output voltage ($V_{D(+)} - V_{D(-)} = 2V_D$). At the sense output, the common-mode rejection offered through differential operation increases dynamic range and suppresses common-mode (environmental/supply) noise and second-order non-linearity. However, the use of a differential architecture also increases the ASIC power consumption, as parallel signal paths are needed to accommodate both positive and negative signals.

2.2.1. Mode-Matching

As mentioned in Chapter 2.1, the two degenerate modes are not perfectly matched due to fabrication imperfections, such as the addition of release holes throughout the BAW disk structure. Because the modes are split, only a partial transfer of energy can occur when Coriolis acceleration is applied and the sensor cannot fully exploit the noise and sensitivity benefits offered with mode-matched operation. To mode-match this device, tuning voltages are applied to control electrodes (i.e. electrodes not connected to drive, sense, or V_P), which change the stiffness of the disk and move the drive mode and the sense mode towards one another [31].

Figure 2-5 shows the frequency response of the drive mode of the gyroscope before and after the device is mode-matched (measured using an Agilent 4395A Network/Spectrum/Impedance analyzer). Before matching the modes, two high-Q peaks are visible from the network analyzer - one generated at the resonance frequency of the drive mode (ω_d) with a quality factor Q_d, while the other is generated at the sense resonance frequency (ω_s) with a quality factor Q_s. The sense mode is present on the

network analyzer as a consequence of quadrature (Chapter 2.2.2). It is not possible to determine which peak corresponds to what mode from the images above, although the peaks can be identified based on what electrodes are needed to tune each unique mode. After tuning is applied, the resonance frequencies of the two modes are matched to form a single, high-Q peak (Q_{eff}). Because both the drive and sense modes are now operating at precisely the same frequency, the two peaks are no longer distinguishable from one another ($\omega_d = \omega_s = \omega_0$, $Q_d = Q_s = Q_{eff}$).

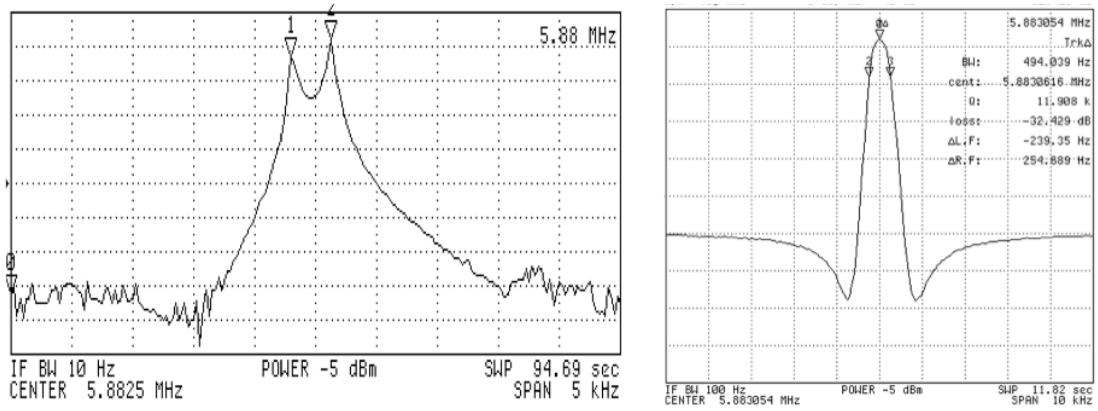

Figure 2-5 – Drive and sense modes of [100] BAW disk (left) before and (right) after mode-matching.

If a process flow can be established that successfully matches the drive and sense modes of the gyroscope, an IC can be designed that implements this algorithm automatically. In [37, 38], automatic mode-matching is accomplished by automated electrostatic tuning of the sense mode. As the two modes get closer, the zero rate output measured at the sense electrode increases until it reaches a maximum when the two modes are matched. In [39], two identical signals are applied at identical positive and negative frequency offsets from the resonance peak. The device is then electrostatically tuned based on the amplitude difference between these two signals after they are passed

through the gyroscope. When the modes are matched, the two signals will be equal to one another.

2.2.2. Quadrature Signal

2.2.2.1. Quadrature and Zero Rate Output (ZRO) in MEMS Gyroscopes

The frequency response of the unmatched gyroscope shown in Fig. 2-5 presents two distinct resonance peaks from the drive and sense modes. However, if the drive and sense modes are truly orthogonal, only one peak should be visible on the network analyzer. This aberration is an effect of quadrature, which can be described for gyroscopes as the undesired coupling between the drive and sense modes due to imperfections introduced in the design, fabrication, and/or packaging of the sensor. As a consequence of these imperfections, drive mode vibrations are no longer completely suppressed at the sense electrode, and a component of this signal is detected even when no rate is applied to the sensor (Fig. 2-6). For this zero-rate case, the signal measured at the sense output is referred to as the zero-rate output (ZRO) of the gyroscope.

Fig. 2-6 shows diagrams of two [100] disk gyroscopes, each with 12 electrodes that are used to drive (red), sense (blue), or tune (gray) the gyroscope. The first (left) gyroscope has been perfectly fabricated while the second (right) has fabrication misalignments and non-idealities. It should be noted that based on the coordinate axes defined in Fig. 2-6, the drive electrode is considered aligned with the x-axis, while the sense electrode is considered aligned with the y-axis. This convention will be used throughout this thesis.

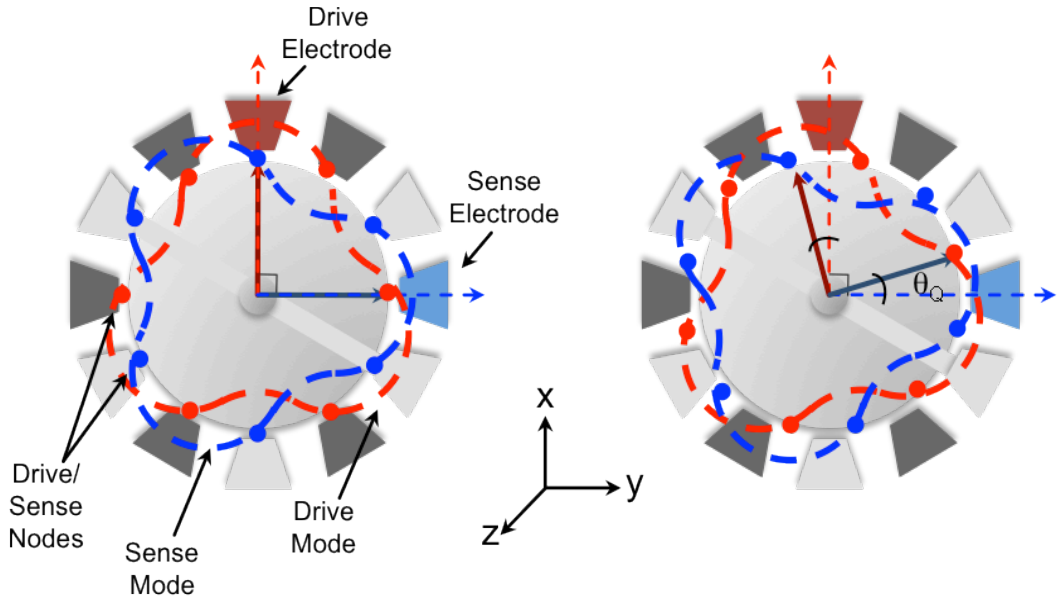

Figure 2-6 – Modes of disk gyroscope (left) without and (right) with quadrature. The drive mode and drive electrode are both shown in red, while the sense mode and electrode are highlighted in blue. In addition, arrows are used to point to the location of the drive (red) and sense (blue) modes (solid) and electrodes (dashed) for both gyroscopes.

In the first (ideal) device, the nodes of each mode are aligned with either the positive or negative anti-nodes of its complementary mode, as described earlier. The lack of imperfections leaves both the drive (red) and sense (blue) modes perfectly aligned with their respective electrodes at the x- and y-axes, as indicated by the solid and dashed arrows. As a result, the vibrations of the drive mode are not observed at the sense electrode (i.e. no quadrature is present), and unless a Coriolis signal is applied to the gyroscope, no signal will be observed at the output.

In the second (non-ideal) gyroscope, imperfections and misalignments introduced during device fabrication or packaging have resulted in mode tilting, a phenomenon in which the drive and sense modes of the gyroscope are no longer aligned with their respective electrodes. The modes deviate from their electrodes (and thus, the x- and y-axes) by angle θ_Q (Fig. 2-7). Because the sense mode is no longer perfectly aligned to

the sense electrode, only a component of the maximum Coriolis signal seen at the anti-node will be fed to the sense electrode. Additionally, the sense electrode is no longer completely orthogonal with the drive mode, so a component of the drive mode is now present at the sense electrode. The sense thus becomes the sum of two signals, given by

$$y(t) = y_{Coriolis}(t) + y_{quadrature}(t) \qquad (2\text{-}1)$$

where $y_{Coriolis}$ and $y_{quadrature}$ represent the Coriolis (sense) and quadrature (drive) components of the sense output, respectively.

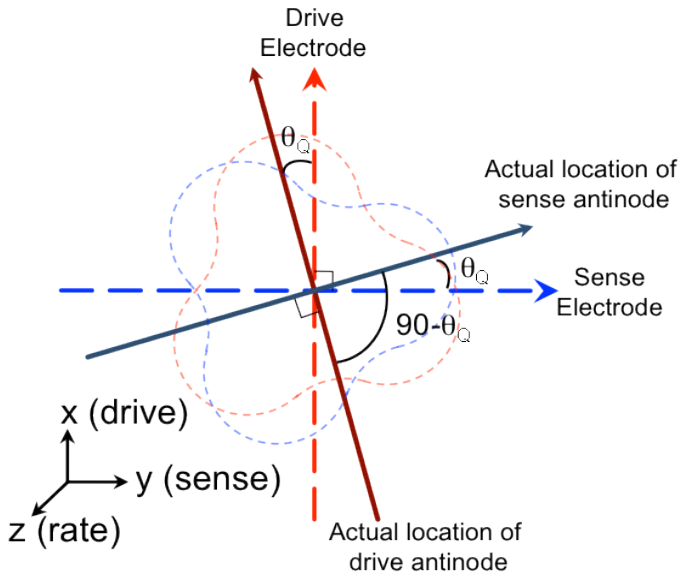

Figure 2-7 – Impact of mode tilting at the drive and sense electrodes.

It should be noted that although the drive (sense) mode is no longer aligned with the drive (sense) electrode, the two modes (along with the drive electrode and sense electrode) are still orthogonal with respect to one another. Quadrature does not occur because the orthogonality between the drive and sense modes has changed. Rather, it occurs because the point on the disk where the Coriolis signal is completely isolated from the drive signal is no longer aligned with the electrode measuring that signal.

Consider a BAW disk gyroscope oscillating sinusoidally along the x-axis with maximum drive amplitude of q_{drive}. From (A-10), the amplitude of vibration can be characterized as

$$x(t) = q_{drive}\sin(\omega_{n_d} t) \tag{2-2}$$

Because the drive mode is tilted, a component of the drive amplitude (referred to as the quadrature component) is aligned with the y-axis and thus measurable at the sense output electrode. The quadrature component ($y_{quadrature}$) can be defined as

$$y_{quadrature}(t) = x(t)\cos(90 - \theta_Q) \tag{2-3}$$

Simplifying (2-3) and substituting this equation into (2-2) gives

$$y_{quadrature}(t) = q_{drive}\sin(\omega_{n_d} t)\cdot\sin(\theta_Q) \tag{2-4}$$

which reduces to

$$y_{quadrature}(t) = \theta_Q \cdot q_{drive}\sin(\omega_{n_d} t) \tag{2-5}$$

for small values of θ_Q.

In addition to quadrature, the sense electrode detects a component of the signal generated by the applied rotation rate, which can be calculated by substituting (2-2) into (1-1), giving

$$y_{Coriolis}(t) = \int\int 2\frac{\partial x(t)}{\partial t} \times \Omega\cdot\cos(\theta_Q)\partial t \tag{2-6}$$

This can be simplified to

$$y_{Coriolis}(t) = \frac{2q_{drive}}{\omega_{n_d}}\Omega\cos(\omega_{n_d} t)\cdot\sin\theta\cdot\cos(\theta_Q) \tag{2-7}$$

where θ represents the angle between the input velocity (x-axis) and applied rate (z-axis) vectors. Because the two signals are orthogonal (θ=90°), the Coriolis term simplifies to

$$y_{Coriolis}(t) = \frac{2q_{drive}}{\omega_{n_d}}\Omega\cos(\omega_{n_d}t)\cdot\cos(\theta_Q) \tag{2-8}$$

Substituting (2-5) and (2-8) into (2-1) gives

$$y(t) = \frac{2q_{drive}}{\omega_{n_d}}\Omega\cos(\omega_{n_d}t)\cdot\cos(\theta_Q) + \theta_Q\cdot q_{drive}\sin(\omega_{n_d}t) \tag{2-9}$$

It can be seen from (2-9) that the quadrature and Coriolis components of the sense output are both centered around the drive resonant frequency with a phase variation of 90° relative to one another as indicated by the $\sin(\omega_d)$ and $\cos(\omega_d)$ terms. The phase difference originates from the fact that the Coriolis acceleration is sensitive to proof-mass velocity along the drive axis (2-8), while the quadrature error is proportional to the proof-mass position along this axis (2-5) [40]. Because the drive signal must also be orthogonal to the sense output, it can be further assumed that the drive signal is either perfectly in-phase (0°) or out-of-phase (180°) with the quadrature signal. When no rate is applied, the $y_{Coriolis}$ term becomes zero and only $y_{quadrature}$ remains, giving the ZRO of the sensor.

If no compensation techniques are applied, quadrature can create several problems for the sensor. First, the maximum sense current generated at the sense antinode is no longer aligned to the sense electrode. Consequently, only a fraction of the maximum Coriolis amplitude will be passed to the sense electrode [41], represented by the $cos(\theta_Q)$ term given in (2-8). Additionally, the input amplifiers along the sense channel interface circuitry will detect signals from both the $y_{Coriolis}$ and $y_{quadrature}$ terms now present at the sense electrode. Because ZRO is several times larger than $y_{Coriolis}$ [42], it pushes the input sense channel electronics out of small-signal (linear) operation, whereby the gain of the channel is reduced and its input-referred noise deteriorated. This is further degraded by mixing within the MOS transistors in the sense channel amplifiers due to the presence

of two sinusoidal inputs. Lastly, the ZRO produces a nonzero output from the sense amplifying chain, even when no rate is applied. Due to the finite output voltage range of the interface electronics, ZRO thus creates a tradeoff between system sensitivity and dynamic range of the gyroscope, in which the gain (sensitivity) of the ASIC must be reduced in order to reach the desired sensor dynamic range. Chapter 4 discusses how this tradeoff affects a vibratory gyroscope's ability to provide navigation-grade measurement.

Quadrature and ZRO are generated from the combined effects of several sources of error created by the device, interface electronics, and the sensor packaging [42]. Fabrication imperfections and misalignments are a major source of quadrature that can lead to mode tilting as described earlier. In addition, the sense signal may also be directly actuated by the drive mode through non-idealities in the gyroscope due to a process called direct-motion coupling [42] or through feedthrough from stray capacitances connected to the silicon substrate (Chapter 2.3.3.2). Lastly, poor packaging or fabrication can create a non-uniform stress across the sensing element that can change how the drive and sense modes are coupled.

2.2.2.2. Quadrature Compensation Techniques

Practically speaking, it is impossible to completely remove quadrature/ZRO. The effects of each source of quadrature vary even across two devices fabricated on the same wafer, making simple DC offset cancellation techniques inadequate to solve the problem. However, quadrature compensation is a necessary tool that significantly improves both the dynamic range and resolution of the sensor [41]. Therefore identifying techniques to cancel the quadrature at the sense electrode are of critical importance for high-performance gyroscope design.

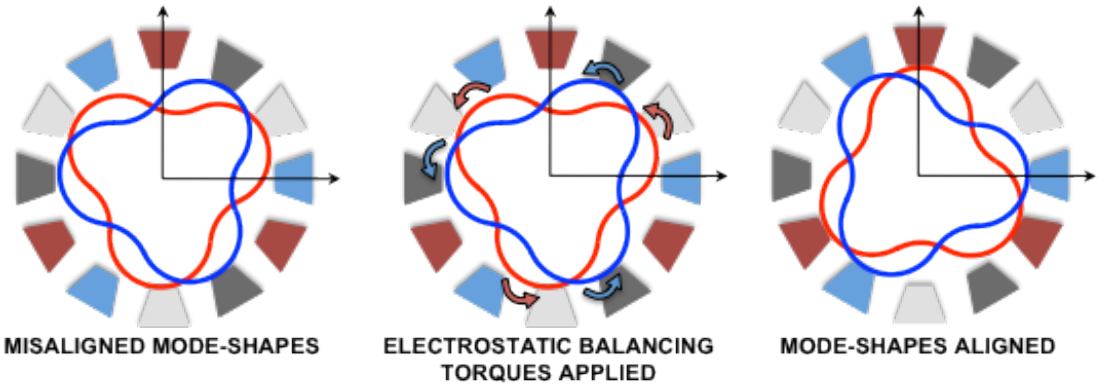

Figure 2-8 – Illustration of quadrature cancellation through electrostatic compensation.

With rate vibratory gyroscopes, many available methods of quadrature cancellation involve manipulation of the mechanical element through the application of an electrostatic force [27, 41], laser trimming [43, 44], or material deposition [45]. Techniques have also been introduced for compensation of the ZRO signal through pseudo-continuous sampling of the quadrature signal [46] or by adding a compensation signal to the sense input [47, 48]. In the case of the BAW gyroscope, the control electrodes needed for quadrature cancellation are independent of those needed to match the drive and sense modes, ensuring that an electrostatic force can be applied without creating any crossover effects on the disk. The control voltages apply a rotational torque to the proof mass (Fig. 2-8) [40], causing the proof mass and the modes of the gyroscope to rotate clockwise or counter-clockwise depending on the voltages applied. If the correct voltages are applied, the proof mass will align the drive and sense modes to their respective electrodes, attenuating (or ideally, removing) the quadrature component of the sense output.

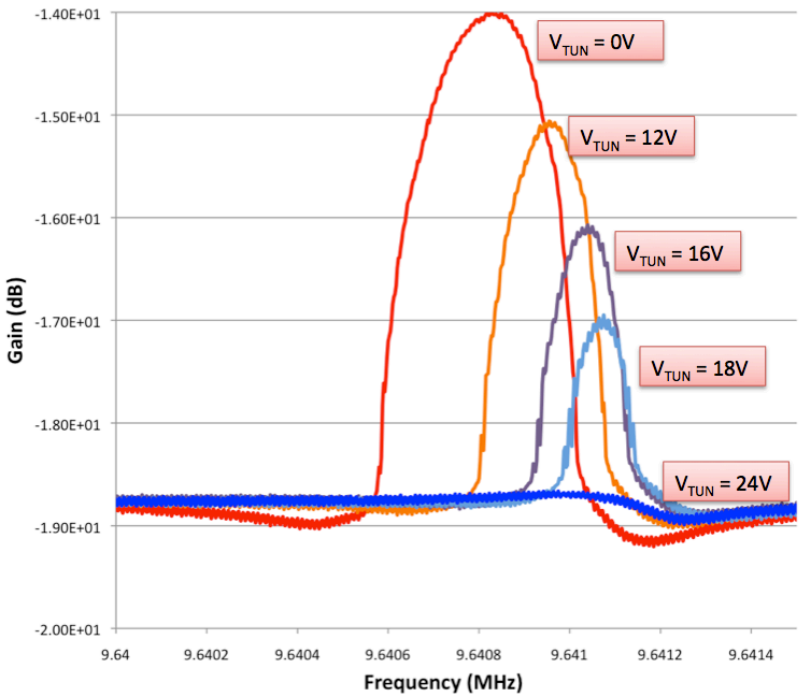

Figure 2-9 – Reduction of quadrature signal through electrostatic tuning of BAW gyroscope.

One example of electrostatic tuning applied to the BAW gyroscope is shown in Fig. 2-9. As mentioned in Section 1.2.2.1, if the drive and sense modes are not orthogonal, both output signals will be visible on a network analyzer. In Fig. 2-9, the RF signal of the network analyzer is applied to the drive input of the gyroscope while the output is taken from the sense electrode. Although the drive and sense modes of the BAW disk have already been matched, a signal is visible at the sense electrode because of quadrature. Applying an electrostatic tuning voltage (V_{TUN}) induces a rotational torque on the disk that causes the proof mass to rotate, reducing the quadrature angle θ_Q between the sense mode and the sense electrode. From (2-5) it can be concluded that this reduction in θ_Q will create a proportional attenuation of $y_{quadrature}$ at the sense electrode, shown in Fig. 2-9 as V_{TUN} increases from $0V$ to $24V$. Along with a reduction in the quadrature signal, there is a slight increase in the resonance frequency of the gyroscope

because of the reduction in stiffness imposed by the application of V_{TUN}. After the correct cancellation voltage ($V_{TUN} \sim 24V$) is applied, virtually no signal is visible at the sense electrode ($\theta_Q \sim 0$).

In addition to electrostatic tuning, quadrature cancellation can also be performed via electronic compensation on the IC (circuit) level. Because the drive mode of the gyroscope is either in-phase (0°) or out-of-phase (180°) with the quadrature signal, it can be added to or subtracted from the sense signal to cancel the quadrature component. One example of this technique is discussed in [46], in which alternate clocking stages are used to first sample the drive mode and then add it to the sense signal to cancel out its quadrature component. Although this topology works effectively for low-frequency sensors, the high-clock speeds needed to run such architectures can be problematic for use with high-frequency devices (such as the BAW), as the switches come with a considerable power cost. Therefore, different compensation strategies must be considered for BAW devices.

2.3. Equivalent Circuit Model of a Gyroscope

In this section, the mathematical and electrical models used to design the BAW gyroscope interface ASIC are presented based on the properties of the disk outlined in the previous subsections. It should be noted that the models discussed here could also be applied to other MEMS vibratory gyroscopes based upon a 2 degree of freedom (DOF) mass-spring system.

2.3.1. Drive Amplitude

From an electrical standpoint, the gyroscope can be considered a coupled resonator system in which the sense mode is linked to the drive mode through rotation-induced

Coriolis acceleration [40]. The complete derivation of the drive and Coriolis (sense) amplitudes is given in Appendix A, from which the drive amplitude is calculated to be

$$x(t) \approx -\frac{Q_d C_0}{M\omega_{n_d}^2 g_0} v_{ac} V_P \sin(\omega_{n_d} t) \tag{2-10}$$

where Q_d, C_0, M, ω_d, g_0, V_P, and v_{ac} represent the drive mode quality factor, rest capacitance of the gyroscope, mass of the gyroscope, drive mode resonance frequency, rest gap distance between the parallel plates, DC polarization voltage, and AC drive voltage, respectively. Of these variables, Q_d, C_0, M, ω_d, and g_0 are determined during the design and fabrication of the device; only V_P and v_{ac} can be used by the ASIC to control the amplitude of the drive mode. To generate the largest Coriolis current, v_{ac} must have a large enough amplitude to create a bulk acoustic displacement one-tenth the size of g_0, the maximum amplitude of $x(t)$ for which the gyroscope is still considered to be driven linearly, while V_P must be as large as possible.

2.3.2. Coriolis-Induced Sense Amplitude

As described earlier, the sense mode displacement is coupled to the drive mode through Coriolis acceleration. From Appendix A, this displacement is calculated to be:

$$y(t) = \frac{Q_s}{M\omega_{n_s}^2}\left(2M\vec{\Omega}_z\right)\frac{v_{ac}V_P Q_d C_0}{M\omega_{n_d}^2 g_0}\left(\omega_{n_d}\cos(\omega_{n_d} t)\right) \tag{2-11}$$

It can be seen that the orthogonality of the drive and sense modes is preserved through the presence of a 90º phase shift indicated by the sine and cosine terms in (2-10) and (2-11), respectively. This phase variation is important in distinguishing the Coriolis signal from the quadrature signal (as discussed in Chapter 2.2.2).

If the gyroscope operates under mode-matched conditions ($\omega_d=\omega_s=\omega_0$, $Q_d=Q_s=Q_{eff}$), (2-11) reduces to:

$$y(t) = \frac{2v_{ac}V_P Q_{eff}^2 C_0 \vec{\Omega}_z}{M\omega_0^3 g_0}\cos(\omega_0 t) \qquad (2\text{-}12)$$

where Q_{eff} and ω_0 are the mode-matched quality factor and resonance frequency, respectively, and Ω_z denotes the Coriolis (rate) signal applied to the gyroscope. At the sense electrode, Ω_z is modulated on top of a carrier signal ($\cos(\omega_0 t)$) generated by the drive vibrations of the gyroscope at the device's resonance frequency. AM demodulation is required to extract the rate signal from *y(t)*.

In addition to Ω_z, the sense output can also be modulated by v_{ac}, which may vary over time due to environmental changes, noise, device aging, or shock. To optimize gyroscope performance, it is critical to prevent changes in v_{ac} from affecting *y(t)*. This requires the implementation of automatic level control to actively hold the drive signal at constant amplitude during sensor operation, which will be discussed in further detail in Chapter 4.

When a rotation rate is applied, the resulting deflection of the gyroscope creates a current, which is calculated (Appendix A) to be

$$I_S(t) = \frac{-2v_{ac}V_P^2 C_0^2 Q_{eff}^2}{M\omega_0^2 g_0^2}\vec{\Omega}_z \sin(\omega_0 t) \qquad (2\text{-}13)$$

Equation (2-13) shows that in addition to increased bandwidth, reduced Brownian noise and small form factor, the sensitivity of BAW gyros is inversely proportional to ω_0^2. this dependence can be counteracted either by increasing the drive voltage v_{ac} or decreasing the gap size g_o [12].

2.3.3. Drive Loop Equivalent Circuit Model

2.3.3.1. Lumped Element Model

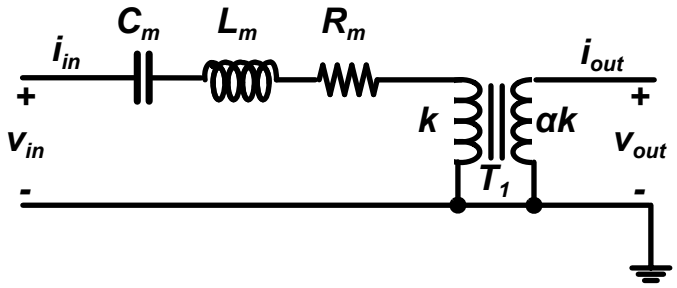

Figure 2-10 – Lumped element electrical model for resonator.

Each mode of an ideal BAW disk gyroscope is analogous to a capacitive resonator that can be represented by a series RLC tank (Fig. 2-10) with a frequency response analogous to that of a band pass filter. The quality factor of the gyroscope and its resonance frequency are determined by:

$$Q = \frac{\omega_0 L_m}{R_m} \tag{2-14}$$

and

$$\omega_0 = \sqrt{\frac{1}{L_m C_m}} \tag{2-15}$$

Here, L_m, C_m, and R_m represent the motional inductance, capacitance, and resistance, respectively. The motional resistance (R_m) of the gyroscope can be defined as [49]

$$R_m = \frac{\sqrt{KM}\, g_0^4}{Q_d \varepsilon_0^2 L_{eff}^2 h^2 V_P^2} \tag{2-16}$$

where K, ε_0, L_{eff}, and h represent the stiffness of the gyroscope, electric constant (8.854×10^{-12} F m^{-1}), effective length of the drive and sense electrodes, and thickness of the disk, respectively. The phase relationship between the input and output electrodes of the resonator is depicted by transformer T_1, which can be either 0° (α=1) or 180° (α=-1) depending on which electrodes are used. For the designs mentioned in this thesis, the

interfaced gyroscopes had a resonance frequency between ω_0 = 6-10 MHz, α = 1, and a motional impedance from R_m = 30-200 kΩ.

2.3.3.2. Parasitic Capacitances From Gyroscope Fabrication

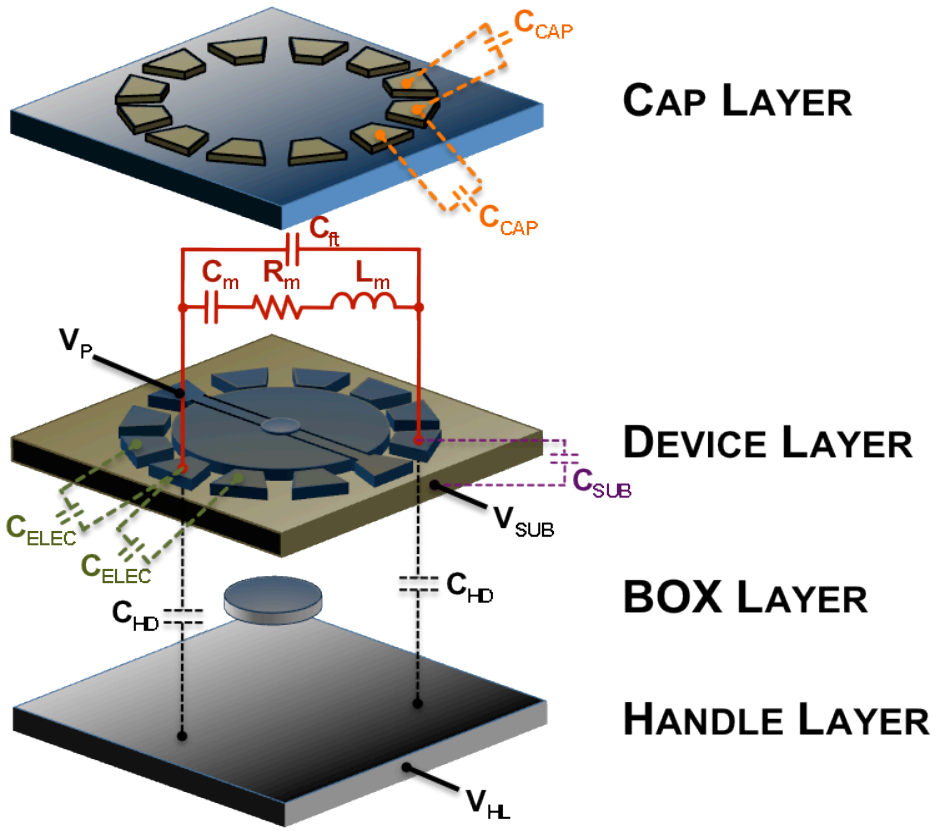

Figure 2-11 – Comprehensive electrical model of packaged BAW gyroscope.

Figure 2-11 shows a comprehensive breakdown of the gyroscope electrical model for the drive mode. A packaged gyroscope consists of 4 distinct layers that each provide specific functions to ensure the device operates correctly. At the bottom of the stack lies the handle layer, a single-crystal silicon (SCS) layer that acts as the base upon which the gyroscope is fabricated. Next is the BOX layer, a thin layer of silicon dioxide (SOI) that separates the device layer from the handle layer and allows the gyroscope to vibrate freely. Atop the BOX layer sits the device layer. All the active components of the

gyroscope (i.e. the disk and the electrodes) are processed on this layer. These 3 layers make up a BAW disk gyroscope composite that can be integrated with an ASIC to form a rotation sensor. However, if the device layer is left exposed it is possible for particles of dust or slurry from the environment to come into contact with the gyroscope and damage the device. In addition, exposing the gyroscope to air will reduce its quality factor. Although the high stiffness of the BAW gyroscope does give it better immunity to air damping than low frequency architectures, low vacuum is nonetheless important to obtain the best performance out of the sensor. For these reasons, a cap layer is placed above the device layer as the final stage of fabrication.

Although the resonator model in Chapter 2.3.3.1 provides electrical equivalents for the mechanical elements of the gyroscope, it does not include several parasitic capacitances present in the gyroscope that must be considered for ASIC design (Fig. 2-11). The parasitic capacitance C_{HD} is created when the BOX layer is etched to release the device layer from the handle layer, consequently creating a capacitance across the two layers. Capacitances C_{ELEC} and C_{CAP} are created from the narrow gaps between each electrode of the gyroscope on the device and cap layers, respectively. C_{SUB} is formed on the device layer between each electrode and the silicon substrate. Finally, parasitic capacitance C_{ft} is created between the input and output electrodes due to the feedthrough that exists between the two terminals from the substrate (device layer).

The feedthrough capacitance ($C_{ft\text{-}Gyro}$) between the drive input and output is analogous to the feedthrough component of quadrature (Chapter 2.2.2.1), in which the two electrodes are also coupled together through the presence of parasitic/stray capacitances present in both the silicon substrate and the interface ASIC. These capacitances create a

second signal path, one that passes the input signal to the output electrode without going through the device. In the case of quadrature, the input signal passes to the sense electrode and is added to the quadrature component ($y_{quadrature}$) of the sense output. With drive feedthrough, the drive input and output are directly coupled through C_{ft}. However, even a small feedthrough capacitance can cause many changes to the frequency response of the gyroscope, which include:

1. *Higher noise floor* – the presence of parallel signal paths reduces the impedance between the input and output electrodes, allowing noise (i.e. any signal where $f_{noise} \neq f_0$) to pass more freely across the terminals. Because the feedthrough path is purely capacitive, the impedance of the parallel path will become smaller as f_{noise} increases. This can become a significant issue in BAW gyroscopes due to their high operating frequency, and if the device is not carefully designed to minimize feedthrough, it is possible for an ASIC with a high gain drive-loop to lock into oscillations at spurious frequencies instead of the resonance mode of the gyroscope.
2. *Smaller resonance peak* – in high frequency resonant BAW gyroscopes, the impedance of the capacitive feedthrough path is small and non-negligible when compared to the motional impedance of the device. As a result, a portion of the motional current generated by the disk will flow through the parallel path created by the feedthrough capacitor, reducing the magnitude of the resonance peak generated from the gyroscope. If the feedthrough is large enough, no current will flow through the resonator, and the drive loop will not be able to lock into oscillations with the drive mode. Even if the feedthrough remains small, the reduction in peak size

combined with the increase in the noise floor will reduce the phase noise of the drive loop and consequently lower the resolution of the sensor.

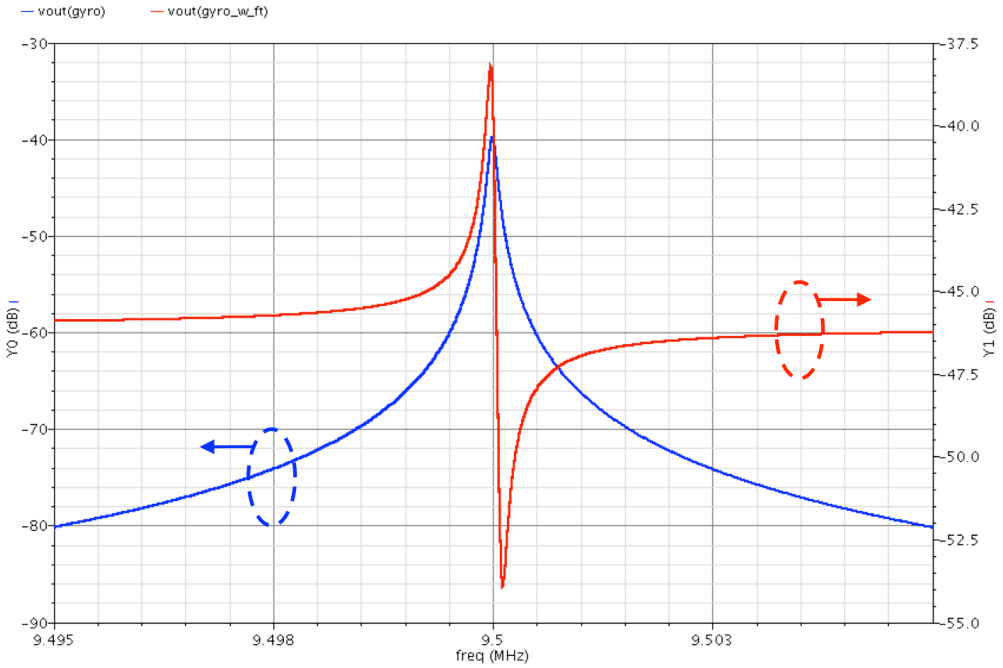

Figure 2-12 – Gyroscope frequency response with (blue) no feedthrough capacitance. (red) With a feedthrough capacitance of 5 fF.

3. *Creation of anti-resonance peak* – shown in Fig. 2-12, the feedthrough capacitance forms an anti-resonance peak near the resonance frequency of the gyroscope. Although there is no performance reduction associated with the anti-resonance peak, the proximity of the anti-resonance peak to the resonance peak is directly related to the magnitude of the feedthrough capacitance.

With careful design and fabrication, the feedthrough capacitance will not be large enough to cause significant issues for the interface ASIC. However, it is important to include this capacitance in gyroscope simulations to be aware of any conditions in which the gyroscope may lock into a spurious mode, or not lock into oscillations at all.

2.3.3.3. Parasitic Capacitances From External Connections

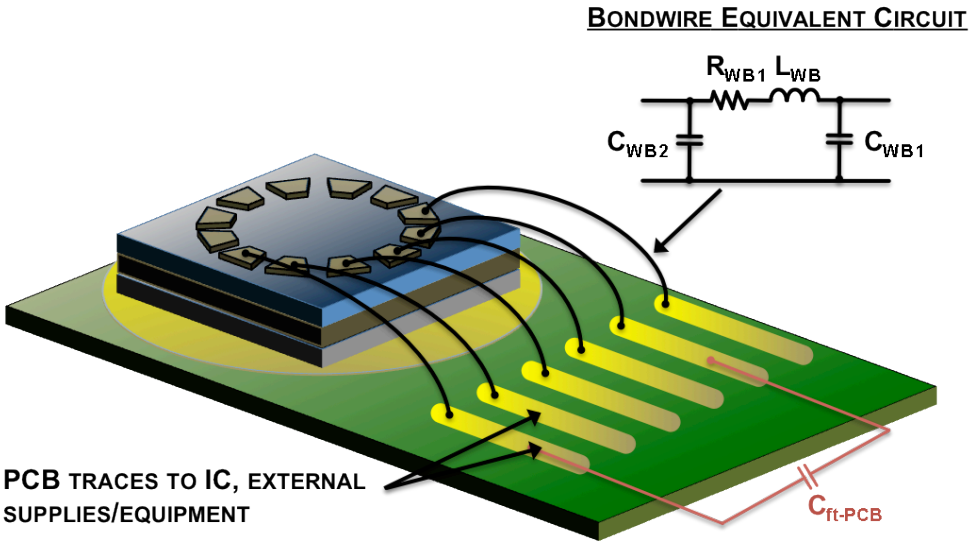

Figure 2-13 – Parasitics added to gyroscope model due to PCB interfacing and testing.

In addition to the parasitics present through device fabrication and packaging, more shunt/feedthrough capacitance is added when the gyroscope is interfaced with the ASIC and placed in a package or on a printed circuit board (PCB) for system testing and characterization (Figure 2-13). The shunt component of the parasitic capacitance comes from bondwire interconnects between the PCB/package/ASIC and the gyroscope. Depending on the length of these wirebonds, this capacitance can range from 10-100fF (including the shunt parasitics of the external connection) [50]. The feedthrough capacitance is created between the input and output pads placed on the PCB or package that are wirebonded to the input and output of the gyroscope. Although these parasitics are unavoidable, they can be attenuated if the size of the PCB/package is reduced or all supply pins from the ASIC are directly connected the gyroscope.

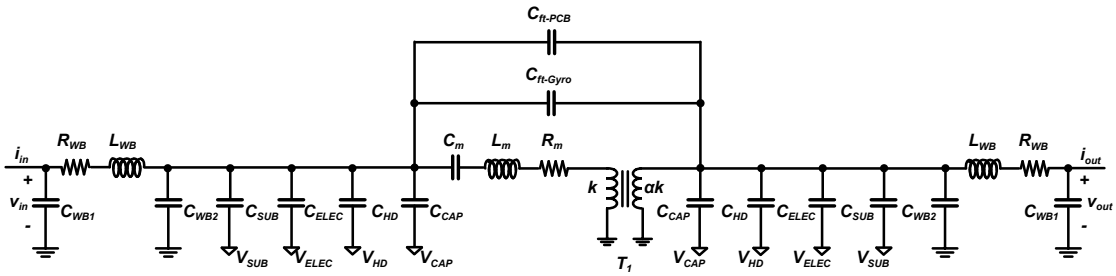

Figure 2-14 – Equivalent circuit model of the BAW gyroscope accounting for all parasitics.

Figure 2-14 presents the equivalent circuit model of the gyroscope used if all parasitic capacitances of the gyroscope are considered. This model can be heavily simplified if a few simple assumptions are made. First, R_{WB} and L_{WB} can be neglected because the impedance of the bondwire is negligible at the gyroscope resonance frequency. Next, V_{CAP}, V_{HD}, V_{ELEC}, and V_{SUB} are all connected to the fixed DC voltages (either V_P, V_{TUN}, or GND) that are AC grounded at steady state. Since these shunt capacitances are connected in parallel, they can be added together. Lastly, feedthrough capacitors $C_{ft\text{-}PCB}$ and $C_{ft\text{-}Gyro}$ are in parallel and can be combined as well. If these changes are made, the equivalent circuit of the gyroscope can be simplified to the diagram shown in Fig. 2-15. Here, the parasitic capacitance C_P is defined as:

$$C_P = C_{WB1} + C_{WB2} + C_{SUB} + C_{ELEC} + C_{HD} + C_{CAP} \tag{2-17}$$

And the feedthrough capacitance C_{ft} is defined to be

$$C_{ft} = C_{ft\text{-}GYRO} + C_{ft\text{-}PCB} \tag{2-18}$$

Typically, the parasitic capacitances for the BAW gyroscope range between 3-6 pF, depending on the size of the electrodes and whether or not the device is packaged. Additionally, the feedthrough capacitance is estimated to be between 10-20fF.

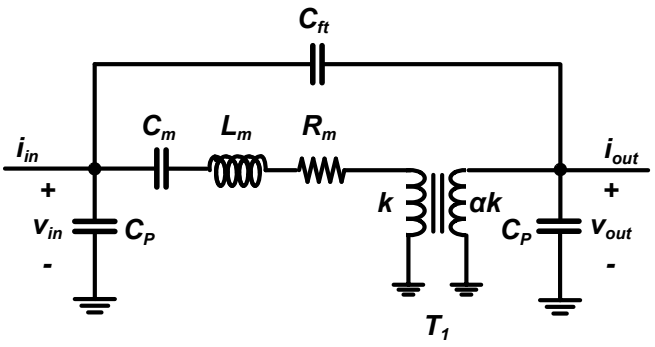

Figure 2-15 – Simplified equivalent circuit model of BAW gyroscope drive mode.

Figures 2-14 and 2-15 present electrical models of the drive mode that assume a clean (low resistance) AC ground connection where the polarization/tuning voltage is connected to the shunt parasitic. However, if these voltages are generated using on-chip DC voltage generators (charge pumps, voltage regulators), there is instead a large impedance R_{VP} associated with the DC voltage generator (Fig. 2-16) that creates poor AC grounding and cause significant feedthrough between the input and output of the resonator. From Fig. 2-17 (left), feedthrough caused by large values of R_{Vp} can completely suppress the resonance peak of the gyroscope.

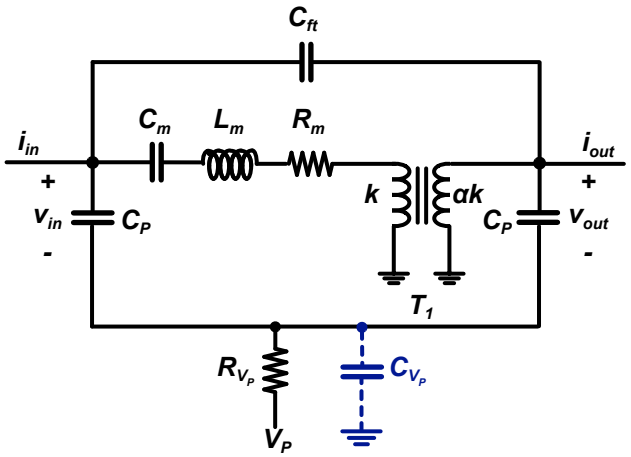

Figure 2-16 – Equivalent circuit model of the drive mode if on-chip circuitry is used to bias V_P and/or other tuning electrodes. The large resistance R_{VP} creates poor AC grounding and significant feedthrough between the input and output ports. To compensate for this poor grounding, a large shunt capacitance C_{VP} is added to provide a low-impedance AC ground path at high frequencies.

To compensate for the feedthrough introduced by the DC voltage generators, it is necessary to improve the existing AC ground path by reducing R_{VP}. This can be done by adding a large capacitance C_{VP} in parallel with the generator that is directly connected to ground. At high frequencies, the impedance of this pathway will be significantly lower than R_{VP}, and the feedthrough effect can be minimized (Fig. 2-17, right).

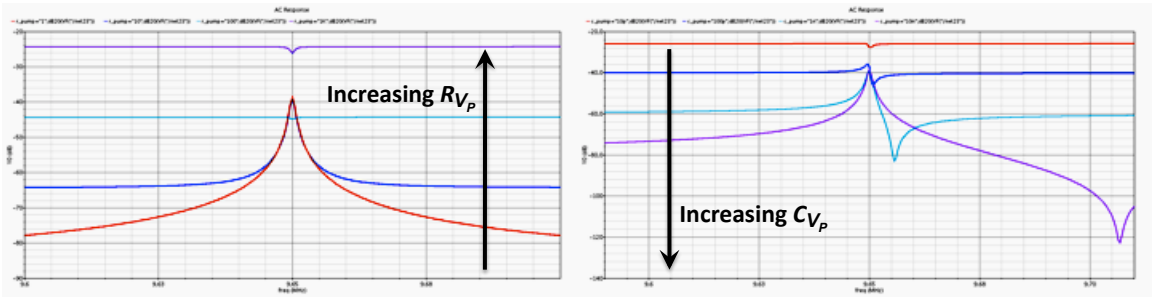

Figure 2-17 – (left) Effect of feedthrough created by introduction of large R_{VP} from DC voltage generation circuitry. (right) Suppression of signal feedthrough from introduction of C_{VP}.

2.3.4. Sense Channel Equivalent Circuit Model of BAW Gyroscope

As mentioned in Chapter 2.3.3.1, the sense channel can be modeled as a resonator with lumped element components defined by the Q (2-13), ω_0 (2-14), and R_m (2-15) of the sense resonance peak. However, unlike the drive loop, the sense electrodes are not connected as a feedback loop to excite the gyroscope into oscillations; rather, they are connected as an open-loop channel that is used to amplify and demodulate the Coriolis signal.

Assuming mode-matched operation, it is expressed in (2-1) that the sense electrode has two inputs – $y_{quadrature}$ and $y_{Coriolis}$. Furthermore, it has been shown that $y_{quadrature}$ (2-5) is a component of the gyroscope drive signal, while $y_{Coriolis}$ (2-8) is an amplitude-modulated sinusoid with a carrier frequency 90º out-of-phase with the drive signal. Lastly, because both the quadrature and Coriolis signals are dependent upon the drive

amplitude, the sense channel must be modeled with the drive loop already excited into self-oscillation.

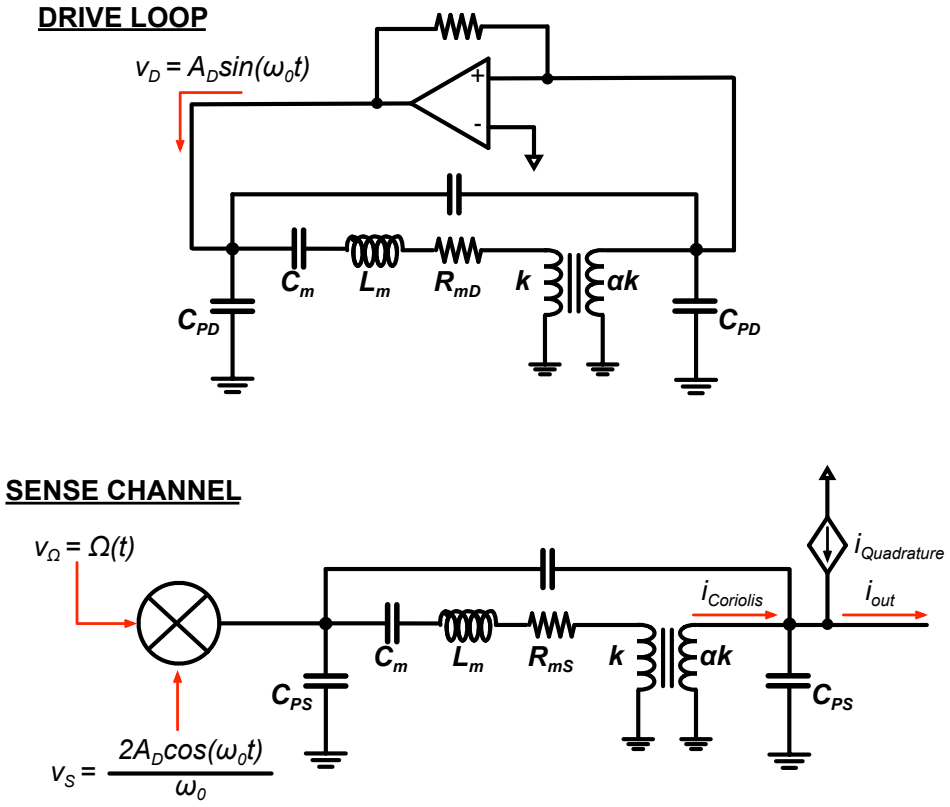

Figure 2-18 – Equivalent circuit model for BAW gyroscope sense channel.

Figure 2-18 shows the equivalent circuit diagram of the sense channel, in which the output current (i_{out}) of the sense electrode is taken as the sum of the Coriolis and quadrature currents. From the model, the quadrature current $i_{quadrature}$ is defined as

$$i_{quadrature} = \frac{k_Q V_D}{R_m}, 0 \le k_Q \le 1 \qquad (2\text{-}19)$$

where the V_D/R_m term provides the output current of the drive loop, and k_Q is a constant term to scale the drive current closer to the estimated quadrature of the gyroscope. The Coriolis signal is derived from the multiplication of the rate signal v_Ω with the drive velocity v_D, as presented in (1-1). The amplitude-modulated signal is passed through the

equivalent model for the sense resonator, which generates the Coriolis current component. From the model, $i_{Coriolis}$ is defined as

$$i_{Coriolis} = \frac{2A_D \cos(\omega_0 t)}{\omega_0 R_m} \tag{2-20}$$

where A_D represents the voltage amplitude of the drive oscillations.

For many calculations and simulations, implementing the sense channel model as presented in Fig. 2-18 can consume significant computing resources and time. In these cases, it is justifiable to use a simplified implementation of this model, in which two ideal current sources are used to generate $i_{quadrature}$ and $i_{Coriolis}$ with currents defined by (2-18) and (2-19), respectively. Using current sources eliminates the need for the drive loop in the sense channel model, which frees up available resources and saves significant simulation time.

CHAPTER 3

GYROSCOPE READOUT AND CONTROL CIRCUIT

The operation of a mode-matched, interfaced z-axis gyroscope can be summarized as follows: first, the device is driven with constant velocity at its resonance frequency along the x-axis. While the device is vibrating, any rate applied along the z-axis (the sensitive axis) will result in an amplitude-modulated (AM) Coriolis current signal generated along the sense (y-) axis that is modulated about the drive frequency. This output current is amplified, demodulated, and low-pass filtered to extract the Coriolis (rate) signal [34].

Figure 3-1 – Gyroscope testing setup.

Figure 3-1 shows the setup used for gyroscope testing and characterization. The sensor is placed inside an Ideal Aerosmith rate table that can apply constant or sinusoidal rates up to 500 °/s at temperatures from -60 °C to 150 °C. Next to the rate table are the test and measurement equipment – power supplies, signal generators, network analyzers,

oscilloscopes, and computers. Lastly, if the gyroscope is unpackaged and requires any level of vacuum, the vacuum pump at the bottom of the screen is connected to a small chamber inside the rate table that houses the device in a sub-mTorr environment.

In this chapter, an overview of the necessary blocks needed to interface with a gyroscope (Fig. 3-2) is presented. First, an outline of the basic interface circuitry is given. The drive loop will be introduced and system requirements needed to excite the gyroscope into self-oscillation are given. This is followed by a discussion of the sense channel and the techniques used to amplify the Coriolis signal and optimize noise performance. Finally, an overview of the demodulation and filtering blocks is provided. After presenting the interface circuitry, this section will review PCB design strategies to consider for optimizing performance when testing the gyroscope in an environment similar to Fig. 3-1.

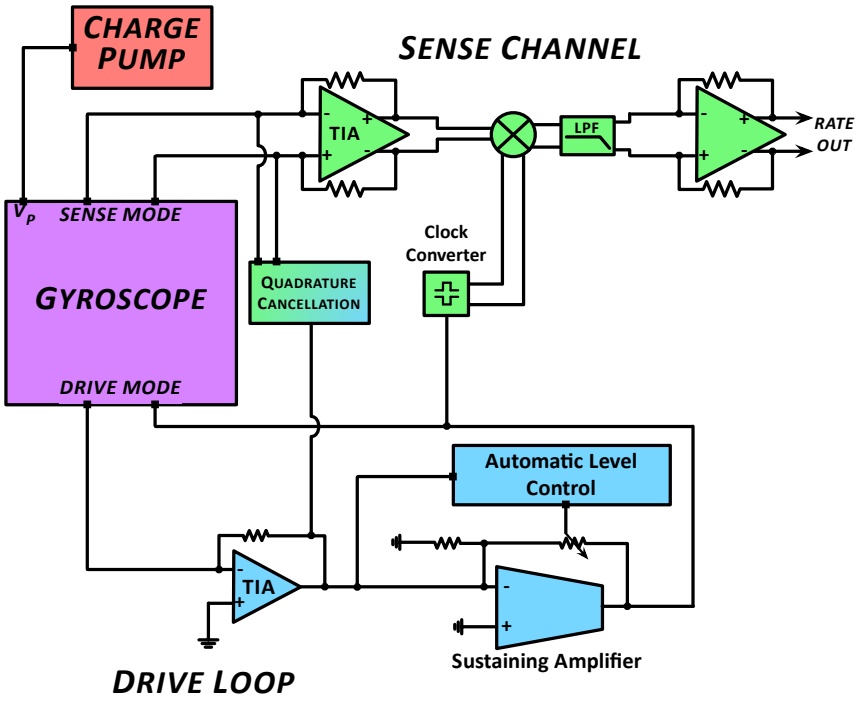

Figure 3-2 – Block diagram of gyroscope interface.

3.1. The Drive Loop

The drive mode of a gyroscope can be actuated using either of two methods. In the first method, an external source (i.e. function generator, network analyzer, etc.) directly applies a signal at the gyroscope resonance frequency. This method is often described as open-loop testing because no feedback is applied between the gyroscope and the actuator, leaving no method for controlling frequency drift. However, because the signal is coming from an external source, high voltages can be directly applied without any design concerns. With the second method, a loop is created that locks into the resonance frequency of the drive mode of the gyroscope. This method is typically used in CMOS ASIC design because the loop automatically adjusts to match any minute changes in the resonance frequency without assistance from an external frequency generator.

The drive loop (Fig. 3-3) is best described as an unstable closed-loop feedback system used to excite MEMS gyroscopes and other MEMS resonant devices [51-53] into self-oscillation for clocking or sensory applications.

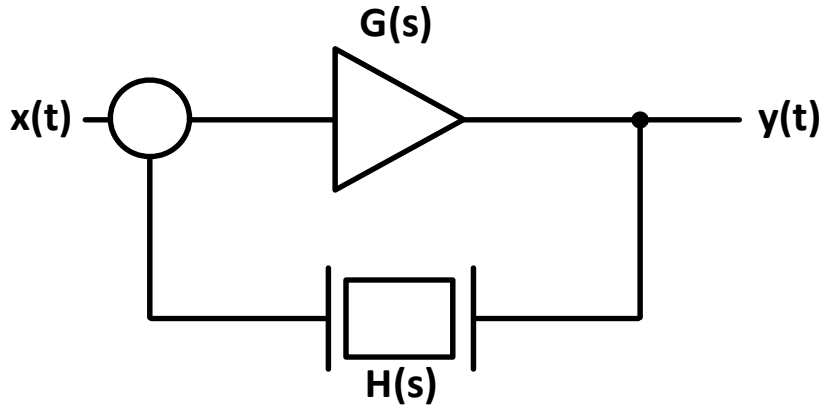

Figure 3-3 – Block diagram of gyroscope (resonator) drive loop.

The transfer function of the drive loop can be mathematically expressed as

$$\frac{Y(s)}{X(s)} = \frac{G(s)}{1 + G(s)H(s)} \tag{3-1}$$

Here, *x(t)* represents the noise generated from the amplifier and power supply while *y(t)* represents the oscillator output waveform. Additionally, *G(s)* and *H(s)* represent the transfer functions of a sustaining amplifier (i.e. controller) and the gyro/resonator (i.e. sensor), respectively.

In a closed-loop circuit or system, oscillations will occur if the feedback loop becomes unstable, given by

$$G(s)H(s) = G(j\omega)H(j\omega) = -1 \tag{3-2}$$

where *G(s)H(s)* is referred to as the loop gain of (3-1). If (3-2) is substituted into (3-1), the denominator simplifies to zero, creating an unstable solution. From this solution it can be concluded that the transfer function of the closed loop will become unstable if

$$\left|G(j\omega)H(j\omega)\right| \geq 1 \tag{3-3}$$

and

$$\angle G(j\omega)H(j\omega) = 0° \; or \; 360° \tag{3-4}$$

where $|G(j\omega)H(j\omega)|$ and $<G(j\omega)H(j\omega)$ represent the loop gain and phase of the system, respectively. Collectively, (3-3) and (3-4) are defined as Barkhausen's criteria [54].

As *x(t)* is amplified and passed to the gyroscope, the inherent band pass filter response of the device will attenuate the signal at all frequencies except resonance (ω_0). This remaining component is fed back to the amplifier, where positive feedback ($|H(j\omega)|>1$) applied via the sustaining amplifier is used to compensate for any signal attenuation at ω_0. As a result, the loop begins to amplify its own noise components at ω_0 indefinitely [55], which is seen at *y(t)* as a sinusoidal waveform increasing in amplitude. The signal at ω_0 will grow over several cycles until non-linearity in the circuit or the resonator brings the system to a steady-state oscillation at ω_0.

Based on (1-5), the drive loop of the BAW gyroscope does not contribute significantly to sensor ENEΩ - it is only responsible for providing a constant AC signal with a large, time-invariant vibration amplitude ($v_{ac} \approx V_{DD}$). It can be argued that because the drive loop is responsible for controlling the vibration amplitude of the disk and demodulating the Coriolis signal, minimizing the loop phase noise or reducing signal jitter through use of a PLL will reduce phase noise effects on the sense channel that show up through amplitude variation or signal multiplication, improving system performance. Although this is true, the phase noise of the sensor is more dependent on Q_{drive} of the gyroscope [56], meaning that a well-designed device provides greater reduction in system phase noise and signal jitter than a low noise drive chain. Furthermore, the loop phase noise will have less effect when referred back to the sensor input due to the high gain of the sense TIA. Consequently, the design of the BAW disk gyroscope drive chain focuses primarily on developing low power, high gain, and high bandwidth circuits with a large signal swing. To that end, a single-ended drive chain is interfaced with the gyroscope (Fig. 3-2), as it requires less power than a differential chain.

To excite the gyroscope into self-oscillation, a trans-impedance amplifier (TIA) is connected in positive feedback with the drive mode of the gyroscope. A TIA provides two advantages over other circuit architectures that can be used to interface with the gyroscope. First, the shunt-shunt feedback topology of the TIA converts an input current signal into a voltage that is fed back to the input of the gyroscope. The current-to-voltage conversion is ideal for any capacitive resonator, which generates a current output for any voltage applied to its input terminal at resonance. Secondly, the shunt/shunt feedback of

this architecture implies low circuit input and output impedances, minimizing the load from the parasitic capacitances at the input and output of the gyroscope.

After the TIA, one or more sustaining amplifiers are cascaded to the drive chain for the primary purpose of providing any additional gain and phase shift needed by the drive loop to generate and sustain self-oscillations. In addition to supplementing these requirements, sustaining amplifiers are designed for use in more sophisticated drive loop functionality, such as rail-to-rail operation of the drive loop oscillations across the large capacitive load of the gyroscope (which can cause slewing) and automatic level control of the drive loop amplitude. These are discussed in further detail in Chapter 4.

3.2. The Sense Channel

Unlike the drive chain, which is optimized for low power and designed for a high gain-bandwidth to excite the gyroscope into oscillation, the sense channel is designed for low-noise amplification. For low rotation rates, the sensor cannot detect the rate signal once the noise generated by the IC becomes larger than Coriolis current; therefore, to achieve the best sensor resolution and minimum level of detection, the input referred current noise of the sense amplifier chain must be as low as possible.

Generally speaking, it is best to implement the sense channel differentially because of the benefits fully-differential operation provides with common-mode noise suppression and power supply rejection. However, fully-differential operation alone is not adequate if the ASIC is to reach navigation-grade performance, which requires an input referred noise performance on the order of 100 fA/√Hz (Chapter 7). Therefore, a closer look at the sense channel is needed to understand the best strategy for minimizing both the input referred noise and power consumption of the ASIC.

3.2.1. Noise Optimization of the Sense Channel

Noise optimization of the sense channel requires identifying which component of the ASIC will most affect the input referred noise, particularly as the frequency of interest is scaled from the kHz to the MHz regime. This component is typically interfaced directly with the sensor, which in the case of the gyroscope (Fig. 3-2) is the sense input TIA. For the architecture shown in Fig. 3-4, the gain of the sense TIA is defined as

$$A_{TIA} = \frac{V_{OUT-TIA}}{I_{IN-TIA}} = -R_{F-SENSE} \tag{3-5}$$

with a 3dB bandwidth (BW) proportional to

$$BW \propto \frac{g_m}{C_L} \tag{3-6}$$

where g_m and C_L represent the trans-conductance of the TIA input stage and the capacitive load of the gyroscope at the TIA input, respectively. With its large gain, any noise contribution from subsequent blocks of the chain is attenuated when referred back to the input and divided by the gain of all preceding stages (including A_{TIA}). Input noise reduction consequently focuses on minimizing the noise contribution of the sense TIA.

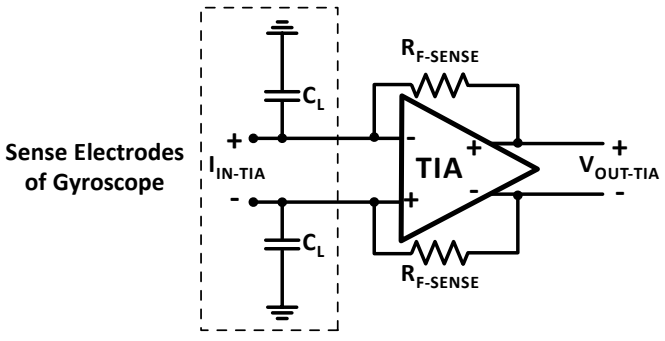

Figure 3-4 – Diagram of sense channel input TIA.

It should be mentioned that although the sense TIA is the primary contributor of input-referred noise, it is important to consider the output noise across the rest of the

ASIC, particularly after demodulation and rate amplification. Here, the rate signal has been demodulated to baseband frequencies, leaving it susceptible to flicker noise from the mixer and rate amplifiers along the ASIC sense channel. Optimization of the post-demodulation amplifiers is not discussed in this thesis.

The generic input referred current noise profile of a CMOS interface TIA is shown in Fig. 3-5. Based on this plot, the noise performance can be divided into 3 regions – the flicker-dominant noise region, the thermal-dominant noise region, and the gain attenuated thermal-dominant noise region. As the operating frequency of the gyroscope is scaled higher, the flicker ($1/f$) noise of the CMOS process plummets and gives way to thermal noise as the primary noise contributor. At the thermal noise region, the input referred noise remains flat until the frequency extends beyond the 3dB bandwidth of the TIA, at which point the gain of the amplifier attenuates and causes the input referred noise to increase once again. Depending on the operating frequency of the gyroscope, the input referred noise can be localized to one of two regions of interest for which to focus on noise optimization.

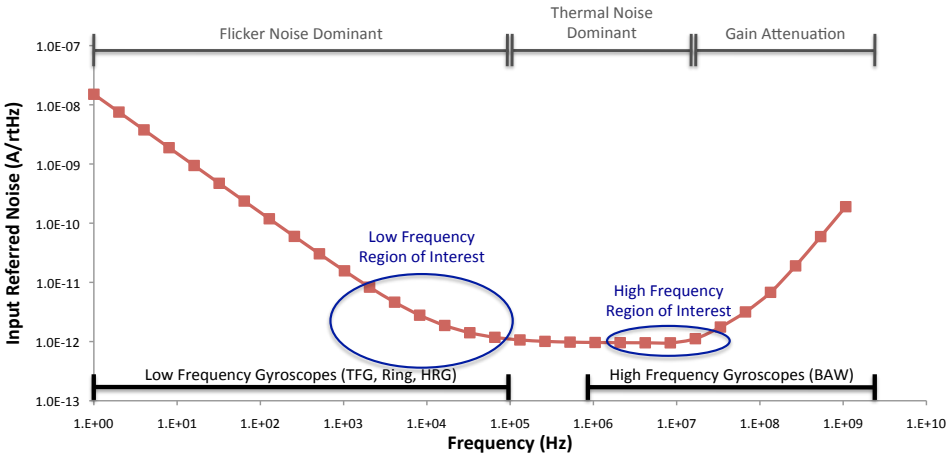

Figure 3-5 – Input referred noise profile of CMOS interface ASIC. The noise can be broken down into three regions of interest that are identified at the top of the graph, while the type of gyroscope that operates in that particular region is identified at the bottom of the graph.

3.2.1.1. Optimization of the Sense Channel for Low Frequency Gyroscopes

At low frequencies, the TIA power consumption is not the largest concern, as design techniques (i.e. sub-threshold operation) can be applied to reduce the current needed for the IC to meet the gain and bandwidth needs of the gyroscope. Instead, more emphasis is placed on minimizing the input referred noise of the TIA, which is limited to operating in the flicker-dominant (1/*f*) noise region of Fig. 3-5. The *1/f* noise is given by [57]

$$i_{n,inF}^2 = \frac{K_f}{C_{ox}WL}\frac{1}{f^{\alpha_f}} \tag{3-7}$$

Here, K_f, C_{ox}, W, L, and α_f represent the flicker noise coefficient, gate oxide capacitance input transistor width, input transistor length, and flicker noise frequency slope, respectively.

For low frequency operation, it is desirable to push the flicker noise corner frequency as close to 0 Hz as possible. This increases the likelihood of operating the sensor in the in the thermal noise regime, where the IC can be more readily scaled down to navigation-grade levels of noise performance. Table 3-1 shows a breakdown of these flicker noise parameters in NMOS transistors as the process minimum feature size is reduced from 0.35 μm to 90 nm [57-59]. This data suggests that as process size (L) reduces, both K_f and α_f remain constant (+/- 20% variation) and do not significantly affect the input referred noise. Instead, the flicker noise shows a linear dependence to C_{ox} and transistor area (W, L_{min}). As the feature length is scaled down, the gate oxide thickness (t_{ox}) becomes smaller, causing C_{ox} to increase and reducing $i_{n,inF}^2$. However, if transistor size is continuously adjusted to keep with minimum feature lengths, $i_{n,inF}^2$ will increase quadratically as W will be repeatedly reduced to maintain a constant W/L_{min}.

Table 3-1 – Breakdown of flicker noise parameters for various CMOS processes [57-59]

Process (L_{min})	K_f	α_f	C_{ox}
0.35 µm	1×10^{-24} J/Hz	1	4.8 fF/µm^2
0.25 µm	7×10^{-25} J/Hz	0.85	6.4 fF/µm^2
0.18 µm	1×10^{-24} J/Hz	0.9	8.8 fF/µm^2
0.13 µm	1.5×10^{-24} J/Hz	0.85	14.8 fF/µm^2
0.09 µm	7×10^{-25} J/Hz	0.85	18 fF/µm^2

To optimize the input-referred noise for low frequency gyroscopes, it is best to maximize W and L to increase the area of the transistors making up the sense TIA (Fig. 3-6). Because of the quadratic relationship between area and flicker noise, this will create the largest flicker noise reduction and push the corner frequency closer to 0 Hz. If system size is limited, W and L should remain unchanged so that only C_{ox} (which increases as L_{min} is reduced) will affect the flicker noise. With this method, both the flicker noise and $1/f$ corner frequency will decrease linearly with L_{min} (Fig. 3-7). To decrease the input referred noise further at low frequencies, it is recommended that PMOS transistors are implemented instead of NMOS for the TIA input, as K_f is smaller and α_f larger for PMOS transistors of equivalent process size [57].

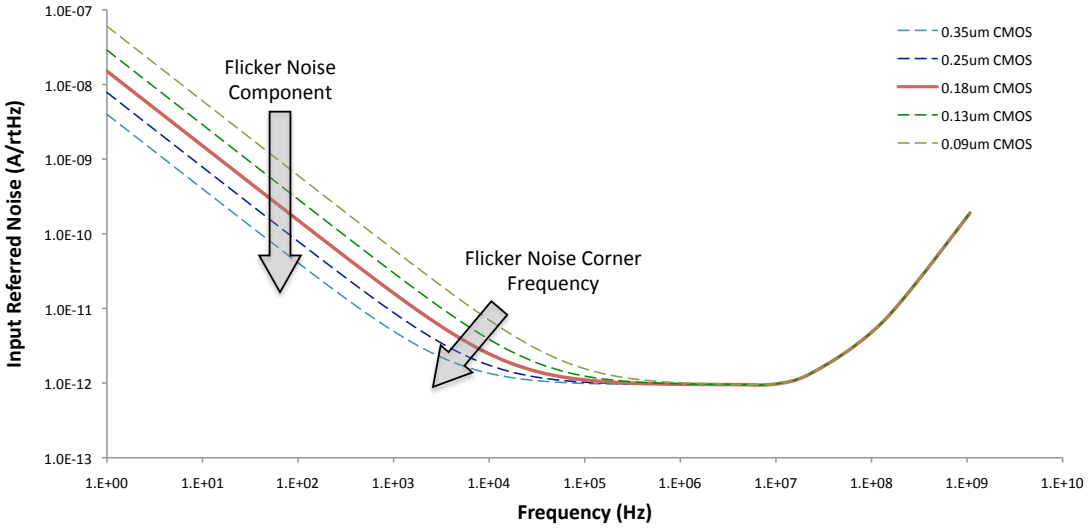

Figure 3-6 – Reduction in flicker noise and flicker noise corner frequency due to increasing W, L. In this figure, the W/L ratio is kept the same as the minimum feature size of the transistor is varied between L_{min}=0.35µm and L_{min}=0.09µm.

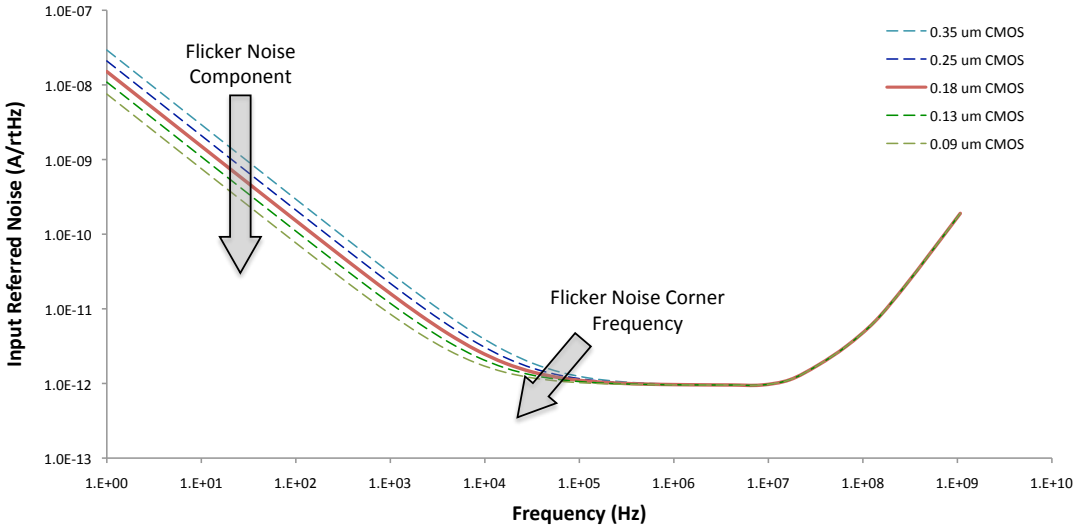

Figure 3-7 – Reduction in flicker noise and flicker noise corner frequency due to constant *W*, *L* and increasing C_{ox}.

3.2.1.2. Optimization of the Sense Channel for High Frequency Gyroscopes

To optimize noise and minimize power consumption for high frequency gyroscopes, the TIA should be designed to operate in the thermal-dominant noise region, as close to the gain attenuation region as possible. This ensures that the TIA will operate under optimal noise conditions, while power is not unnecessarily wasted on extending the thermal noise region beyond the region of interest.

With the region of interest identified, the next step in optimizing the TIA noise performance is to reduce the thermal noise as much as possible. From [60], the input referred thermal noise current of a TIA can be given as

$$i_{n,inT}^2 = \frac{8kT}{3g_m R_F^2}\Delta f \qquad (3\text{-}8)$$

where k, T, g_m, and R_F represent Boltzmann's constant, the ASIC temperature, the transconductance of the input stage of the TIA, and the feedback resistance of the TIA, respectively. The transconductance g_m can be defined as

$$g_m = \sqrt{2K\frac{W}{L}I_D} \tag{3-9}$$

where K, W, L, and I_D are the current drive strength of the input transistor, the transistor width and length, and the current dissipated by the transistor, respectively.

Equation (3-8) suggests that if the sensor is operating in the thermal noise regime, the input referred noise will be independent of the device operating frequency. However, by substituting (3-6) into (3-8) it can be seen that there is a linear relationship between bandwidth and input referred noise. Additionally, substituting (3-6) into (3-9) suggests a square-root proportionality between BW and power. Designing the optimal operating frequency of the gyroscope to be as low as possible (low MHz) can compensate for both these dependencies. The noise and power can also be improved if the load capacitance of the gyroscope is reduced, thereby pushing the dominant pole of the gyroscope (and the gain attenuated region of input referred noise) to higher frequencies.

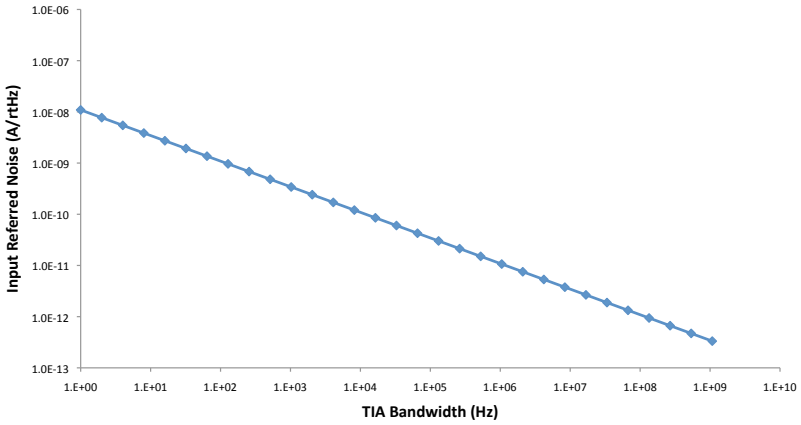

Figure 3-8 – Log-log plot of input referred noise dependence on TIA bandwidth. For high frequency gyroscopes, the input referred noise of the TIA is linearly proportional to the 3dB bandwidth of the TIA, which is approximately set to the operating frequency of the gyroscope.

Once the operating frequency is defined, the TIA design should focus on optimizing R_F, which has a quadratic effect on the input referred noise (Fig. 3-9). This task is very challenging, as any changes made to R_F create a tradeoff between the resolution and full-

scale range of the sensor. This challenge is magnified when considering the effect of quadrature, which introduces a large, undesired current component to the sense input that compresses the gain of the amplifier and further reduces the dynamic range attainable by the ASIC. If R_F is limited due to FSR or quadrature, any improvements in noise performance must be attained by increasing g_m (and consequently, I_D) (Fig. 3-10).

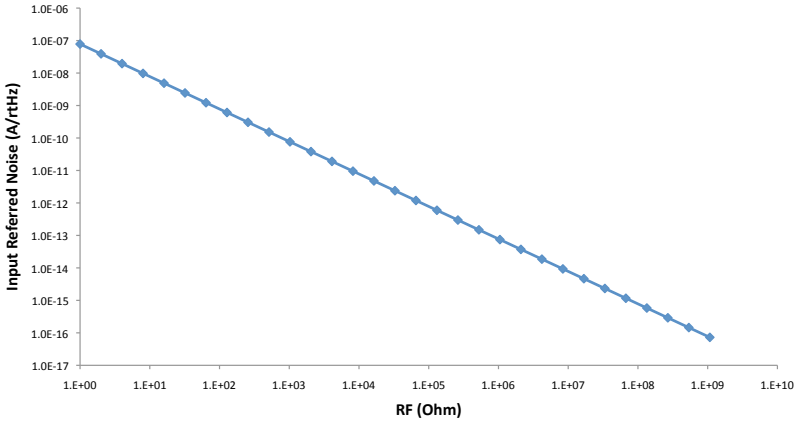

Figure 3-9 – Log-log plot of input referred noise dependence on R_F. For high frequency gyroscopes, the input referred noise of the TIA is proportional to R_F^{-2}.

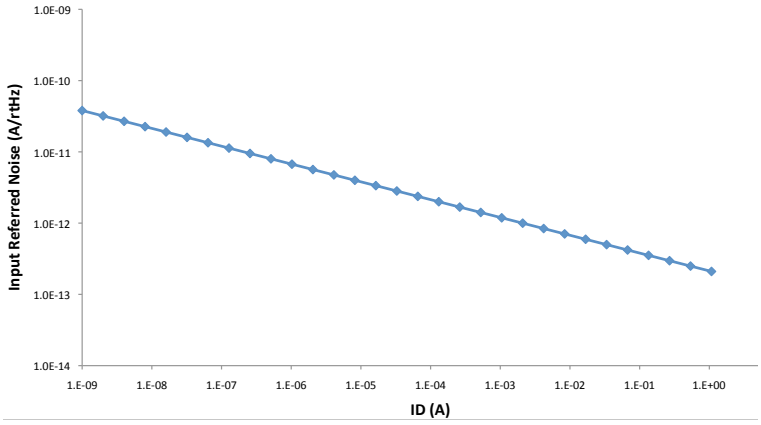

Figure 3-10 – Log-log plot of input referred noise dependence on I_D. For high frequency gyroscopes, the input referred noise of the TIA is proportional to $\sqrt{I_D}$.

To achieve the best noise and power performance from the sensor, it is necessary to make R_F as large as possible, as any increase in R_F does not directly impact the power consumption of the ASIC. Quadrature cancellation thus becomes an important

component of the sense channel because it reduces the quadrature error at the sense TIA input, permitting a larger feedback resistance to be implemented across the sense TIA. If the quadrature error is minimized, then R_F becomes solely dependent on the full-scale range specification of the sensor, and the current (power) necessary to achieve the desired performance level for the gyroscope will be minimized.

3.3. Demodulation and Filtering

At the output of the sense TIA, the amplitude-modulated Coriolis signal can be expressed as

$$V_{Coriolis}(t) = A_S \sin(\omega_0 t)\sin(\omega_r t) \tag{3-10}$$

where A_S and ω_r denote the modulation depth and frequency of the amplitude-modulated (rate) signal. Using trigonometric identities, (3-8) can be also expressed as

$$V_{Coriolis}(t) = \frac{A_S}{2}\left[\cos\left((\omega_0 - \omega_r)t\right) - \cos\left((\omega_0 + \omega_r)t\right)\right] \tag{3-11}$$

To extract the rate signal, the output of the sense channel is passed to the LO input of a demodulator. Depending on the design criteria, the two most viable design choices for the mixer include the Gilbert Cell [61], which offers a high conversion gain at the cost of non-negligible power consumption, and the quad-switching demodulator [62], which consumes no power and offers high linearity, but comes with the drawback of a conversion loss due to its passive switching implementation. The output of the drive loop, which is matched to the Coriolis carrier frequency, is passed to a clock generator (Fig. 3-11) that generates two non-overlapping, square-wave clock signals to be used as the RF (CLK) inputs of the demodulator based on the delay created by the NAND gate

and inverters in the feedback path [63]. When both inputs to the mixer are applied, the demodulator will multiply the two signals and give

$$V_{out,mixer}(t) = \frac{A_S}{2}\left[\cos\left(\left(\omega_0 - \omega_r\right)t\right) - \cos\left(\left(\omega_0 + \omega_r\right)t\right)\right]\sin\left(\omega_0 t\right) \tag{3-12}$$

which can be simplified to

$$V_{out,mixer}(t) = \frac{A_S}{4}\left[\sin\left(\left(2\omega_0 - \omega_r\right)t\right) + \sin\left(\left(2\omega_0 + \omega_r\right)t\right) + 2\sin\left(\omega_r t\right)\right] \tag{3-13}$$

Following the mixer stage, a low pass filter is used to filter the high frequency $2\omega_0+\omega_r$ components of the output signal, reducing the output signal to

$$V_{out,mixer}(t) = \frac{A_S}{2}\sin\left(\omega_r t\right) \tag{3-14}$$

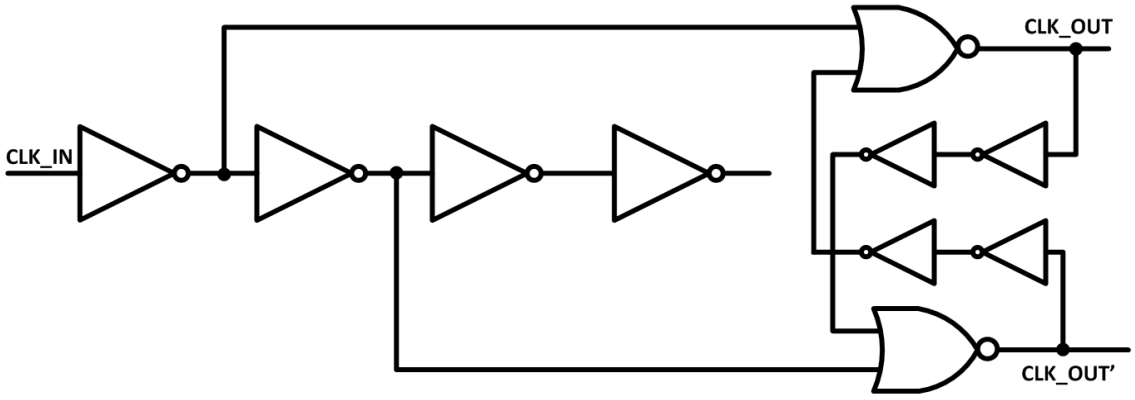

Figure 3-11 – Block diagram of non-overlapping clock converter.

3.4. PCB Design and Interfacing

A printed circuit board (PCB) connects electronic and/or mechatronic components together to perform a specific function by using signal traces etched onto a conductive film (typically copper) that is deposited over a non-conductive substrate. PCBs are widely used in both industry and academia to assemble electrical circuits and systems due to their low cost and high reliability.

To characterize the sensor, pads from the IC and the gyroscope are wirebonded to the PCB and routed through its on-board traces to other terminals. Consequently, PCB traces and other components on the PCB can introduce unwanted feedthrough that degrades the Coriolis signal coming from the gyroscope. Although quantifying and characterizing this PCB error is not a focus of this thesis, it can be said qualitatively that the error is dependent on the design and layout of the PCB itself. Here, several steps are provided to reduce the error component from the PCB with the hopes of both improving the overall resolution of the sensor and educating future designers on the importance of careful PCB design.

In this sub-section of gyroscope interfacing, a discussion of design techniques and challenges specific to gyroscope PCB design and testing is presented. The section then introduces several other possible sources of error that are created off-PCB.

3.4.1. Determining PCB Size

Designing a PCB is very similar to designing the topcell for an IC – both require careful planning to ensure the desired results. This begins with considering the dimensions of the PCB. In terms of board size, it is usually best to make the board as small as possible. Obviously the cost of the PCB will increase with the PCB size, but reducing the size of the board will also reduce the size of its largest traces, thereby mitigating some of the effects of electromagnetic interference (EMI) and RF interference (RFI) [64]. Reducing trace length will also minimize the noise associated with the transmission line effects of each trace [65] and force the designer to populate the board with smaller active and passive components that will contribute less noise to the signals routed on the PCB. However, the PCB size is also dependent upon on what shape the

board must be and how the board will be tested. Therefore, the dimensions of a PCB should be determined carefully so as not to exceed the smallest size and shape necessary to perform its given function in its given environment.

3.4.2. Multi-Layered PCBs

In addition to choosing the size of a PCB, multiple copper films can be deposited to create a multi-layered board where each layer provides an independent plane to route signals. By providing such planes, multi-layered boards can reduce the noise and EMI radiated from each current loop on the PCB [66, 67], which are created by current moving between its source and destination through a trace etched on the PCB and then returning back to its source through the ground traces. The magnitude of the radiated noise is dependent upon the impedance of this loop, which is minimized by creating one or more dedicated ground planes underneath the top layer of the board that effectively provide the shortest return path between source and destination [66].

For designing gyroscopes and other resonant systems, 4-layer and 6-layer boards allow ground planes to be placed between any critical traces (i.e. power, signal) and make the PCB design process simpler. However, additional board layers can be very costly, and it is often possible to provide the necessary grounding by using only a 2-layer PCB [67]. This will depend on the complexity of the board, particularly the number of signals that are being processed on the PCB (i.e. single-axis gyro vs. multi-axis gyro vs. IMU) as well as the components placed on the board (analog, digital, or mixed-signal).

3.4.3. Connectors

Several connectors – including SMAs, BNCs, and D-Subs – can be used to interface the PCB with the external supplies and testing equipment. Depending on the design,

twist on connectors (SMA, BNC) typically work best with high-frequency connections, as the shielding afforded to the signal by the connector is specifically designed for high-frequency operation. These connectors also have the advantage of being easily connected up to most testing equipment (i.e. network analyzers, power supplies, function generators). D-Sub connectors, on the other hand, may or may not have enough shielding available to ensure a clear high-frequency signal near and above 1 GHz, but can still provide good signal in the kHz and MHz regimes as long as a well-established low-impedance ground connection is provided near each input and output terminal.

When applying and measuring signals using BAW gyroscopes and other inertial sensors, screw-in connectors do not work well. Inertial sensors are tested in environments with significant vibration or rotation, and in these environments the SMA and BNC connectors on the PCB can get loose and worn over time and not form as tight a connection with the external cables as they once did. If this occurs, it is possible that applying an inertial force may cause the contact between the SMA connector and the wire to move and by doing so weaken or break the connection, which would clearly affect the signal output. It has also been shown that with certain wires (particularly BNC connectors), pulling from the cables may cause either board flex or piezoelectric strain on the cables, which has been shown to affect the operation of resonant MEMS devices [68].

D-Sub connections provide a strong fixed connection that remains secure over time (even with heavy use). Additionally, for the several input and output connections of the PCB, the stress applied through rotation or acceleration will be felt strongest where the male and female pins are connected, but their effects can be neglected with the use of long, thin wire that does not place much stress on the board.

3.4.4. Placing Components and Routing

After the board size and shape are determined and the number of board layers has been selected, it is important to carefully place and route all components on the PCB. Critical circuits and system blocks should be placed first to make sure that routing can be optimized and minimized (to reduce noise) before less important sections are addressed. The most important system of the gyroscope is the sense channel, for which keeping the noise of the input current and subsequent voltages minimal is critical for getting the best resolution. Therefore, these components should be placed closest to the IC and the MEMS device. After placing the components, the next step in board design is to layout the ground plane, which must be well-routed to ensure minimum impedance for all circuit loops as described in Chapter 3.4.1.2,. After the ground plane come the power plane and the drive loop routing. It is critical that the drive loop be kept away from the sense channel traces to prevent any crosstalk between the two signals. Lastly, routing secondary signals such as V_P and V_{TUN} should be performed. When routing any signal, avoid drawing traces with 90° segments, which radiate stronger EMI than 45° or curved segments [64]. For DC voltages decoupling capacitors should be added between the supply and ground as close to each component as possible to filter out low and high-frequency ripple carried on the DC voltage by the power supply. Decoupling capacitors used to filter higher frequencies should be connected closer to the components than lower frequency decoupling capacitors.

CHAPTER 4

AN INTERFACE IC FOR BAW GYROSCOPE IN 0.18μM CMOS

As discussed in Chapter 2, the high resonance frequency scaling of the BAW disk gyroscope provides the sensor with unique advantages over the current state-of-the-art commercial gyroscopes. Primarily, the bandwidth of the gyroscope is extended while the MNEΩ is reduced significantly. Additionally, high-frequency operation opens up the possibility of hybridization, in which the gyroscope can act as both a rotation sensor and a clock in the system for which it is being used.

Despite these advantages, high-frequency devices introduce new challenges on the ASIC side of the system design (Chapter 3). In particular, the reduction of MNEΩ shifts the burden of noise optimization to the electronic component (ENEΩ) of the ASIC. Consequently, additional power is needed by the interface circuit to facilitate both high-frequency operation and ENEΩ reduction.

In this chapter, a low power, low noise interface ASIC (Fig. 4-1) for the BAW gyroscope is presented. The clocking performance of the loop is characterized, and challenges to optimizing the drive signal as a timing element are presented and discussed. To permit maximum sensitivity and reduce input referred noise, a technique is presented to remove any quadrature at the sense input, after which the resolution of this sensor is measured and characterized.

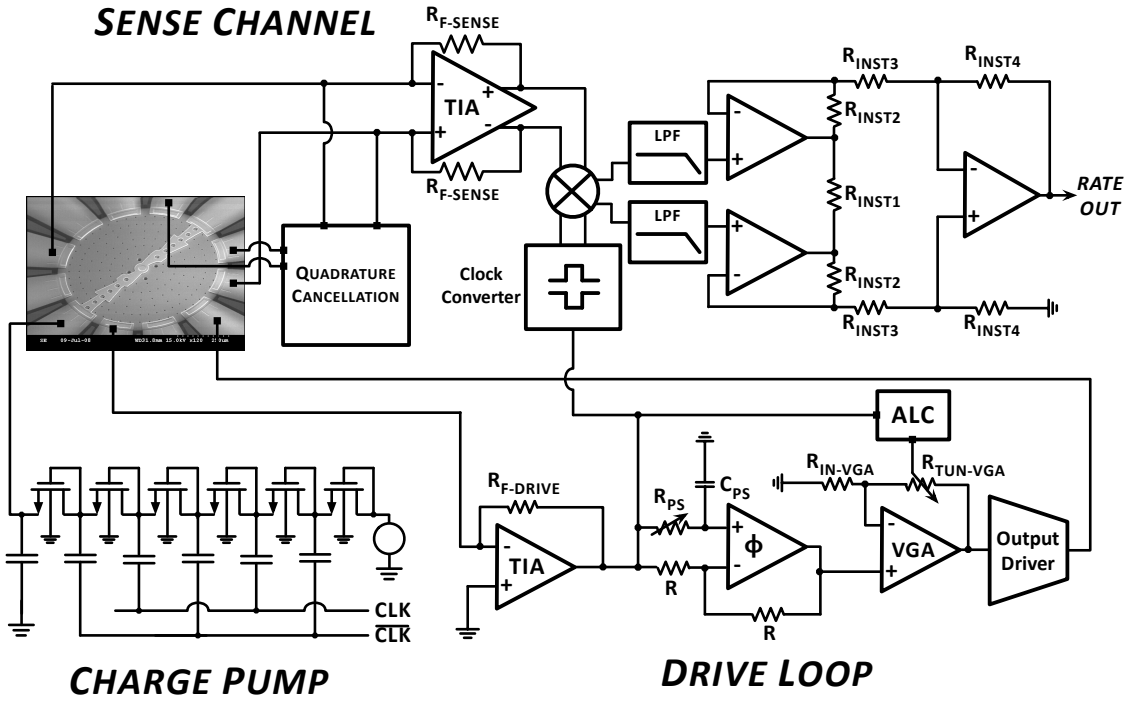

Figure 4-1 – Block diagram of complete interface ASIC for BAW gyroscope. The system includes circuitry for amplitude level control (ALC), quadrature cancellation, and DC voltage generation.

4.1. System Architecture

4.1.1. Drive Loop

As described in Chapter 3, drive chain design focuses on minimization of power consumption, as the noise of the loop does not significantly affect the resolution of the gyroscope. For this reason, the drive loop circuitry is designed as a single-ended architecture, which consumes less current (power) than a fully-differential design. Additionally, the single-ended configuration uses 2 fewer electrodes than the differential configuration (one at the input, one at the output), leaving additional electrodes of the disk open to match (via tuning) the two modes of the gyroscope or assist in quadrature cancellation. In this design, the electrodes are used for the latter purpose (Chapter 4.1.4).

The drive loop is composed of four blocks. First, the input TIA amplifies the

motional current generated by the gyroscope and converts it into a voltage. After amplification, the output is passed from the TIA to a phase shifter, which is followed by a variable gain amplifier (VGA). These two blocks are used to adjust the gain and phase shift of the drive loop to satisfy Barkhausen's criteria for oscillations ($A_{Loop} \geq 1$, $\theta_{Loop} =$ 0° or 360°) at ω_0. They also assist with automatic level control of the loop. After the VGA, the signal passed to an output driver and fed back to the disk.

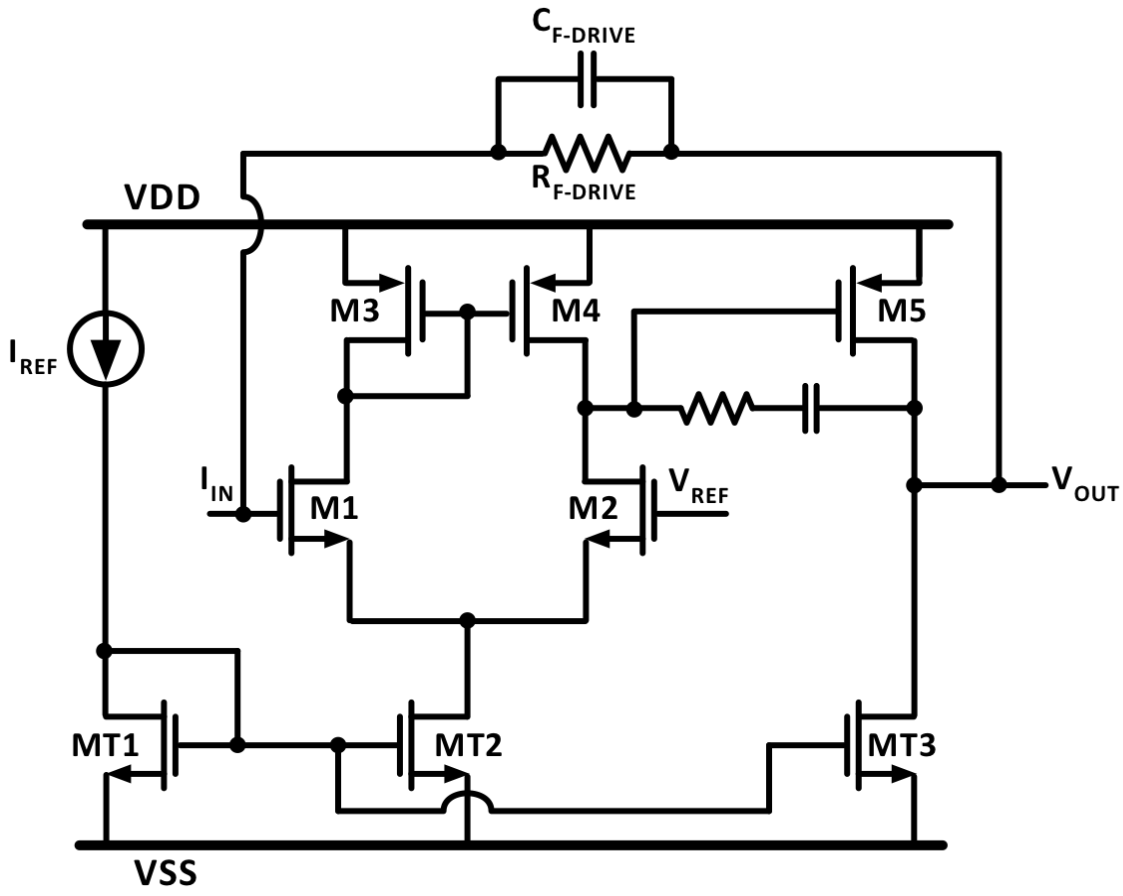

Figure 4-2 – Circuit diagram of input drive TIA.

The input TIA used in the drive loop is a 2-stage op-amp is made up of an input differential pair followed by an output common source stage (Fig. 4-2). Biasing currents and voltages for this op-amp and all other designs presented in this chapter are generated from a bandgap reference based on the design in [63]. A high-resistance poly-silicon

resistor (R_F = 35 kΩ) is connected in feedback between the input (I_{IN}) and output (V_{OUT}) terminals of the TIA. The poly-Si resistor was chosen to ensure that the signal at V_{OUT} remains linear, a necessary condition for proper amplitude level control of the drive loop as well as demodulation of the AM rate signal from the carrier in the sense channel.

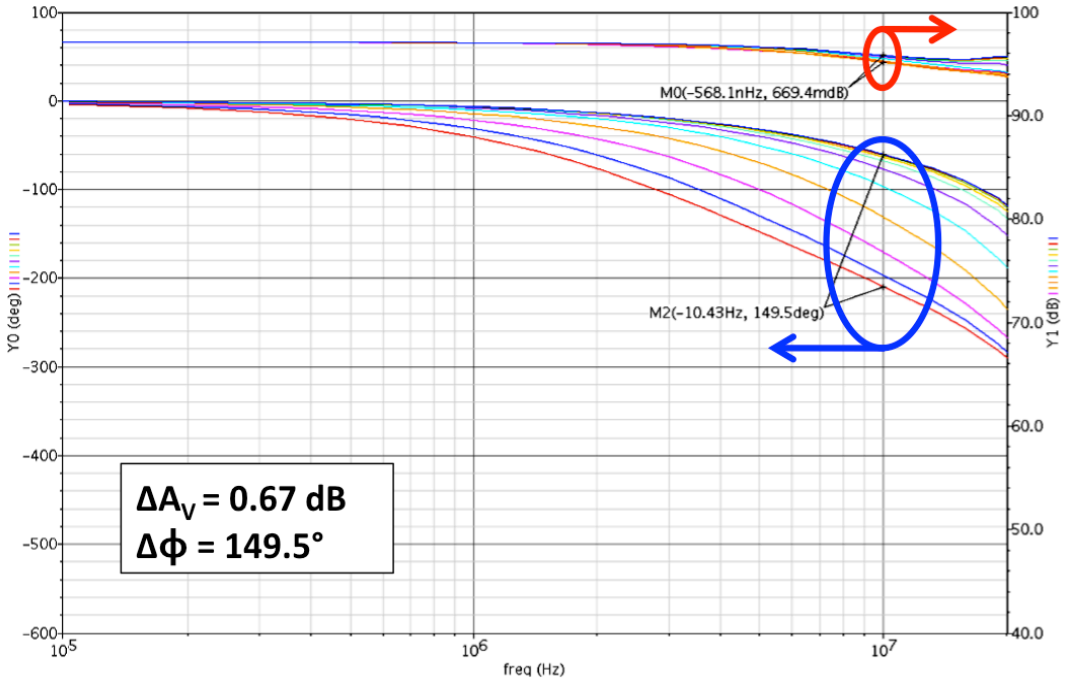

Figure 4-3 – Simulated AC gain and phase response of drive chain caused by phase shift tuning.

The phase shifter (Fig. 4-1) uses an all-pass filter architecture that contains the same core 2-stage op-amp design as the TIA. The transfer function of this circuit is given by

$$\frac{V_{OUT}}{V_{IN}} = \frac{1 - sR_{PS}C_{PS}}{1 + sR_{PS}C_{PS}} \qquad (4\text{-}1)$$

where R_{PS} and C_{PS} represent the resistor and capacitor at the positive terminal of the phase shifter, respectively. R_{PS} is made tunable through the parallel combination of a high-impedance poly-Si resistor and a MOS transistor, which operates in triode due to the feedback connection of the op-amp ($V_{DS} \sim 0$) and the application of a large tuning voltage ($V_{GS} = V_{TUN\text{-}VGA} - V_S > V_t$). Using an external voltage to adjust the resistance of the MOS

component of R_{PS} creates a proportional change in the phase shift ($\omega_0 = 1/R_{PS}C_{PS}$) of the circuit at resonance while the gain remains at unity, defined by the ratio ($A_{PS} = -R/R = 1$). Drive chain simulations (Fig. 4-3) across the operating range of $V_{TUN\text{-}VGA}$ (1-1.2V) show the phase shifter offers ~149° of phase tuning with <1 dB gain variation across the entire tuning range.

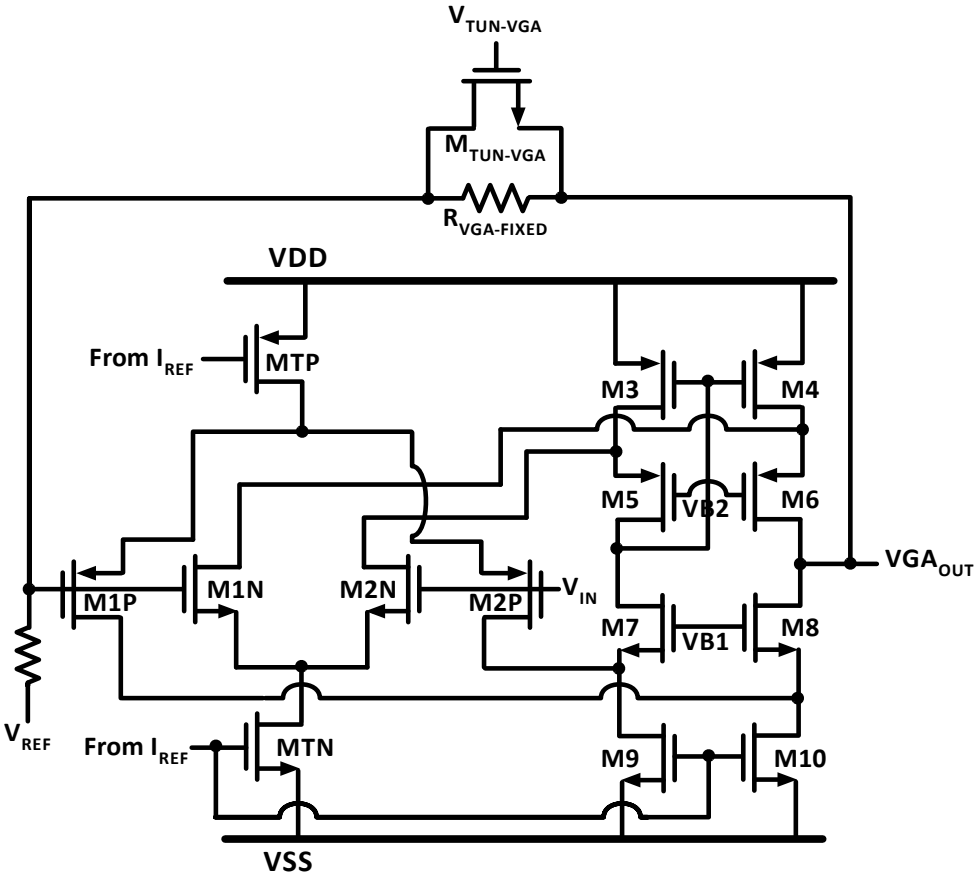

Figure 4-4 – Circuit diagram of VGA.

The VGA of the drive chain (Fig. 4-4) is used primarily for level control of the drive signal, which is discussed later in this chapter. Complementary NMOS and PMOS differential pairs are used to extend the input swing of V_{IN}, after which the currents from each differential pair are summed together through transistors M3-M10. $R_{TUN\text{-}VGA}$ (Fig. 4-1) is made from the parallel combination of $R_{VGA\text{-}FIXED}$ and $M_{TUN\text{-}VGA}$. By adjusting the

voltage $V_{TUN\text{-}VGA}$ of transistor $M_{TUN\text{-}VGA}$, the drive loop is simulated to provide a total gain variation of 19.89 dB (Fig. 4-5). It should be noted because of large signal operation, the output signal of the VGA does show nonlinearity in simulation for large input signals > $V_{DD}/2$. However, all system processing (ALC, demodulation) is done after the drive TIA, which remains linear across all expected current inputs. Furthermore, the VGA signal is primarily needed to provide a tunable signal to the output driver with maximum output voltage range, which is observed in the loop simulations shown in Section 4.1.2.

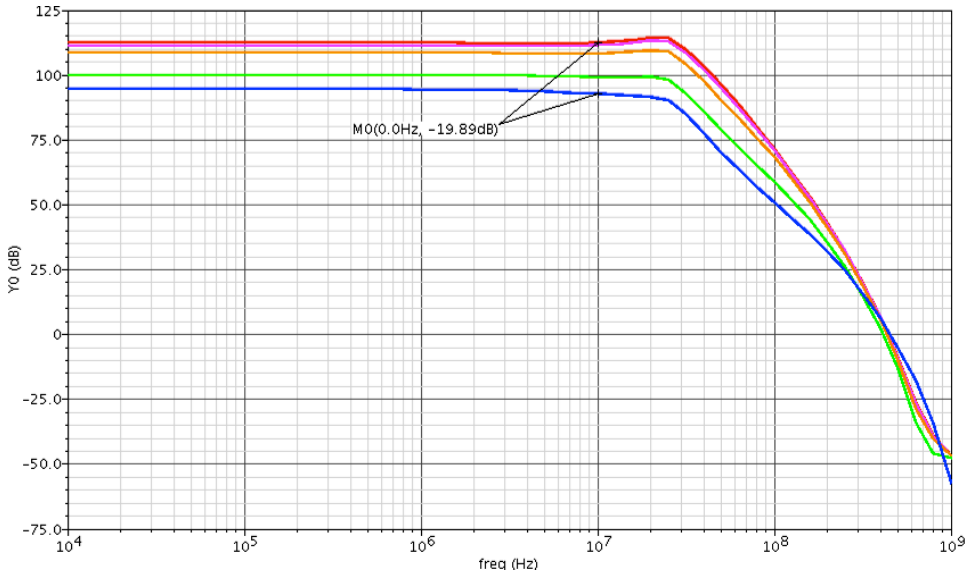

Figure 4-5 – Simulated AC gain variation from VGA. As $V_{TUN\text{-}VGA}$ is adjusted, the drive chain shows a tunable gain of ~ 20dB.

After the gain and phase settings of the drive signal are properly adjusted, the signal is passed to the output driver (Fig. 4-6), which is designed to drive it across the capacitive load of the gyroscope. The driver uses a simple inverter with shunt-shunt feedback topology to maximize the voltage swing of V_{OUT}, ensuring near rail-to-rail swing ($1.2V_{PP}$) for up to a 5pF load. To prevent slewing, the output driver draws a large amount of current, resulting in a large current consumption from this block. By keeping the drive loop single-ended, the ASIC avoids the need for two such buffers to drive the gyroscope,

reducing the power consumption of the sensor significantly.

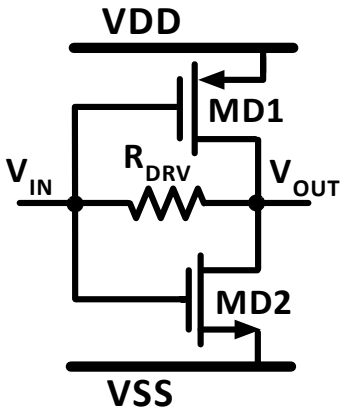

Figure 4-6 – Circuit diagram of output driver.

The complete drive chain was simulated using capacitive loads of C_P = 5pF at the input and output terminals. The system had a maximum simulated gain of 112.5 dBΩ (420 kΩ) with a 3-dB bandwidth of 32.31 MHz.

4.1.2. Automatic Level Control

An automatic level control (ALC) loop is integrated into the drive chain to eliminate any short-term amplitude variations in the drive mode of the gyroscope due to shock or other environmental and non-environmental factors, which would directly affect the Coriolis signal seen at the sense electrode due to the coupling of the two modes. The ALC regulates the drive signal by comparing the peak of the TIA output amplitude with pre-set reference voltage V_{AGC}. From this comparison, $V_{TUN\text{-}VGA}$ is adjusted to change the gain of the VGA such that a constant drive amplitude is maintained at the output of the driver circuit.

The ALC circuit (Fig. 4-7) is made of 4 blocks. The first block is a peak detector, which is used to measure and track the peak amplitude of the output signal of the drive TIA over time. The peak detector is composed of an op-amp connected as a unity-gain

follower with large capacitive (C_{PD}) and resistive (M_{T5}) loads to maintain the DC voltage of the output peak while rejecting the high frequency AC carrier signal. The peak detector DC output is passed through a buffer amplifier to a comparator, which compares it to a predetermined reference voltage (V_{AGC}) that is applied from an external source. Lastly, the signal is passed to a low-pass filter, which acts as an integrator and ramps the voltage between V_{DD} and V_{SS} until $V_{Tun\text{-}VGA}$ reaches a steady state and the comparator output is constant.

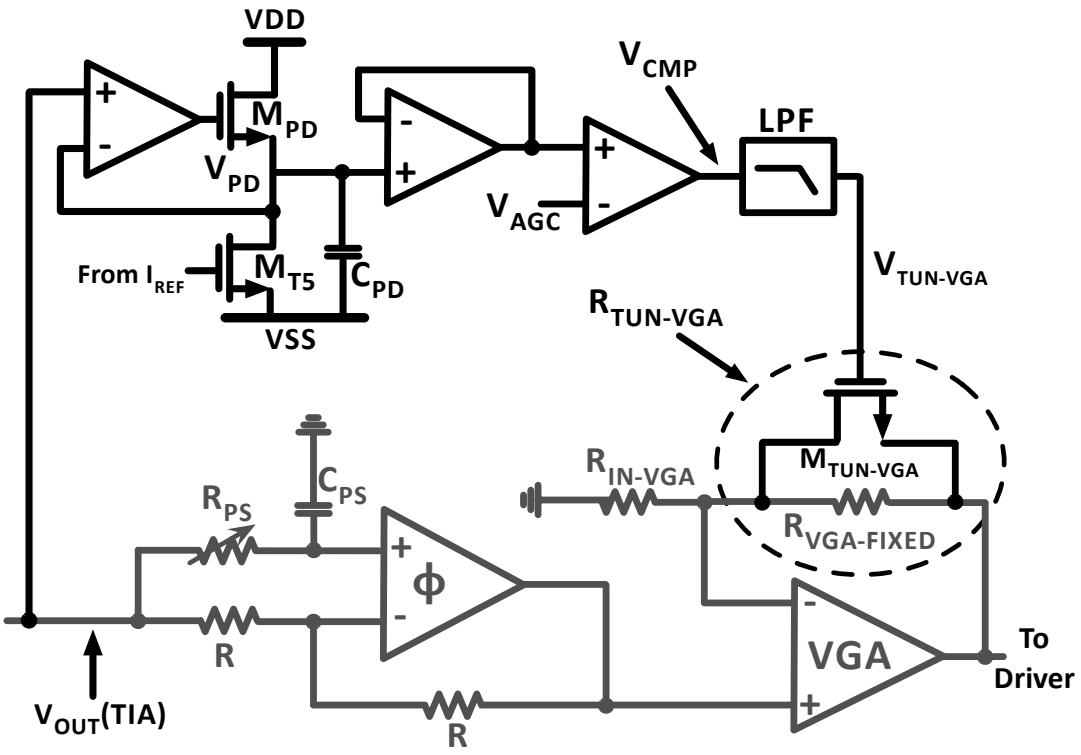

Figure 4-7 – Automatic level control architecture.

The comparator in the ALC loop is primarily responsible for controlling the gain of the VGA. If a larger signal is needed for the drive loop, the comparator will output $V_{CMP} = V_{DD}$, causing $V_{Tun\text{-}VGA}$ to slowly ramp higher until V_{PD} becomes larger than V_{AGC}. As V_{PD} approaches this point, V_{CMP} will slowly reduce until $V_{PD} = V_{AGC}$, at which point both

V_{CMP} and $V_{Tun\text{-}VGA}$ reach steady state and remain constant. Conversely, if a signal with smaller amplitude is needed, the comparator will output $V_{CMP} = V_{SS}$, causing $V_{Tun\text{-}VGA}$ to slowly ramp lower until V_{PD} approaches V_{AGC}.

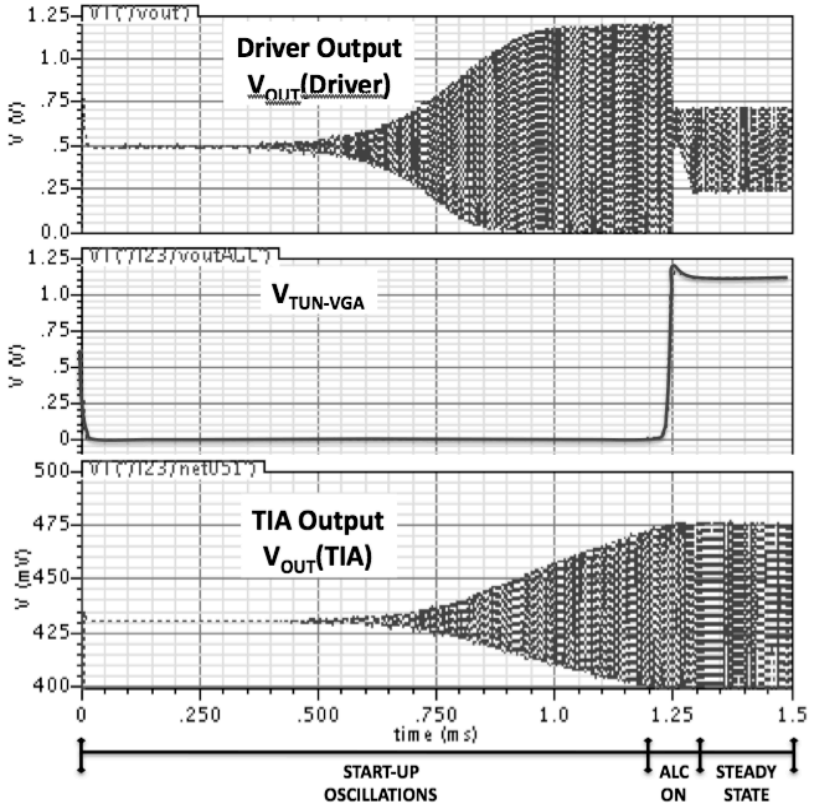

Figure 4-8 – Transient analysis of drive loop with before and after level control is activated.

To ensure that the ALC loop is stable and would not overshoot the steady state point and cause the drive signal to oscillate with $V_{Tun\text{-}VGA}$, transient simulations were run in Cadence for the complete drive loop. It is seen in Fig. 4-8 that after ALC loop turns on there is only a slight overshoot in $V_{Tun\text{-}VGA}$ before it reaches steady-state and the output of the drive loop and to the ALC loop ($V_{OUT}(TIA)$) operate with constant amplitudes. This data is validated using periodic steady-state stability (PSTB) simulations of the ALC loop, which showed a loop phase margin of 73.9° (Fig. 4-9). The PSTB simulations also reported a loop gain of 30.3 dB, indicating that the ALC has a maximum amplitude

variation of $\frac{1}{10^{\frac{A_{Loop}(dB)}{20}}} \cdot 100\% = 3.05\%$. The system settles into steady-state oscillation after ~1.5 ms, which is set by the bandwidth of the gyroscope as defined by (1-2).

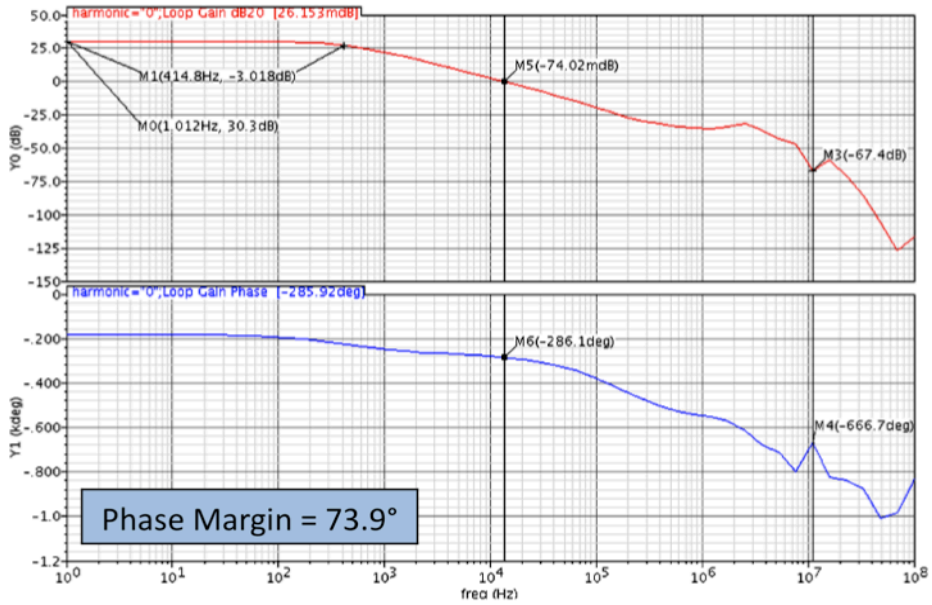

Figure 4-9 – Periodic stability (PSTB) analysis of ALC loop.

4.1.3. Sense Channel

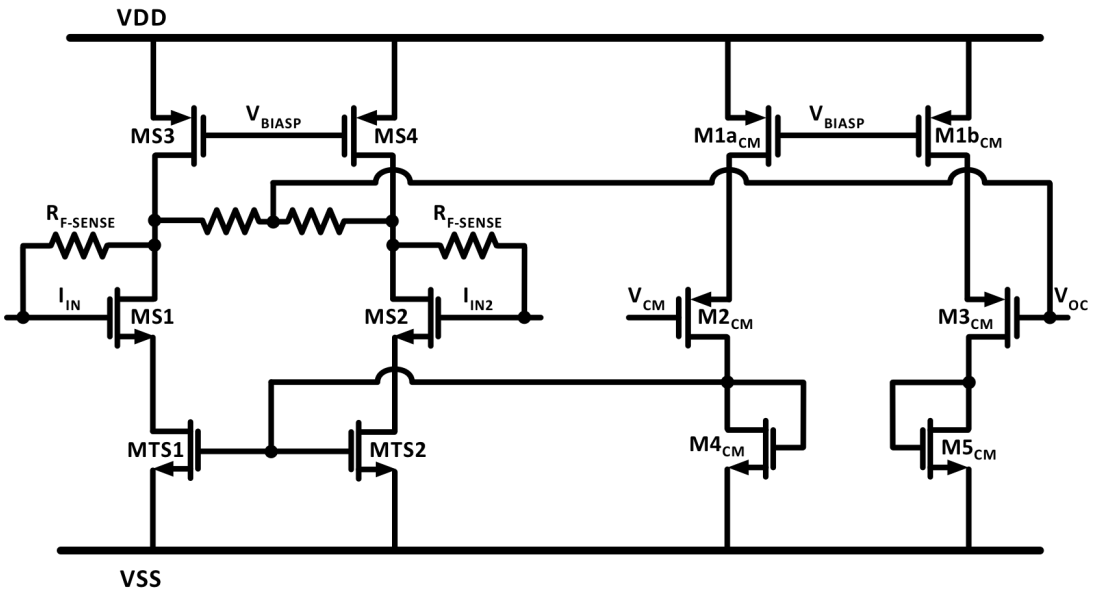

Figure 4-10 – Differential sense TIA with CMFB.

A fully-differential sense channel (Fig. 4-1) was implemented to eliminate common-mode noise along the channel and provide additional signal amplification by using both the positive and negative sense electrodes of the BAW gyroscope. The front-end of the sense channel is composed of a fully-differential TIA with common-mode feedback (Fig. 4-10), similar to the design described in Chapter 3. Large NMOS transistors are used for the input pair MS1-MS2 to reduce the flicker noise component of the amplifier while maintaining a large transconductance. A feedback resistance of $R_{F\text{-}SENSE}$ = 47 kΩ was implemented using a poly-silicon resistor. This resistance was chosen to provide high gain and maintain linearity across a large input range while accounting for any DC offset present due to quadrature (compensated or uncompensated). Using this architecture, an input referred current noise of 1.77 pA/√Hz was simulated at resonance (Fig. 4-11).

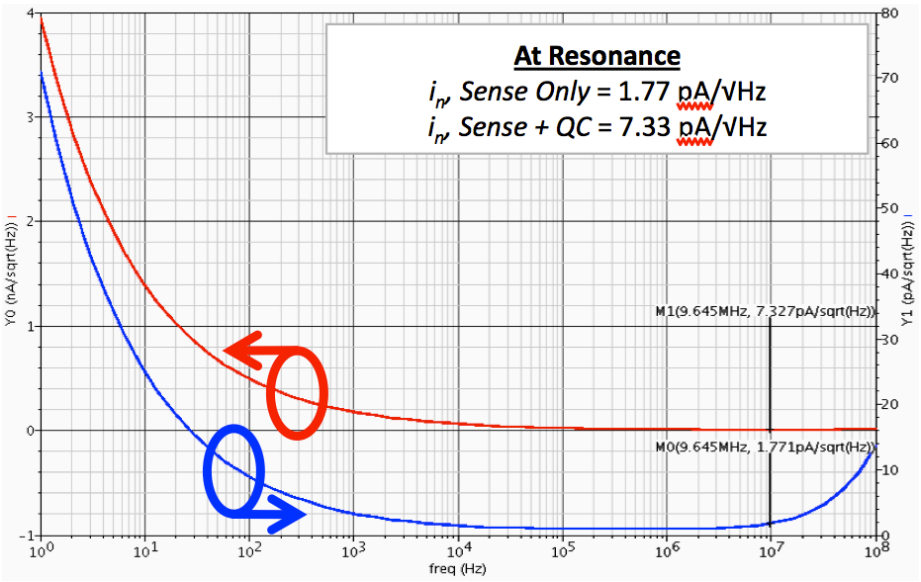

Figure 4-11 – Simulated input referred noise of sense TIA. Before the quadrature cancellation architecture is implemented, the input referred noise of the sense channel is measured to be 1.77 pA/√Hz (red). However, due to the gain attenuation brought upon by the resistive divider in the quadrature cancellation (QC) architecture, the input referred noise of the sense channel increases ~4X to 7.33 pA/√Hz (blue).

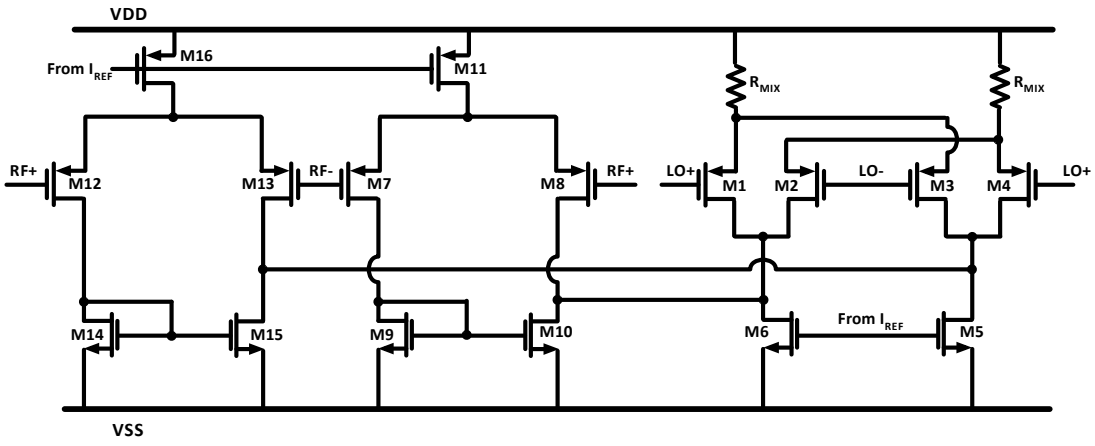

Figure 4-12 – Schematic of PMOS folded mixer.

After amplification, the signals are passed as RF inputs to a PMOS folded mixer (Fig. 4-12) [69], down-converted and decoupled from the carrier signal, and filtered by a 120 kHz on-chip passive RC low-pass filter. The LO signal of the mixer is provided by a clock generator which converts $V_{OUT}(TIA)$ of the drive loop into 2 non-overlapping, rail-to-rail clock signals with an output power of 3.5dBm. Using periodic AC (PAC) analysis, the conversion gain of the mixer was simulated to be A_{CG}=13.6dB at resonance. After low-pass filtering, the 2 signals are passed to an instrumentation amplifier, which amplifies the baseband Coriolis signal. The gain of the instrumentation amplifier is defined by

$$\frac{V_{OUT}}{V_2 - V_1} = \left(1 + \frac{2R_{INST2}}{R_{INST1}}\right)\frac{R_{INST4}}{R_{INST3}} \qquad (4\text{-}2)$$

in which V_1 and V_2 represent the inputs to the positive and negative terminals of the instrumentation amplifier, respectively. By setting R_{INST1}-R_{INST4} (Fig. 4-1) to 1kΩ, 40kΩ, 8 kΩ, and 12 kΩ, respectively, the gain of the instrumentation amplifier is calculated to

be A_{INST} = 41.7 dB. This is confirmed through AC simulation.

4.1.4. Quadrature Cancellation

It was discussed in Chapter 2.2.2 that imperfections in the gyroscope introduce a quadrature current at the sense input that is given by

$$i_{Sense} = i_{Coriolis} + i_{ZRO} \tag{4-3}$$

where $i_{Coriolis}$ and i_{ZRO} represent the Coriolis and quadrature current components of the sense output, respectively. However, because the quadrature current is in phase with the motional current of the drive mode, the input drive signal can be modified and fed to the sense input to suppress (or eliminate) i_{ZRO}.

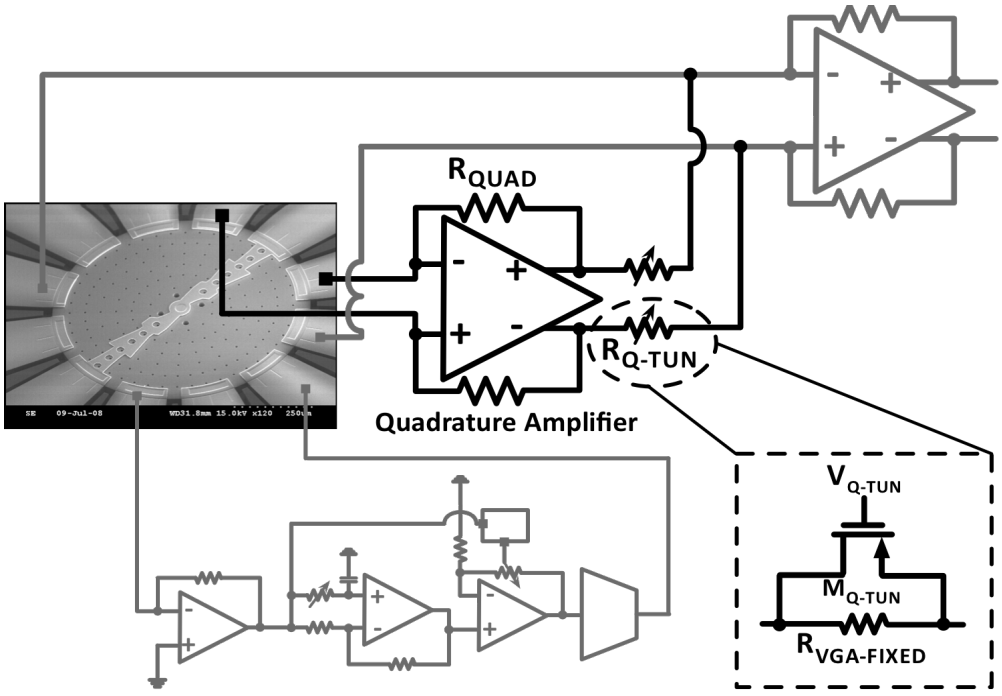

Figure 4-13 – Diagram of quadrature cancellation architecture.

A diagram of the quadrature cancellation (QC) architecture is shown in Fig. 4-13. The two inputs of the quadrature amplifier are connected to two 180° out-of-phase drive electrodes. Because of the symmetric disk structure, the two drive electrodes used for

quadrature cancellation are not directly connected to those used to excite the gyroscope into oscillation, circumventing any challenges that may occur from cross-coupling the two systems. The quadrature amplifier circuit is kept identical to the input differential sense TIA to eliminate any DC variation between the sense and QC signals; however, the feedback gain of the quadrature amplifier has been significantly reduced in order to minimize the undesired phase shift introduced by the amplifier.

After amplification, the quadrature amplifier signal is passed to the sense channel input TIA through a controllable resistive divider, creating a cancellation current that is fed to the sense TIA input and given by

$$i_{QC} = \frac{i_{Drive} R_{Quad}}{R_{Q-Tun}} \tag{4-4}$$

where R_{Quad} and $R_{Q\text{-}Tun}$ represent the trans-impedance gain of the quadrature amplifier and the equivalent resistance of the tunable divider, respectively. A tunable resistive divider was chosen because of the large tunable range offered through the use of MOS resistors, along with the small area needed to implement these components. Due to the inherent coupling of the drive and quadrature signals, the phase difference between these two components will be 0° or 180°, depending on the phase of i_{Drive}. Assuming i_{QC} and i_{ZRO} are 180° out of phase (which can be done easily by wirebonding to the correct electrode), the input current of the sense TIA will become

$$i_{Sense} = i_{Coriolis} + i_{ZRO} + i_{QC} \tag{4-5}$$

Substituting (4-4) into (4-5), i_{Sense} simplifies to

$$i_{Sense} = i_{Coriolis} + \left(i_{ZRO} - \frac{i_{Drive} R_{Quad}}{R_{Q-Tun}} \right) \tag{4-6}$$

If $R_{Q\text{-}Tun}$ is tuned such that i_{QC} matches the magnitude of i_{ZRO}, the quadrature component of the output signal will be eliminated, leaving the sense current solely dependent upon $i_{Coriolis}$.

Although the quadrature compensation architecture was shown in both simulation and measurement to significantly attenuate the magnitude of the quadrature component of the sense signal, it was observed following measurement of the rate signal that it also degrades the input referred noise component of the sense channel. As shown in Fig. 4-11, the introduction of the quadrature cancellation architecture increases the input referred noise of the sense channel by 4.2X to 7.3 pA/√Hz. This increase in the noise is attributed to noise introduced by the quadrature amplifier by $R_{Q\text{-}Tun}$, as well as gain attenuation of the input sense TIA due to resistive loading from the QC architecture. To minimize this noise component, a tunable capacitive divider can replace R_{Quad} and $R_{Q\text{-}Tun}$ as the tuning elements, and a low noise current buffer should be introduced between the sense TIA and the QC architecture to reduce loading effects.

4.1.5. Power Analysis

From simulation, the power consumption of the complete ASIC was found to be 1.51 mW. Table 4-1 shows a power breakdown of each major block of the interface ASIC. Although the drive loop and sense channel consume a relatively equal amount of power, it should be noted that the sense channel is implemented differentially and therefore has two channel paths that double the power of the TIA and quadrature cancellation blocks. This can be reduced by converting these structures to single-ended designs; however, a fully-differential design is recommended for retention due to its gain and noise rejection benefits. Therefore, the focus of power reduction is placed on the drive loop, specifically

on the input TIA and output driver blocks. The power consumption of these blocks is large primarily due to the input or output parasitic capacitive loads introduced from the gyroscope. As these parasitics are reduced, the power consumption of the TIA and output driver can also be proportionally decreased. Therefore, additional focus should be placed on reducing packaging and fabrication parasitics, as well as developing electronic compensation techniques for reducing the capacitive loading effects introduced by the gyroscope.

Table 4-1 – Overview of power consumption of ASIC blocks

Block	Power Consumption	Percentage of Total Power Consumption
Drive Loop	740.9 µW	49.0%
TIA	*236.2 µW*	*15.6%*
Phase Shifter	*115.8 µW*	*7.7%*
VGA	*70.0 µW*	*4.6%*
Output Driver	*266.1 µW*	*17.6%*
AGC	*52.8 µW*	*3.5%*
Sense Channel	724.7 µW	48.0%
TIA	*256.2 µW*	*17.0%*
Quad Cancellation	*237.1 µW*	*15.7%*
Mixer	*114.7 µW*	*7.6%*
Rate Amp	*116.7 µW*	*7.7%*
Biasing	45.1 µW	3.0%
Total	**1510.7 µW**	**100 %**

4.2. Results and Discussion

4.2.1. Drive Loop

The gyroscope ASIC was fabricated in a 0.18µm standard TSMC process. Following tape-out, both the IC and the device were affixed to a custom PCB (Fig. 4-14) and interfaced using aluminum bondwire. All measurements were recorded using an Agilent 4395A Network/Spectrum analyzer and Tektronix 54622D and DSO6014A oscilloscopes.

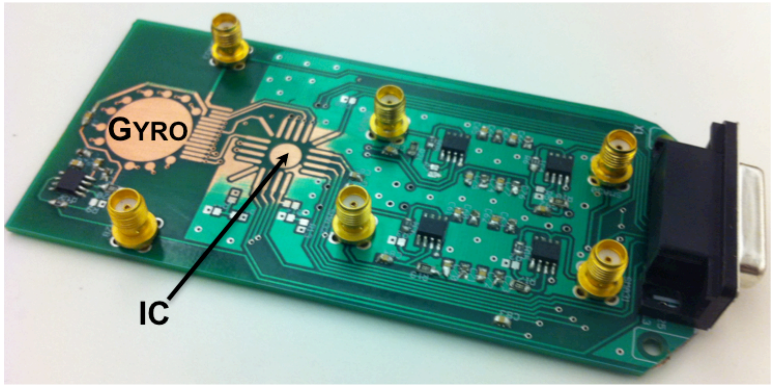

Figure 4-14 – BAW gyroscope interface PCB.

Figure 4-15 shows the transfer function of the BAW gyroscope interface. After being placed on the PCB, the drive loop of the ASIC was connected in feedback with the drive mode of the device. The resulting oscillations (Fig. 4-14, inset) showed a maximum AC drive voltage of 660 mV_{pp} at resonance using a supply voltage of $1.2V$. Although higher output voltages were attainable for the device, they exceeded the acceptable upper limits for V_P ($>35V$) and were not used during testing to avoid damaging the gyroscope.

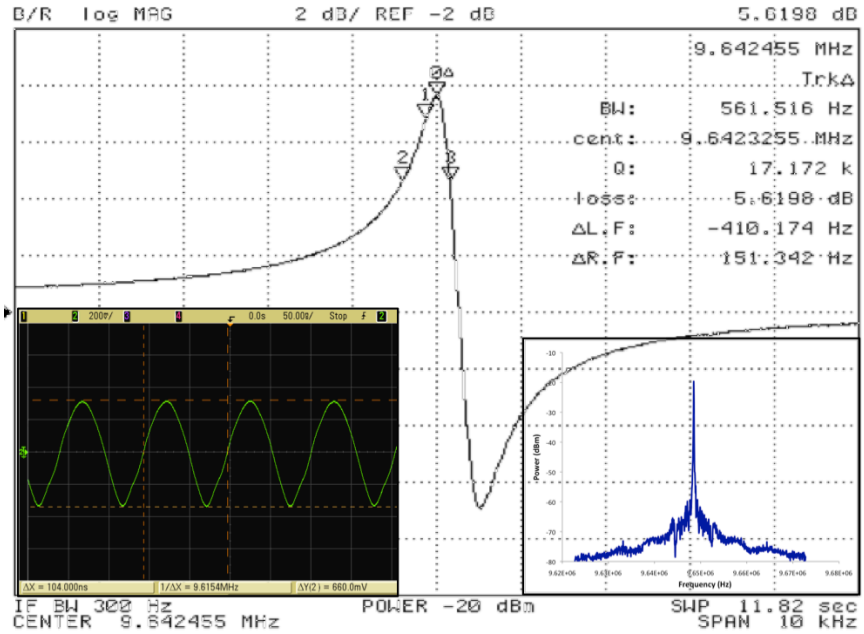

Figure 4-15 – Transfer function of BAW device. (inset, left) Closed-loop oscillation waveform. (inset, right) Closed-loop frequency spectrum at resonance.

To characterize the timing performance of the drive loop, temperature sensitivity (Fig. 4-16) and phase noise measurements (Fig. 4-17) were performed on the drive oscillations. The drive signal was shown to have a temperature coefficient of frequency (TCF) of -26.7 ppm/°C with a phase noise of -118 dBc at 1MHz from the carrier signal and -103 dBc at 1kHz from carrier.

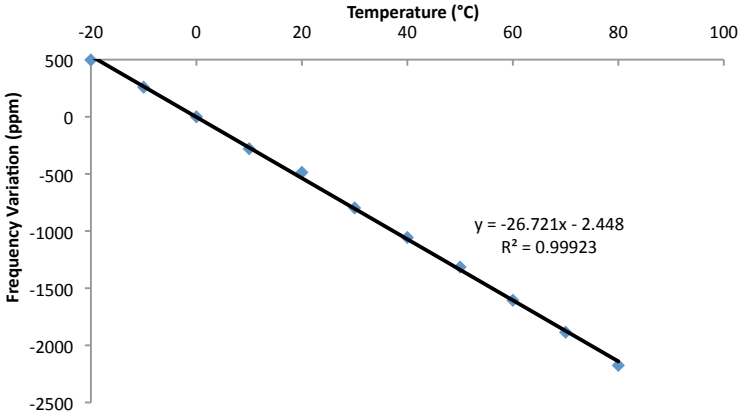

Figure 4-16 – Measured TCF of BAW disk gyroscope drive loop (-20°C to 80°C).

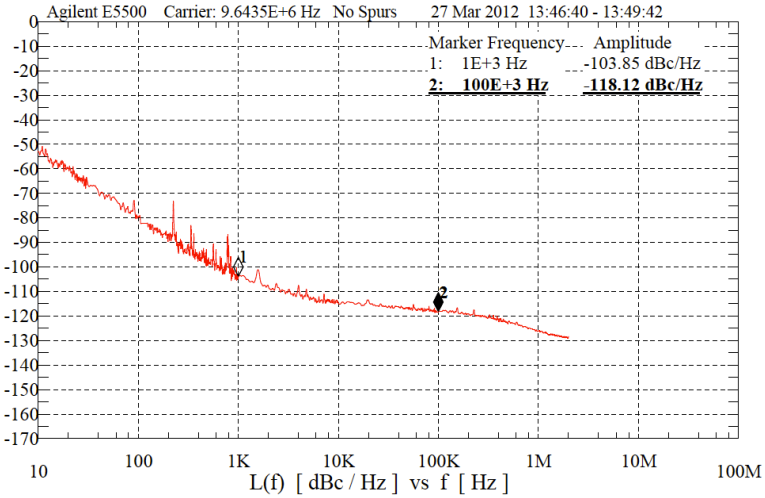

Figure 4-17 – Measured phase noise of BAW gyroscope drive loop oscillations.

After collecting TCF and phase noise data, the BAW disk gyroscope oscillator performance was compared to other state-of-the-art MEMS oscillators in literature to determine whether or not it could be used as a viable clocking source,. As shown in

Table 4-2, the BAW oscillator consumes less power than most designs while offering very competitive phase noise performance close-to-carrier. This data was then used to calculate an oscillator figure of merit (FOM) [70], in which the phase noise, power consumption, and operating frequency are equally weighted to provide a snapshot of the overall performance of any oscillator. The FOM is given by

$$FOM = 20 \cdot \log(\frac{f_0}{f_m}) - 10 \cdot \log(P_{DC}) - L(f_m) \quad (4\text{-}7)$$

Based on this equation, the BAW oscillator is shown to have a FOM of 185dB, comparable to the other oscillators in the state of the art. This suggests that with additional work to minimize temperature and environmental variations, the BAW gyroscope drive loop can make an effective timing device and rate sensor hybrid.

Table 4-2 – MEMS oscillator performance comparison

Design	Process (μm)	f_0 (MHz)	P_{DC} (mW)	Phase Noise @ 1kHz (dBc)	FOM @ 1kHz (dB)
[71]	0.18	496	9.4	-92	196
[72]	0.18	8.29	8.7	-89	158
[73]	0.5	1050	3.5	-81	196
[74]	-	42.8	6	-105	170
[75]	0.6	6	1.8	-112	185
[76]	0.35	10.92	0.35	-85	170
[77]	0.35	61.2	0.95	-100	196
This Work	**0.18**	**9.7**	**0.78**	**-104**	**185**

Following phase noise and temperature measurement, experiments were performed to determine the sensitivity of the drive loop frequency to rotation rate. ANSYS (Fig. 4-18) simulations run on the drive mode sensitivity of the BAW disk gyroscope show negligible change in the phase shift and frequency of the drive signal to applied rate up to 3000 °/s. These simulation results were reproduced in Cadence (Fig. 4-19), where it was also shown that a low frequency gyroscope such as the tuning fork (f_0~*10 kHz*) would begin show significant variation to applied rotation inputs of 100 °/s or greater. Cadence

simulations of the closed-loop drive oscillations (Fig. 4-20, left) further supported the BAW gyroscope immunity to applied rotation, showing negligible sensitivity until rotation frequencies >1000 Hz were applied. However, the drive frequency of the oscillator showed a total measured variation of ~18 ppm (Fig. 4-20, right) when the sensor was rotated at rates from 0-160 °/s . It was concluded that this drastic increase in rotation sensitivity is created by limitations in the testing setup which create board and package stresses that affect the device and ASIC, as discussed in [68, 78]. This requires careful re-implementation of each experiment to match the experimental results to simulation.

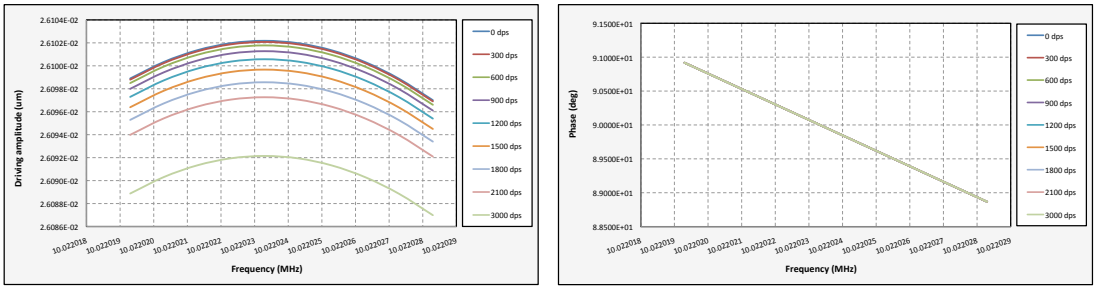

Figure 4-18 – ANSYS simulation of drive-mode (right) amplitude and (left) phase shift variation of BAW gyroscope due to applied rotation rate. Even after 3000 °/s rotation is applied, there is negligible change in these two signals at resonance, indicating strong immunity of the drive loop frequency to applied rotation inputs.

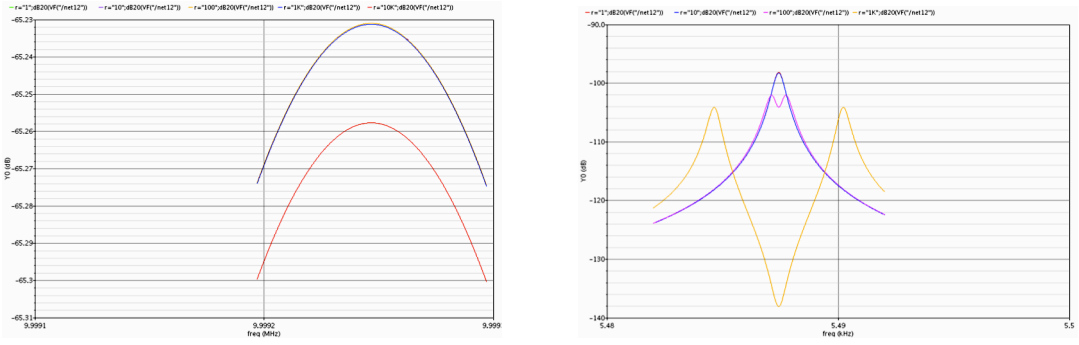

Figure 4-19 – (left) Cadence simulation of (left) BAW disk and (right) tuning-fork drive-mode variation due to applied rotation rate. Negligible change in the BAW signal was observed after applying rotation rates up to 10000 °/s, supporting the observations made from the ANSYS simulations. However, the tuning-fork shows significant peak splitting and shift after only 100 °/s rotation is applied, suggesting that the high frequency BAW disk gyroscope has a higher immunity to rotation rate-induced frequency variations of the drive loop.

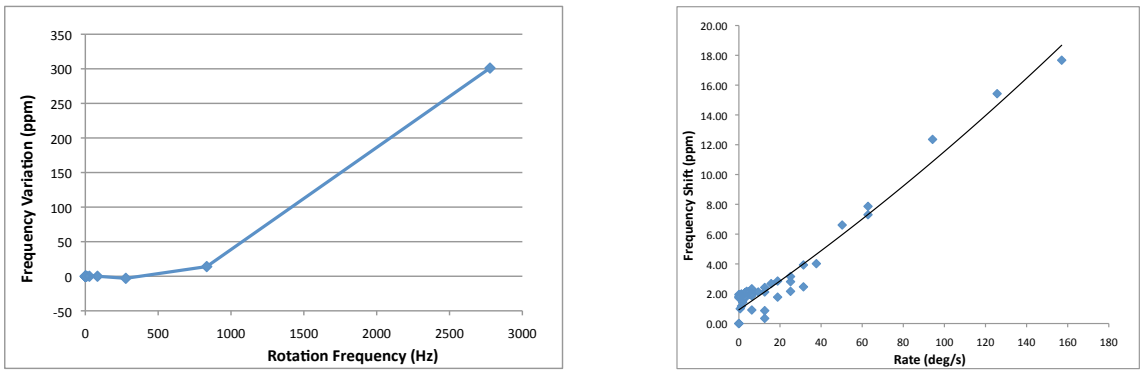

Figure 4-20 – (left) Simulated closed-loop BAW gyroscope drive oscillation frequency dependence on applied rotation rate. Significant frequency variation was not observed until rate signals >1000Hz (300000 °/s) were applied to the device. (right) Measured BAW gyroscope drive loop frequency dependence on applied rotation rate. In contrast to simulation, the drive loop shows significant rate sensitivity (18 ppm over 160 °/s), indicating external factors may be responsible for the variation of the drive signal.

4.2.2. Automatic Level Control

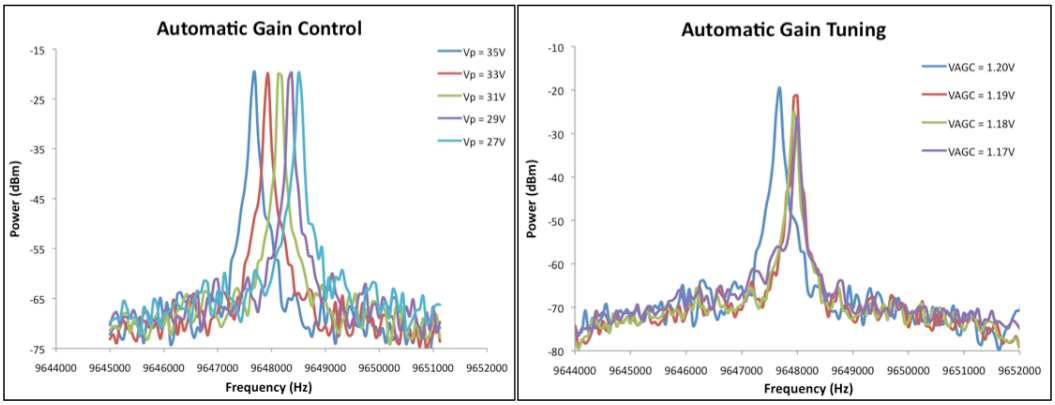

Figure 4-21 – (left) Amplitude variation of ASIC. (right) Tunable amplitude range of ASIC.

To characterize the ALC, two tests were performed. First, the amplitude variation of the output peak was measured as V_P was tuned between 27-35V. Based on (2-6), tuning V_P across this range would cause a 40% change in R_m (and consequently, V_{OUT}) if the system were left uncompensated. With the ALC on (Fig. 4-21), the total variation in the output signal is measured at 0.362 dBm (4.18%), similar to the amplitude variation simulated for the loop in chapter 4.1.2. Following this measurement, the tuning voltage V_{AGC} was adjusted to test whether or not the output voltage of the drive loop would tune

with this voltage. The measurements in Fig. 4-21 showed the ALC tuning range to be 6.42 dBm across a tuning range of 30 mV. At $V_{AGC} < 1.17V$, there was not enough gain in the drive chain to supplement the gyroscope loss, and the system was seen to drop out of self-oscillation. This indicates a need for very precise tuning circuitry for V_{AGC} to set the desired amplitude levels.

4.2.3. Sense Channel

To measure the input referred current noise of the sense channel, the voltage noise at the output of the TIA was recorded on the 4395A network analyzer and divided by $R_{F\text{-}Sense}$ (Fig. 4-22). Using this method, input referred noise measurements of 1.74 pA/√Hz (without the quadrature cancellation circuitry) and 9.36 pA/√Hz (with QC circuitry) were measured at resonance, close to estimated current noise found through simulation.

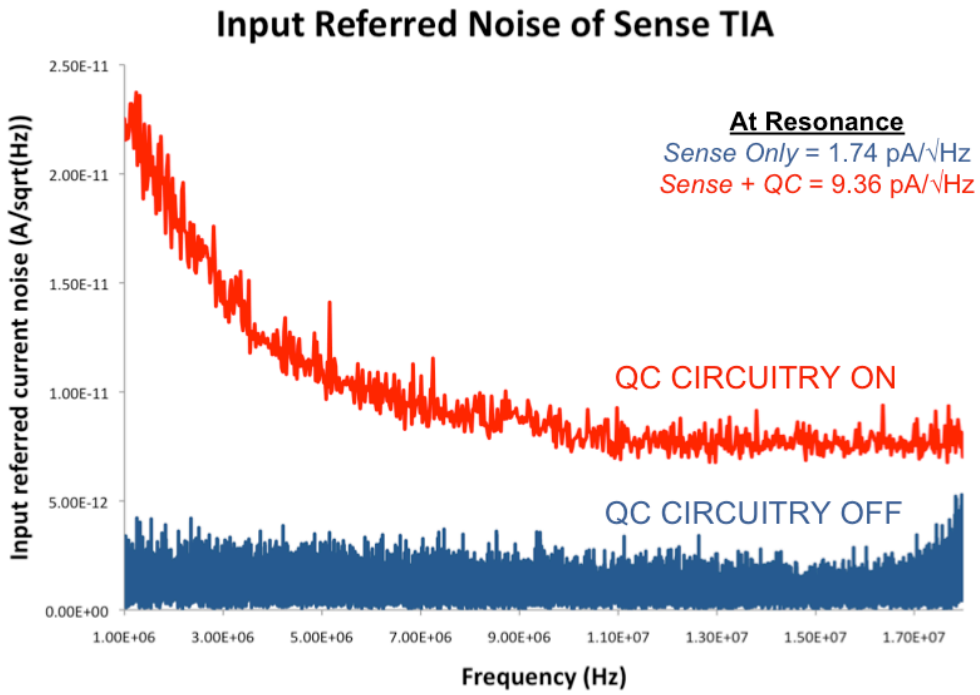

Figure 4-22 – Measured input referred sense current noise. When the quadrature cancellation circuitry was enabled, the input referred noise of the channel jumped 5.4X (from 1.74 to 9.36 pA/√Hz).

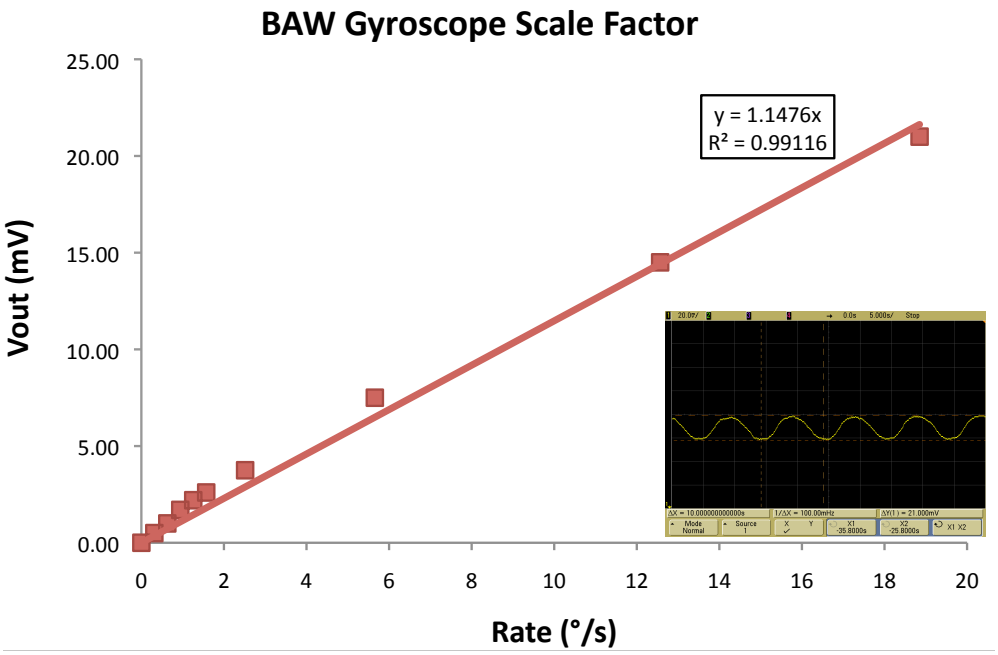

Figure 4-23 – BAW gyroscope scale factor, showing the sensor has a sensitivity of 1.15 mV/°/s. (inset) Sensor response to 20 °/s sinusoidal rate input.

Following noise measurement, the sensor was placed on an Ideal Aerosmith rate table for sensitivity characterization. Before applying any rotation input, a 5-Hz off-chip low-pass filter was added at the rate output terminal of the IC in order to filter high frequency noise from the AC power supplies. Sinusoidal rates were then applied, yielding a scale factor of 1.15 mV/°/s (Fig. 4-23) for the sensor. Using this sensitivity, Allan variance measurements taken for the sensor (Fig. 4-24) showed the gyroscope to have a bias instability of 0.095 °/s, satisfying the requirement for rate grade performance (Table 1-2). It should be noted that the current version of the BAW gyroscope is not sensitive enough to measure Earth's rotation rate (~0.004 °/s), and therefore earth rotation does not impact the accuracy of this measurement.

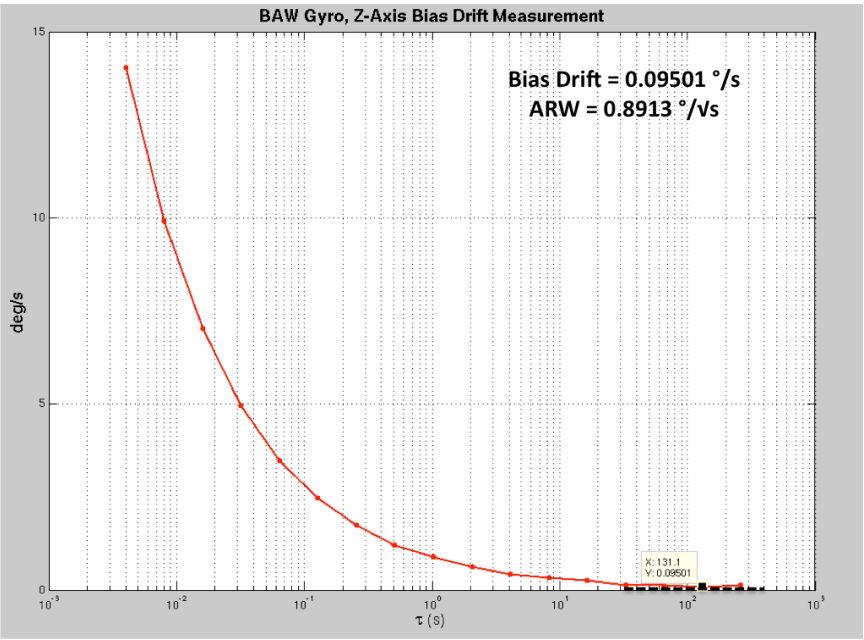

Figure 4-24 – Allan variance measurement of BAW gyroscope, showing the gyroscope has a bias drift of < 0.1 °/s and an angle random walk of 0.8913 °/√s.

4.2.4. Quadrature Cancellation

As mentioned in the previous chapter, quadrature cancellation is an undesired coupling between the drive and sense modes of the gyroscope. To fully observe the effects of the quadrature cancellation architecture, the closed loop connection of the ASIC was broken and an input signal was applied to the drive mode of the gyroscope from the network analyzer and measured after the sense TIA. Before applying any compensation, a distinct quadrature-induced peak was measured on the network analyzer as a consequence of the coupling between the two modes. As $V_{Q\text{-}TUN}$ of the compensation resistor increases, the magnitude of the peak is reduced (Fig. 4-25), although the maximum tuning voltage of the compensation circuit was unable to completely remove the quadrature signal. Additionally, it can be seen that the noise floor of the sensor increases, presumably due to the noise degradation factors outlined in Section 4.1.4.

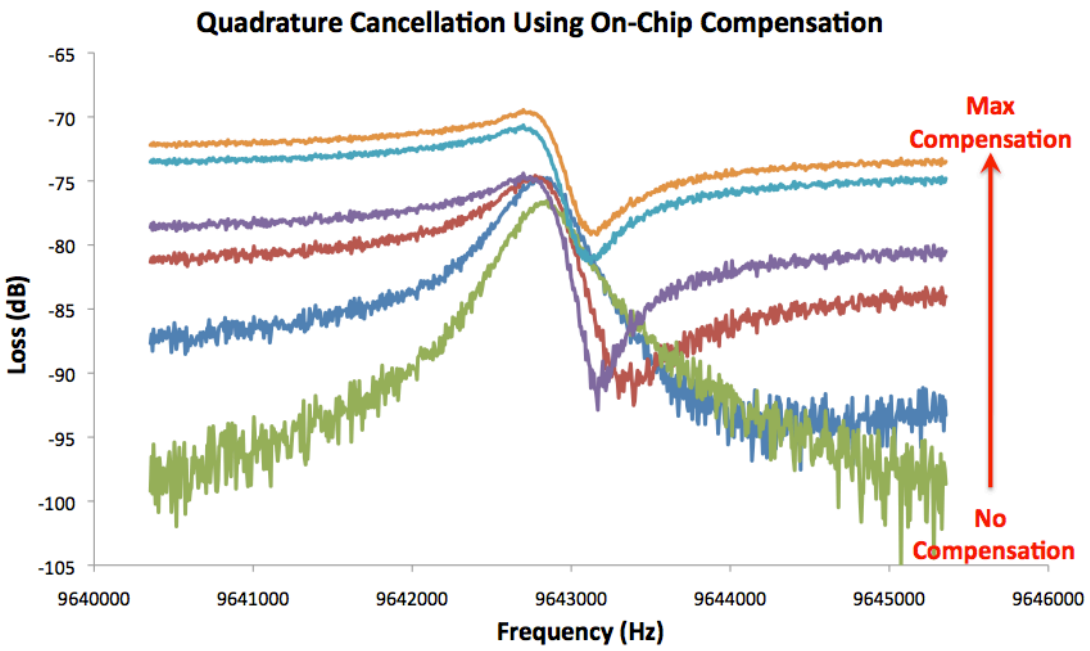

Figure 4-25 – Reduction in quadrature using on-chip compensation.

After measuring the open-loop effects of the quadrature compensation architecture, the ASIC was reconnected in closed-loop feedback with the gyroscope. Transient measurements of the rate output terminal (Fig. 4-26) showed that the magnitude of the output signal increases 4X (2.5 mV_{PP} to 10 mV_{PP}) when $V_{Q\text{-}TUN}$ is increased to the maximum compensation point. This is believed to occur due to attenuation of the quadrature input to the sense TIA by the cancellation circuitry, which returns the TIA to small-signal operation where the gain of the amplifier is significantly larger and more linear. Further improvements to the quadrature compensation architecture (specifically modifying the $R_{Q\text{-}TUN}$ element) can be made to electrically remove all coupling present between the drive and sense modes of the gyroscope and reduce the noise injected by the quadrature cancellation circuitry into the sense channel.

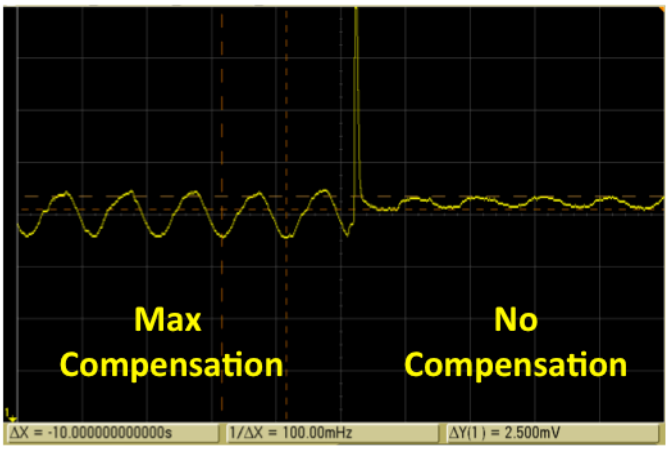

Figure 4-26 – Gyroscope transient response for 12.5°/s applied rotation rate before and after quadrature compensation. When no compensation is applied, a signal of 2.5 mV_{PP} is measured at the sensor output. With maximum compensation, this signal improves to 10.0 mV_{PP}.

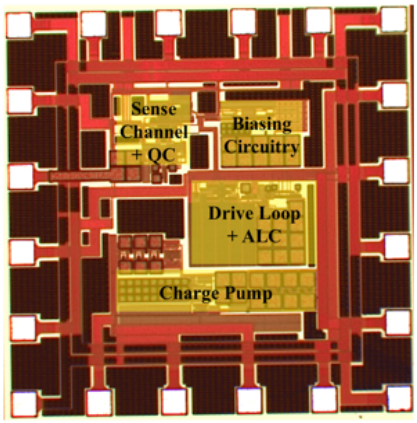

Figure 4-27 – TSMC die micrograph.

4.3. Performance Analysis

Table 4-3 presents a breakdown of key parameters of the interfaced BAW disk gyroscope. By driving the gyroscope with a large vibration amplitude and incorporating quadrature cancellation to reduce the magnitude of the ZRO component, the sensor offers a sensitivity of 1.15 mV/°/s with a bias instability of 0.095 °/s. This performance should improve if the noise contribution of the quadrature cancellation architecture is reduced. The power consumption of the system (excluding the charge pump) was measured to be 1.59 mW, close to the expected simulation results. The ASIC area (Fig. 4-27) measures

0.8 mm x 0.8 mm.

Table 4-3 – Summary of measured sensor parameters

Parameter	Measured Performance
Fabrication Process	TSMC 0.18 µm
IC Die Area	0.64 mm^2
Supply Voltage	1.2 V
Total Power Consumption	1.587 mW
Polarization Voltage	35 V
Sense Channel Input Referred Noise	9.36 pA/√Hz
Measured Sensitivity	1.15 mV/°/s
Electronic Noise Floor	0.0202 °/s/√Hz
Bias Stability	0.095 °/s
Angle Random Walk	0.8913 °/√s

The table suggests that the BAW gyroscope is can be used as both a timing element and a rotation sensor, although work can still be done to improve the sensor's performance in both areas. Compensation circuitry must be added to the drive loop in order to reduce the variation of the drive signal TCF. Additionally, a more optimal testing setup is needed to characterize the gyroscope to prevent the strain-induced frequency effects discussed in Chapter 4.2. To reduce the ASIC ENEΩ and further improve rotation sensitivity, a buffer must be added between the quadrature cancellation circuitry and the sense input TIA. This will remove any loading effects from the cancellation circuitry on the TI and prevent attenuation of the TIA gain and its corresponding increase in input referred current noise. Following this, R_F and g_m must be calculated for optimum noise performance based on the criteria discussed in Chapter 3.

CHAPTER 5

CHARGE PUMPS: ON-CHIP DC VOLTAGE GENERATION

Current trends of development in resonant capacitive MEMS inertial sensors [27, 35, 51] have focused on the design and fabrication of devices that have grown smaller and more sophisticated over the last several years. The accompanying interface circuitry is simultaneously pushed toward smaller minimum feature sizes as the reduced area, enhanced unity-gain bandwidth, and decreased power consumption offered by circuits in newer CMOS processes are more attractive for use in consumer-, industrial-, and military-based applications. However, the actuation of these smaller MEMS devices requires the use of large DC polarization voltages, a problem exacerbated by the voltage headroom limitations of these same state-of-the-art CMOS processes.

Charge pumps are DC voltage generators commonly used for non-volatile and programmable memories (i.e. flash, EEPROM) to generate the high voltages necessary to operate such systems. Unlike other high voltage generators (i.e. transformers and diode-voltage multipliers [79]), charge pumps can be fabricated directly on a CMOS IC, making them critical system components due to the significant area and cost savings of on-chip integration. For this reason, charge pump use has become more common in MEMS systems, providing the large on-chip DC polarization voltages (V_P) necessary to actuate many resonant devices (i.e. gyroscopes) [31, 35, 80]. In recent years, as the

supply voltage of standard CMOS processes have trended downward (Fig. 5-1) [81], additional stages have been added to the charge pump chain to compensate for the reduction in output voltage. However, the body effect of MOS transistors prevents these additional stages from transferring as much charge as the previous pump. Thus, novel techniques and strategies [82-89] must be employed that both improve the efficiency and increase the DC output of these architectures. To maximize the resolution of the sensor, these systems must also suppress any voltage ripple atop the DC voltage generated by the circuit or the charge pump.

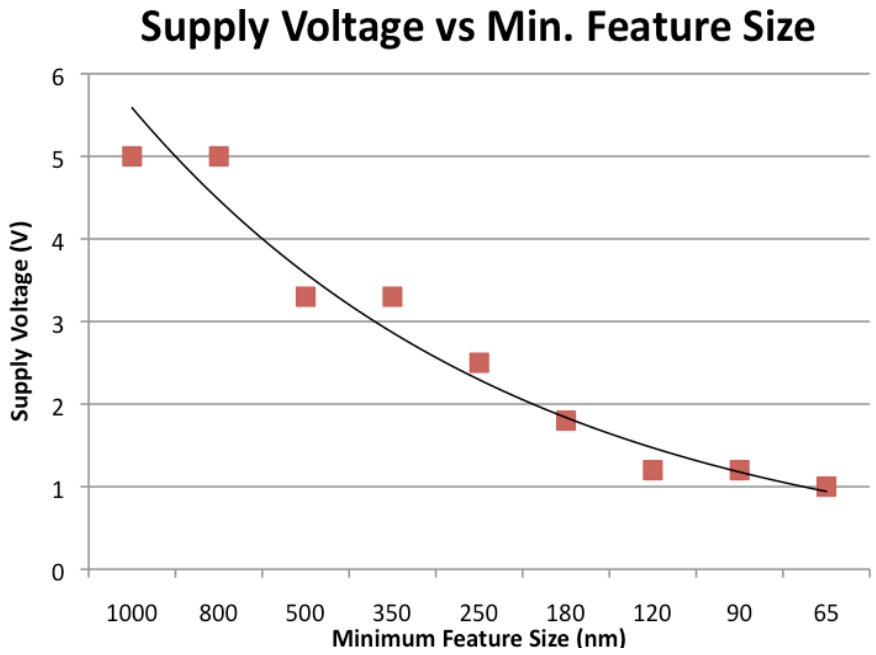

Figure 5-1 – Standard supply voltages used for given feature sizes.

This chapter investigates the requirements for designing and optimizing charge pumps for capacitive MEMS devices. Basic charge pump design is introduced, and architectures that provide better efficiency (i.e. improve the charge transfer between pump stages) and generate larger pump voltages are presented. Following this

discussion, closed-loop strategies for maintaining a constant voltage and reducing voltage ripple at the pump output are also reviewed.

5.1. CMOS Charge Pumps

A charge pump is a DC-DC voltage converter that uses a network of capacitors and diodes/switches to up-convert (down-convert) an input DC voltage to a higher (lower) voltage. As mentioned previously, charge pumps can be integrated monolithically, making them particularly useful for any IC that requires a DC potential above the maximum tolerance of its respective CMOS process. For MEMS gyroscopes, charge pumps generate large DC polarization voltages (V_P) necessary to realize the best performance from the device. From (2-6), a high V_P reduces the motional impedance of a capacitive resonator. Consequently, any oscillator made from this device will generate a larger carrier power, which translates to a lower phase noise signal. Additionally, it can be seen from (1-5) that the ENEΩ of a MEMS rate vibratory gyroscope will reduce as V_P is increased.

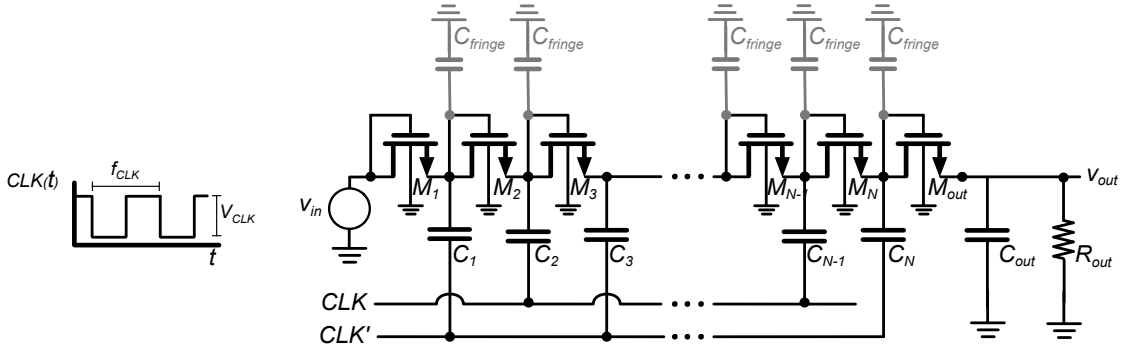

Figure 5-2 – Block diagram of Dickson charge pump. In a typical CMOS process, an NMOS transistor is used as the diode component.

A diagram of the traditional CMOS Dickson charge pump is shown in Fig. 5-2. In most designs, both v_{in} and V_{CLK} are set to the supply voltage (V_{DD}) to generate the largest

DC voltage possible. Unless a multi-well process is used, the bulk of each transistor is connected to the IC substrate and thereby set to the minimum voltage possible (typically V_{SS} or GND). NMOS diodes M_1-M_N are used to transfer the voltage held in capacitors C_1-C_N between stages. These capacitors are set to the same capacitance (C) and are alternately connected to one of two non-overlapping clock signals, *CLK* and *CLK'*. R_{out} and C_{out} represent the impedance at the output of the charge pump due to loading from the connected stage. If this stage is capacitive in nature (as is the case with capacitive MEMS devices), R_{out} can be neglected, and only C_{out} must be considered.

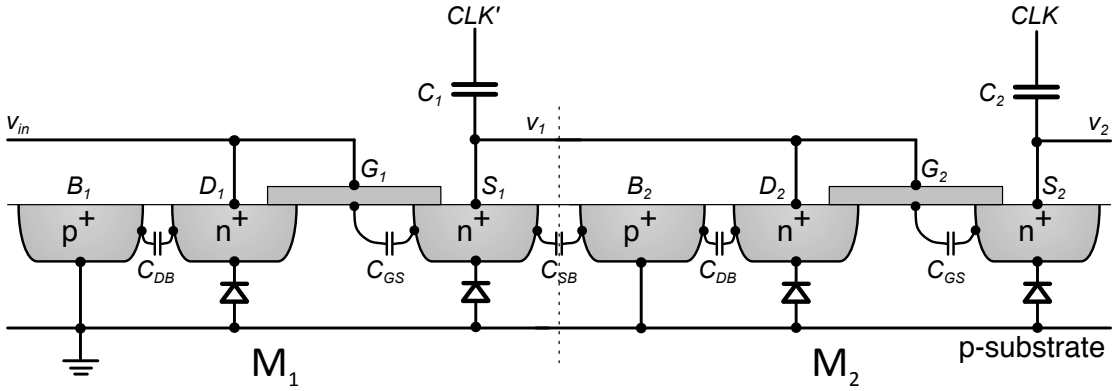

Figure 5-3 – Model of first two stages of CMOS Dickson charge pump based on MOS device physics.

To understand the operation of the CMOS charge pump, consider the device physical model in Fig. 5-3 that shows the first two stages of the pump. If *CLK* is set to V_{CLK} (*CLK'* to GND), then $v_{GS1}>V_t$ and transistor M_1 will turn on, reaching saturation due to the diode connection. Conversely, M_2 will remain off because $v_{GS2}<V_t$. Each parasitic diode connection to the charge pump is reverse-biased, preventing any latch-up issues that may occur across the chain. While M_1 is on, the input voltage v_{in} will be transferred across the diode, charging C_1 to $v_1=v_{in}-V_t$.

When *CLK* changes to GND M_1 turns off. However, because of the simultaneous change of *CLK'* to V_{CLK}, v_1 becomes

$$v_1 = v_{in} + \left(V_{CLK} \frac{C}{C_{f\,ringe} + C} - \frac{i_{out}}{f_{CLK}\left(C_{f\,ringe} + C\right)} - V_t \right) \tag{5-1}$$

where i_{out}, C_{fringe}, and f_{clk} represent the equivalent pump output current due to loading from the connected stage, total fringe capacitance present at the node (from C_{GS}, C_{SB}, etc), and clock frequency, respectively [83]. Furthermore, all parasitic diode connections along the diode chain remain reverse-biased, ensuring proper functionality as the voltage increases across the later stages of the pump. After N pump stages, the charge pump voltage (v_{out}) becomes

$$v_{out} = v_{in} + N \cdot \left(V_{CLK} \frac{C}{C_{f\,ringe} + C} - \frac{i_{out}}{f_{CLK}\left(C_{f\,ringe} + C\right)} - V_t \right) - V_t \tag{5-2}$$

in which V_t is given by

$$V_t = V_{t0} + \gamma \cdot \left(\sqrt{2\phi_s + V_{SB}} - \sqrt{2\phi_s} \right) \tag{5-3}$$

where ϕ, γ, and V_{SB} represent the surface potential at threshold, body effect coefficient, and potential across the source-bulk interface, respectively.

One of the major tradeoffs of charge pump integration is the inherent body effect associated with MOS transistors along the pump chain. As the DC voltage increases at each stage along the charge pump, the potential at the source of each transistor increases while the bulk remains tied to ground, increasing V_{SB}. From (5-3), V_t will rise and less charge will be transferred to the remaining stages until it becomes so large that there is no net transfer of charge between stages.

5.2. Charge Pump Regulation

When a rotation rate (Ω) is applied to the gyroscope, the induced Coriolis acceleration will be orthogonal to both the drive axis and the axis of rotation. Expanding upon (1-10), this acceleration can be written as

$$\vec{a}_{Coriolis} = 2\frac{\partial \vec{x}_{drive}(t)}{\partial t} \times \vec{\Omega} \tag{5-4}$$

which (from Appendix A) gives a Coriolis current of

$$\frac{I_{out}}{\vec{\Omega}_z} \approx \frac{2\varepsilon_0^2 A_{cap}^2 Q_{eff}^2 V_P^2}{M_{eff}\omega_0^2 g_0^4} v_{ac} \sin(\omega_0 t) \tag{5-5}$$

It can be concluded from (5-5) that the output Coriolis current is only dependent upon the rotation rate applied to the gyroscope. However, this is based upon the assumption that V_P remains constant over time, which is unlikely in an uncompensated system due to short- and long-term variations in the pump voltage. Consequently, the constant-V_P term is replaced with time variant term $V_P(t)$, changing (5-5) to

$$\frac{I_{out}}{\Omega} \approx \frac{2\varepsilon_0^2 A_{cap}^2 Q_{eff}^2}{M_{eff}\omega_0^4 g_0^4} v_{ac} V_P(t) \cdot \left(V_P(t)\omega_0^2 \sin(\omega_0 t) - 2\frac{\partial V_P(t)}{\partial t}\omega_0 \cos(\omega_0 t) - 2\frac{\partial V_P^2(t)}{\partial t^2}\sin(\omega_0 t) \right) \tag{5-6}$$

If left unregulated, the charge pump output voltage is susceptible to one of several perturbations. This includes shock and drift, along with environmental variations (i.e. temperature) that can cause non-negligible changes to the charge pump output voltage. The charge pump also introduces a ripple in the output voltage due the continuous capacitive charging and discharging of each pump stage. This ripple voltage is present in both open- and closed-loop pump designs, and is given by

$$V_{Ripple} \propto \frac{i_{out}}{f_{CLK}\left(C_{fringe} + C\right)} \tag{5-7}$$

In open-loop charge pump architectures, V_{Ripple} is minimized through the use of large pump capacitors and high frequency clock signals (5-7). However, in order to keep the charge pump operating at a fixed DC voltage, a closed loop charge pump architecture must be implemented. If not properly designed, an unstable closed loop architecture can create additional ripple in the loop when attempting to maintain a constant DC output, which may present itself in the form of one or more secondary effects that will hurt sensor performance. These effects include mode splitting, frequency shift, and Q variation.

5.2.1. Mode Splitting

Equations (5-4) and (5-5) were derived based on the assumption that the drive and sense modes of the gyroscope are matched. To match the modes of most gyroscopes, it is necessary to adjust the drive and/or sense frequencies until they are equal, which is accomplished by applying DC voltages at specific electrodes. For disk gyroscopes, the amount of device tuning can be determined by [90]

$$f_{tune} = f_0 \sqrt{1 - \varepsilon_0 \cdot h \cdot R \cdot \left(\frac{\theta_e}{2} + \frac{\sin(2\theta_e)}{4} \right) \cdot V_P^2 \cdot \frac{\left(\frac{1}{d_d^3} + \frac{1}{d_s^3} \right)}{K}} \qquad (5\text{-}8)$$

where h, R, θ_e, d_d, d_s, and K are the device thickness, device radius, span of the electrode angle, drive electrode capacitive gap, sense electrode capacitive gap, and device stiffness, respectively. Since f_{tune} is directly proportional to V_P^2, the drive and sense cannot be matched if V_P varies with time. Instead, the signal variation will introduce some error into equations (5-4) and (5-5), and the sensitivity and resolution of the gyroscope will be attenuated proportional to the magnitude of the voltage ripple.

5.2.2. Frequency Shift

In addition to mode splitting, the polarization voltage itself has a direct impact on the resonance frequency of the gyroscope, given by

$$\omega_0 = \sqrt{\frac{K_{Mechanical} - K_{Electrical}}{M_{Eff}}} \tag{5-9}$$

where $K_{electrical}$ and $K_{mechanical}$ represent the electrical and mechanical stiffness of the disk, respectively. While $K_{mechanical}$ is dependent upon the mechanical properties of the gyroscope, $K_{electrical}$ is calculated as [37]

$$K_{Electrical} = \frac{\varepsilon_0 A_{cap}}{d_0^3} V_P^2 \tag{5-10}$$

Based on (5-10), any variation in V_P will carry over into the electrical stiffness, causing ω_0 to fluctuate with the ripple. Although these effects may not be as severe due to the square-root proportionality of V_P to ω_0, it will add additional non-white noise to the output Coriolis current, as defined in (5-6).

5.3. Charge-Pump Architectures

Several options can be implemented to maximize the on-chip DC voltage generated by the charge pump. Of these options, the simplest involves switching to a process that offers a larger voltage headroom. A large headroom increases the absolute DC voltage amplification between each stage and reduces the number of pump stages, mitigating the circuit's body effect issues. However, increasing the minimum feature size of the process will also increase the power consumption and area of the complete ASIC, which may not be possible depending on the design criteria. As another option, the charge pump can be moved off the IC and brought onto the MEMS die. With this option, the body effect issue brought about through the use of MOS transistors will be removed, as a p-n junction

can be created directly on the silicon wafer. Depending on its size and function, this charge pump may not significantly increase the area of the sensor; however, all supporting electronics for the charge pump (input voltage, clock generator, regulation electronics) will still need to be provided by the interface IC. If a low voltage CMOS process must be used, alternate methods of improving charge pump efficiency and DC amplification are available. The methods have been divided in this thesis into four categories based on their optimization strategy (Fig. 5-4), and it may be possible to use either one method or a combination of several methods in the final charge pump design.

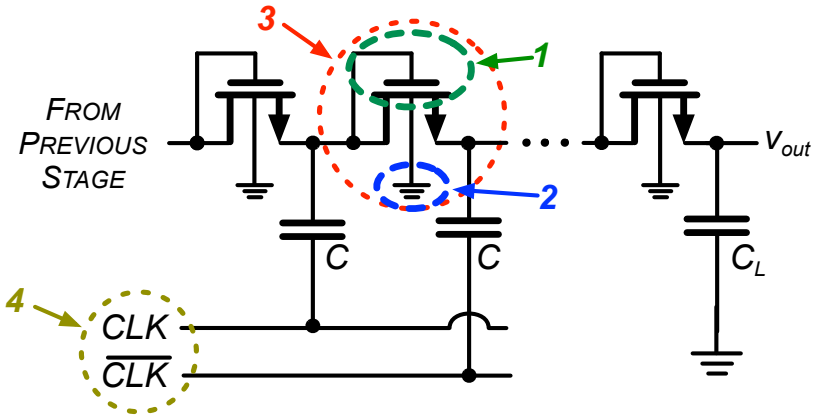

Figure 5-4 – Focus of different charge pump optimization methods

5.3.1. Gate-Voltage Boosting

It is difficult to compensate for the body effect in a standard low-voltage CMOS process because the substrate of every NMOS transistor is connected to a fixed voltage (V_{SS}). From (5-3), $V_t \propto \sqrt{V_s}$, which gets larger after each pump stage. Under gate-voltage boosting, the charge pump is designed so that at every stage additional voltage is applied to boost the gate voltage during the charge transfer phase of each MOS diode. The increase in V_{GS} effectively cancels the increase in V_t, and the pump can transfer voltage at or near maximum efficiency.

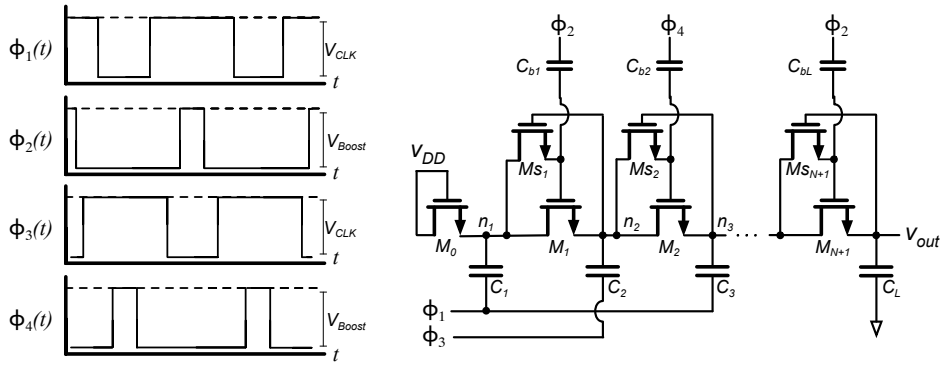

Figure 5-5 – Charge pump using 4-phase clock scheme

One of the more widely used methods of gate voltage boosting involves using four carefully designed clock signals to increase the voltage at the gate of each MOS diode during its 'on' phase [82]. The 4-phase charge pump and a plot of each clock waveform are shown in Fig. 5-5. The overlapping of primary clock signals ϕ_1 and ϕ_3 is critical to the pump's operation. While both signals are high, the gate of M_1 is pre-charged to V_{DD} through the Ms_1. Once M_1 has been charged, clock ϕ_3 turns off and ϕ_2 turns on, boosting the gate voltage of M_1 (through capacitor C_{b1}) by $V_{boost} \geq V_t$. The increase in the gate voltage provided in this boosting stage compensates for the body effect loss during charge transfer. After the charge transfer has been completed, ϕ_2 will turn off and the gate voltage of M_1 returns to V_{DD}. Using this scheme, the output voltage of the pump can be calculated as:

$$v_{out} = v_{in} + N \cdot \left(V_{CLK} \frac{C}{C_{fringe} + C} - \frac{i_{out}}{f_{CLK}\left(C_{fringe} + C\right)} - \left(V_t - V_{Boost}\right) \right) - V_t \qquad (5\text{-}11)$$

Although 4-phase charge pumps can effectively cancel body effect on first-order level, this architecture consumes additional power to generate ϕ_1-ϕ_4. In addition, more area may be needed to incorporate the clocking scheme correctly and route each stage of the pump to provide the right conditions for boosting the gate voltage.

5.3.2. Charge Transfer Switching

Another technique often used to boost the efficiency of the pump is charge transfer switching (CTS) [84]. In CTS (Fig. 5-6), MOS switches are used to transfer higher voltages from later stages of the chain back to transistors at earlier stages of the chain to compensate for V_t. The transistors denoted by M_d represent the diode portion of the chain and are used to set the initial voltages at each node of the charge pump, similar to the MOS diodes in the traditional Dickson architecture. Additionally, M_N, M_P, and Ms transistors are added for feedback and charge transfer operations.

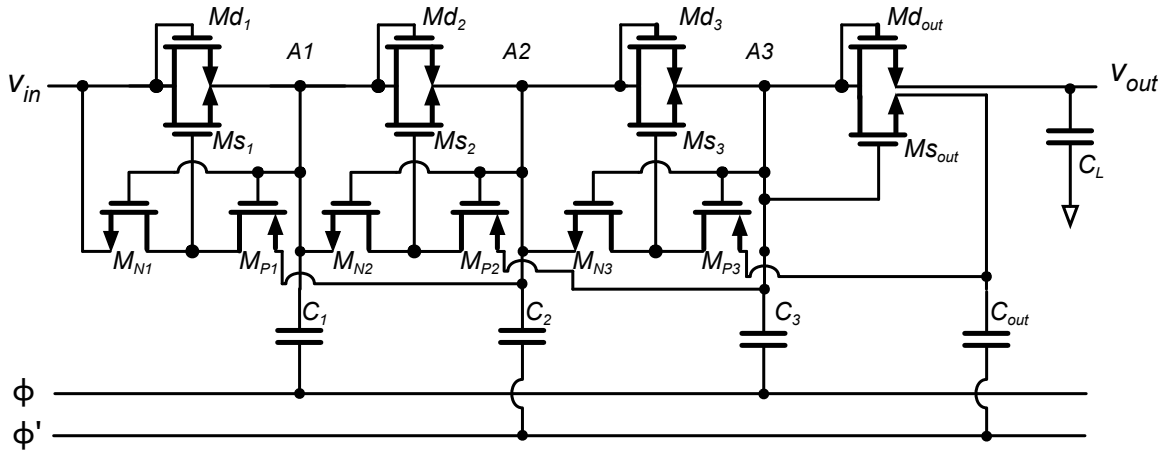

Figure 5-6 – Charge pump using CTS-based pump architecture

When ϕ is high, the voltages at nodes *A1* and *A3* are charged up to $V(A1)=V_{A1}=V_{in}+\Delta V$ and $V(A3)=V_{A2}+\Delta V$, respectively, where ΔV represents the net increase in voltage after each stage. Transistor Md_2 will turn on, presetting the voltage at node *A2* to $V(A2)=V_{A1}+\Delta V-V_t$. At the same time, the charged-up voltages at *A1* and *A3* turn M_{N2} off and M_{P2} on, passing *V(A3)* to the gate of Ms_2 [82]. The boosted gate voltage will turn Ms_2 on and eliminate the charge transfer loss across Md_2, setting $V(A2)=V_{A1}=V_{in}+\Delta V$. During the next half-cycle (ϕ is low), node *A2* will charge to $V(A2)=V_{A2}=V_{A1}+\Delta V$ while *V(A1)* and *V(A3)* will fall to V_{in} and V_{A2}, respectively, turning

Ms_2 off and Ms_3 on, setting the charge transfer for the next stage. After N stages, the output voltage of the CTS-based charge pump becomes

$$v_{out} = v_{in} + N \cdot \left(V_{CLK} \frac{C}{C_{f\,ringe} + C} - \frac{i_{out}}{f_{CLK}\left(C_{f\,ringe} + C\right)} \right) \tag{5-12}$$

Like 4-phase gate boosting architectures, CTS charge pumps require additional area expenditure, as 3 more transistors must be routed for each pump stage than for the traditional Dickson design. In addition to area, the extra transistors introduce more fringe capacitance, reducing the voltage transferred between each stage.

5.3.3. Diode Replacement

If power and area consumption need to be kept to a minimum, gate-voltage boosting and CTS techniques will not be effective strategies. Instead, it may be best to use a diode replacement technique, which seeks to simply replace the MOS diode. In [85], poly-silicon diodes are used in place of the NMOS transistors. The diodes are fabricated in CMOS by depositing the intrinsic poly-silicon layer provided by the CMOS process and doping it with n- and p-type impurities. Doing so will completely eliminate the body effect, leaving the V_t term in (5-2) fixed and independent of body effect. However, a specialized CMOS process is required to provide the n- and p-type doping on-chip, although it is reported that this may come standard in some newer CMOS processes [85].

5.3.4. Clock Voltage Amplification

Clock voltage amplification techniques [83, 86] are often used in conjunction with other charge pump optimization strategies, as they do not directly address the body effect problem. Instead, these techniques are used to increase the amplitude of the clock

generator operating the charge pump. From (5-2), it can be approximated that the charge pump output voltage is related to V_{CLK} by

$$v_{out} \propto N \cdot V_{CLK} \frac{C}{C_{fringe} + C} \tag{5-13}$$

A typical clock voltage-doubling circuit is shown in Fig. 5-7. During the first half cycle when ϕ is low, transistor M_{P2} will turn on, charging V_{C2} to V_{IN} (typically set to V_{DD}). At the next half cycle, the rise in V_{ϕ} will turn M_{P2} off, allowing the voltage at the drain of M_{P1} to rise to $V_{IN}+V_{CLK}=2V_{DD}$. This voltage acts as the supply voltage for an inverter when a low voltage input is applied so that the generated clock signal will have a rail-to-rail voltage of $\sim 2V_{DD}$.

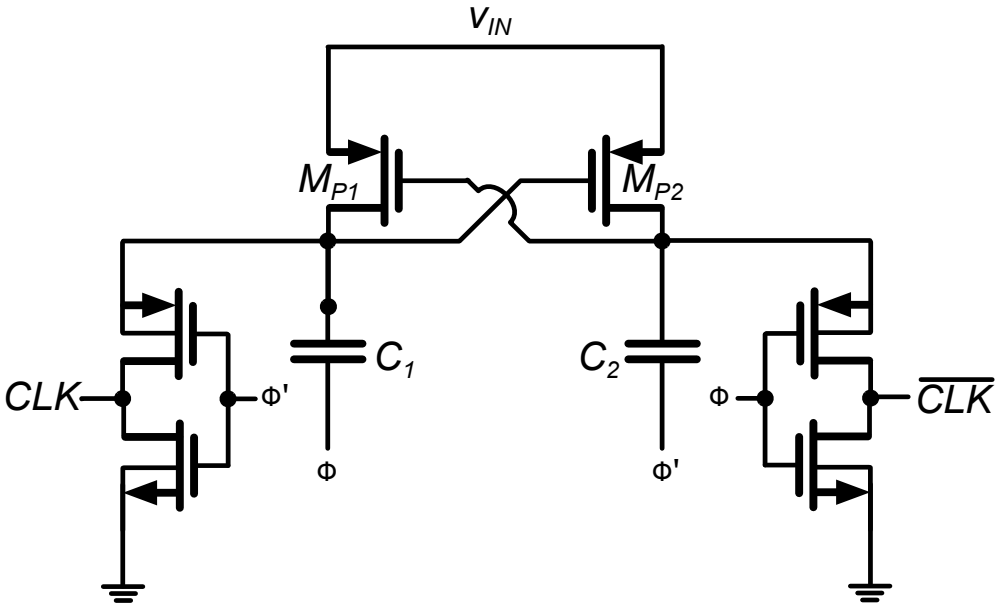

Figure 5-7 – Clock voltage-doubler architecture

Although the output voltage of the charge pump can be significantly improved with the incorporation of a voltage-doubling architecture, additional chip area and power consumption are needed to use these circuit blocks. However, because the circuitry only

modifies the clocking of the charge pump, V_t-cancellation strategies such as CTS can still be added to the chain to provide additional voltage amplification without affecting the performance of the clock doubler.

5.3.5. V_t Reduction Through Substrate Decoupling

Another method of compensating for the body effect involves decoupling the bulk voltage of each pump transistor from ground [87-89]. The bulk voltage is instead tied to the node of the transistor with the lowest voltage (typically to the source or another node from a previous stage). With the bulk connection rerouted, the V_{SB} term in (5-3) remains constant as charge is pumped to the later stages, reducing the body effect-related losses of the charge pump.

Most techniques that use substrate decoupling require a specialized CMOS process that offers deep N-well to provide a bulk connection that does not need to be grounded. It may also be possible to use PMOS diodes in place of the NMOS diodes, thereby creating an isolated n-well to which any potential can be applied. However, this must be done carefully so as to not activate any of the parasitic diodes present between the N-well, substrate, and transistor that would cause the charge pump to latch up.

One particular method of substrate decoupling involves the implementation of a negative charge pump (Fig. 5-8). It has the same architecture as the pump shown in Fig. 5-2, but with three distinct modifications. First, V_{IN} is set to V_{SS} instead of V_{DD}. Next, PMOS transistors are used along the pump chain instead of NMOS transistors. With the incorporation of PMOS transistors in the pump, each bulk connection in the chain can now be separated from the others, and as a result is connected to the highest voltage of the charge pump instead of V_{DD} or ground. As a result of these changes, the output DC

voltage of the pump drops below $0V$. In smaller supply voltage processes, negative and positive charge pumps may become necessary for generating the large voltages needed to actuate and tune the gyroscope.

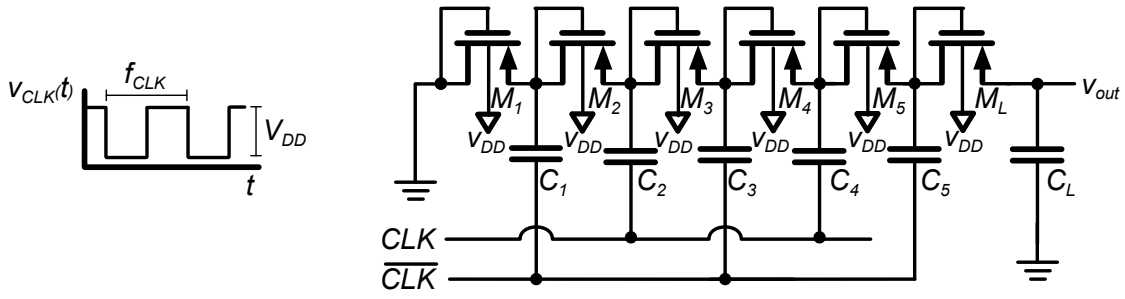

Figure 5-8 – Negative charge pump architecture

A table listing the benefits and tradeoffs of each technique used to amplify the charge pump voltage is listed in Table 5-1. From this table, one or more designs can be selected that offer the best performance based on the area, cost, and power parameters that have been established.

Table 5-1 – Benefits and tradeoffs of charge pump optimization techniques

4-Phase Charge Pump	• Works in standard CMOS process • Reduces body effect	• Larger area • Higher power consumption
CTS	• Works in standard CMOS process • Reduces body effect	• Larger area • Larger C_{fringe}
Diode Replacement	• Completely removes body effect	• May require special CMOS process
Clock Voltage Amplification	• Increases efficiency of pump in early stages	• Does not compensate for body effect • Larger area • Higher power consumption
Substrate Decoupling	• Reduces body effect • Certain architectures maintain power/area consumption	• May require deep N-well, triple-well CMOS

5.4. Closed-Loop Regulation of Charge Pumps

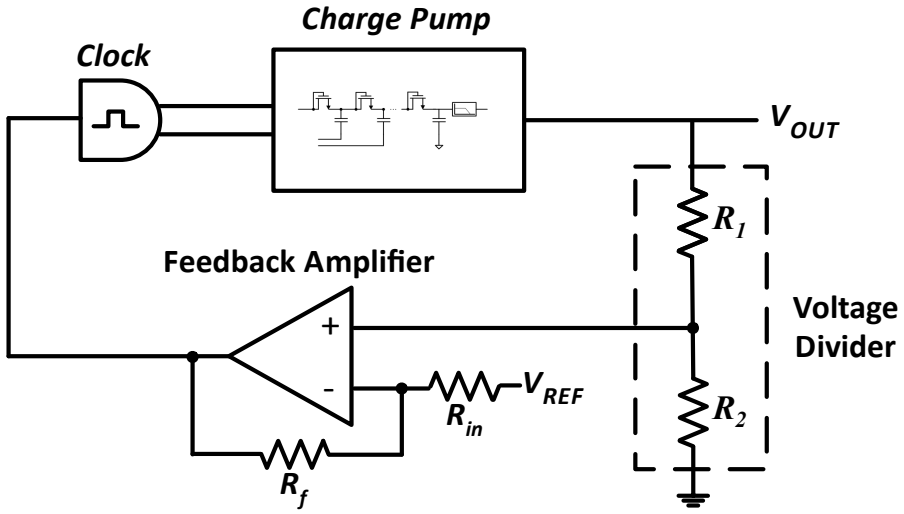

Figure 5-9 – Closed-loop charge pump architecture.

If a constant V_P generated on-chip is necessary for gyroscope operation, a regulated (closed-loop) charge pump design (Fig. 5-9) must be implemented. A closed-loop architecture allows the charge pump output to be tuned to a specific DC voltage. Additionally, the closed-loop configuration reduces the effects of short- and long-term shock, drift, and environmental variations on the pump output.

Most closed-loop charge pumps control the frequency or amplitude of the clock signal to regulate the output voltage, which provides the user with a large tuning range. It was suggested in [91] that i_{out} can also be used to control the output voltage of the charge pump through the use of current steering; however, this technique is not advisable as the current needed would dramatically increase the power consumption of the IC. Regulation can be accomplished through one of several strategies, which include: (1) turning off the clocks when V_{out} exceeds the desired output voltage [92], (2) reducing the amplitude of the clock signal when V_{out} reaches the desired output voltage, or (3) reducing the frequency of the clock signal when V_{out} reaches the desired output voltage.

Although design 3 is discussed in this thesis, each closed-loop design uses the charge pump and three other core blocks: a clock generator, voltage divider, and feedback amplifier.

5.4.1. Defining the Closed-Loop Transfer Function

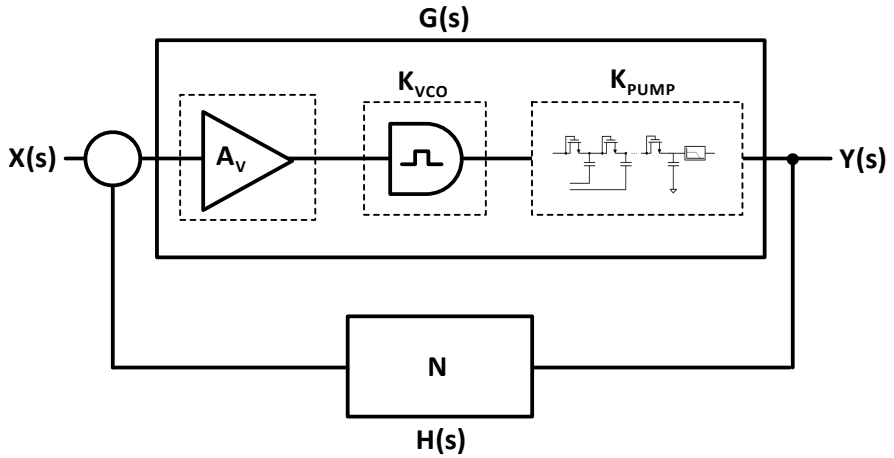

Figure 5-10 – Transfer function block diagram of closed-loop charge pump.

When connected as closed-loop system, the blocks discussed above create the diagram shown in Fig. 5-10. Based on this layout, the transfer function of the charge pump can be written as

$$\frac{Y(s)}{X(s)} = \frac{G(s)}{1 - G(s)H(s)} \tag{5-14}$$

Where G(s) and H(s) are given by

$$G(s) = A_v(s)k_{VCO}k_{pump} \tag{5-15}$$

and

$$H(s) = N \tag{5-16}$$

The input *X(s)* represents the reference voltage that is used to set the pump output voltage *Y(s)*, while $A_v(s)$, k_{vco}, and k_{pump}, and N represent the transfer functions of each block in

the closed loop – the voltage amplifier, clock generator, charge pump, and voltage divider, respectively. The forward gains of the VCO, charge pump, and voltage divider are proportional to their respective input signals, leaving the stability of the charge pump dependent upon the stability of the op-amp.

5.4.2. Closed-Loop Components

The following discussion relates to the design of clock-frequency controlling closed-loop architecture (design 3). However, each of the individual blocks can be used in other feedback architectures involving amplitude control, such as designs 1 and 2.

5.4.2.1. Clock Generator

An on-chip ring oscillator (Fig. 5-11) is used to generate the charge pump's clock frequency and amplitude. To control the frequency of the clock signal (as described by design 3), current-starved inverters are implemented along the oscillator chain, in which an additional NMOS transistor (M_{tune}) controls the current flowing through the inverter. As a result, the frequency of the clock signal (f_{clk}) is dependent upon the tuning voltage V_{tune} that is provided by the feedback amplifier.

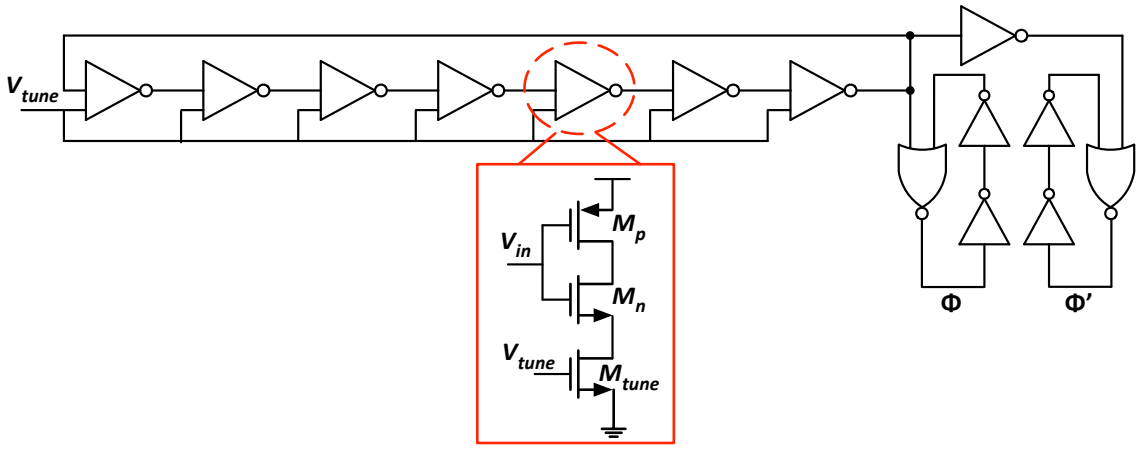

Figure 5-11 – Current-starved clock generator architecture.

5.4.2.2. Voltage Divider

A voltage divider is needed to step the output voltage of the charge pump down to a potential that will not damage the operation of the rest of the closed loop. For this reason, it should be composed entirely of passive components, either capacitive or resistive, which can withstand larger voltages than on-chip active components and therefore will not be damaged during pump operation. Charge pumps that use capacitive voltage dividers typically generate higher output voltage than resistive dividers, as they draw no current from the charge pump. Resistive dividers draw a small load current i_{out} that reduces the amount of voltage transferred at each stage of the charge pump (5-2). The voltage drop can be particularly significant for capacitive devices such as MEMS gyroscopes that have no resistive load. However, capacitive dividers consume significantly more area than resistive dividers and may be too large to layout in the space allotted for some older CMOS processes. For this reason, large resistive dividers of R_1=11 MΩ and R_2=1 MΩ were used in the design 3 implementation.

5.4.2.3. Feedback Amplifier

The last block of the charge pump regulation circuit is the feedback amplifier, which determines if the output voltage of the charge pump needs to increase, decrease, or remain unchanged. The non-inverting amplifier compares the reduced-DC output of the charge pump provided by the voltage divider to an external reference voltage V_{REF}. Based on these two voltages, an output signal is passed to the clock generator as V_{tune} to increase/decrease the frequency of the clock signal. A folded-cascode op-amp was implemented for design 3 because it offers a high open-loop gain while only introducing a single pole into the transfer function of the amplifier, given by

$$A_V(s) = \frac{\frac{A_0}{1 + A_0 f}}{1 + \frac{s}{(1 + A_0 f)\omega_{3dB}}} \tag{5-17}$$

where A_0 and ω_{3dB} represent the open-loop gain and 3-dB bandwidth of the amplifier, respectively. The feedback factor f can be defined as:

$$f = \frac{R_{in}}{R_f + R_{in}} \tag{5-18}$$

where R_f and R_{in} are the feedback and input resistors shown in Fig. 5-9, respectively. Combining Eqs. (5-14)-(5-18), the closed-loop transfer function of the charge pump is found to be

$$\frac{Y(s)}{X(s)} = \frac{A_0}{(1 + (A_0 f - NA_0))\frac{s}{\omega_{3dB}}} \tag{5-19}$$

5.5. Charge Pump Simulation and Measurement

Because charge pumps are based on switching, charge-pump circuit simulations are heavily dependent on transient simulations to estimate pump efficiency and output voltage. For closed-loop operation, it is necessary to perform periodic steady-state (PSS) analysis, particularly to determine periodic AC (PAC) and stability (PSTB) performance, which are used to ensure that the charge pump loop is stable.

5.5.1. Open-Loop Charge Pump simulations

Before beginning charge pump simulations, it is important to check the pump design to make sure the circuit does not have any parasitic diodes that may cause latch-up issues (as discussed in Chapter 5.1). The circuit simulator (in this thesis, Cadence) does not incorporate the MOS parasitic diodes created between the p-substrate and n-implant

regions that make up the source and drain of the transistor. Therefore, latch-up effects will not be detected in simulation. Reverse-biased diodes should also be added to the schematic as models of parasitic bulk-source and bulk-drain PN junctions.

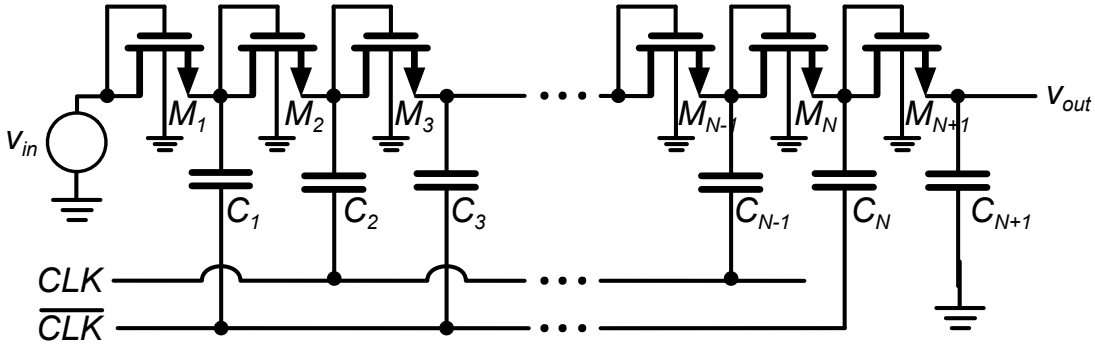

Figure 5-12 – Schematic of simulated charge pump.

Cadence simulations were performed on the charge pump in Fig. 5-12 using a pump chain of length N=7, supply voltage of V_{in}=3.3V, f_{CLK}=4.3 MHz, C_N=1 pF, and W/L=5.7. Substitution of these values into (5-2) yields an estimated charge pump output voltage of V_{out}=18.1V. Transient simulations (Fig. 5-13) show an output voltage of 15.7V, close to the expected value. However, there is significant voltage ripple (2.14 mV_{PP}) at the output due to the charging and discharging of the pump capacitors. This can be reduced significantly by incorporating a low-pass filter at the output of the charge pump. Using a 3rd-order passive LPF, the output voltage ripple is reduced from 2.14 mV_{PP} to 112 μV_{PP} while the pump output voltage is marginally reduced from 15.7V to 15.5V.

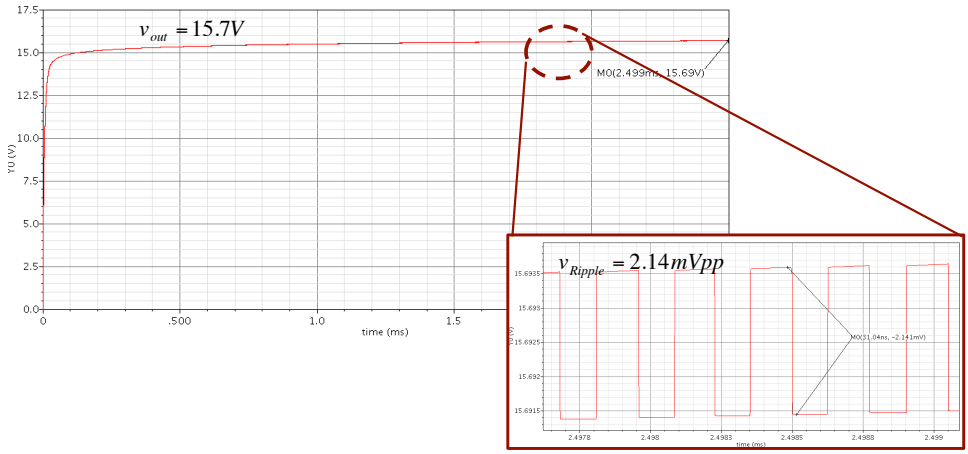

Figure 5-13 – Open-loop charge pump simulation. (inset) If no compensation is applied, the charge pump shows significant ripple at the output voltage.

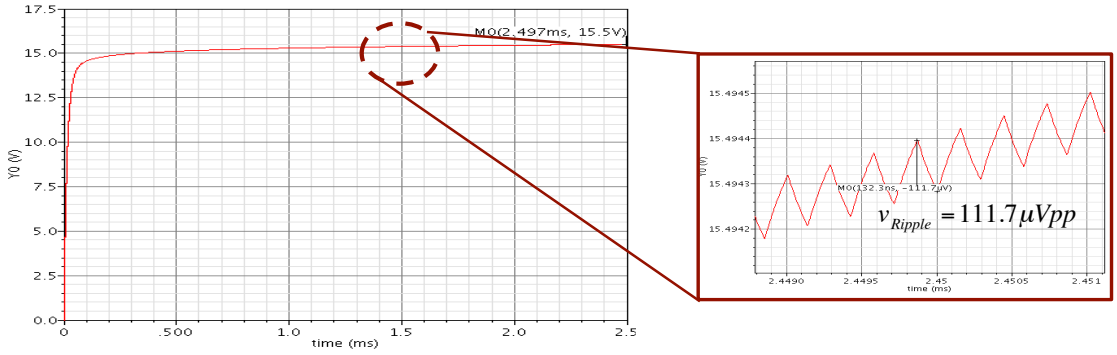

Figure 5-14 – Open-loop charge pump simulation with 3rd order passive low-pass filter. The charge pump output ripple is reduced significantly without significantly attenuating the output voltage.

5.5.2. Closed-Loop Charge Pump Simulations

The charge pump in Fig. 5-12 was implemented in the design 3 closed-loop implementation described in Chapter 5.4 (Fig. 5-9) with a 3rd order low-pass filter added to the charge pump output. Using this technique, transient simulations showed a reduction of ~2X in the loop ripple (Fig. 5-15). However, the closed-loop output voltage of the pump reduced to $12V$ from $16V$ due to the introduction of a resistive divider into the pump architecture.

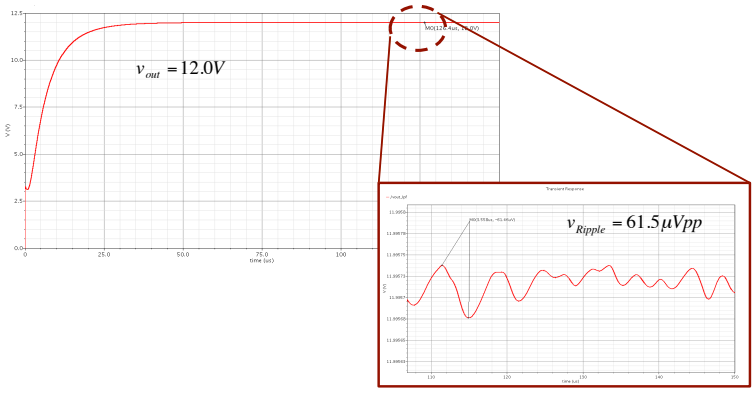

Figure 5-15 – Closed-loop charge pump simulation with 3rd order passive low-pass filter. The charge pump output ripple is further reduced, but the output voltage has also been attenuated due to the implementation of a resistive voltage divider.

After running transient analysis, PSTB simulations were performed to ensure the stability of the closed-loop. The loop was determined through simulation (Fig. 5-16) to have a phase margin of 62.2°, indicating good system stability. It should be noted that in charge pump PSTB simulations it is very important to include an exact beat frequency/period in the simulation. Varying from this frequency (period) can significantly alter the PSTB results and may prevent the simulator from reaching steady-state convergence.

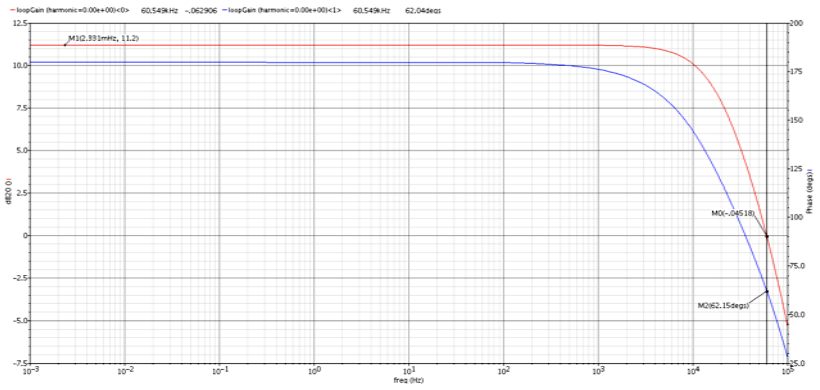

Figure 5-16 – PSTB simulation of closed-loop charge pump stability.

In addition to closed-loop stability analysis, temperature simulations were run on both the open-loop and closed-loop charge pump architectures to examine performance from 0-100 °C (Fig. 5-17). After closed-loop implementation, the temperature variation in the

charge pump output reduces from 3.2% to 0.4%. To further improve the temperature performance, the closed-loop gain of the charge pump should be increased and a temperature-insensitive control voltage V_{REF} should be implemented.

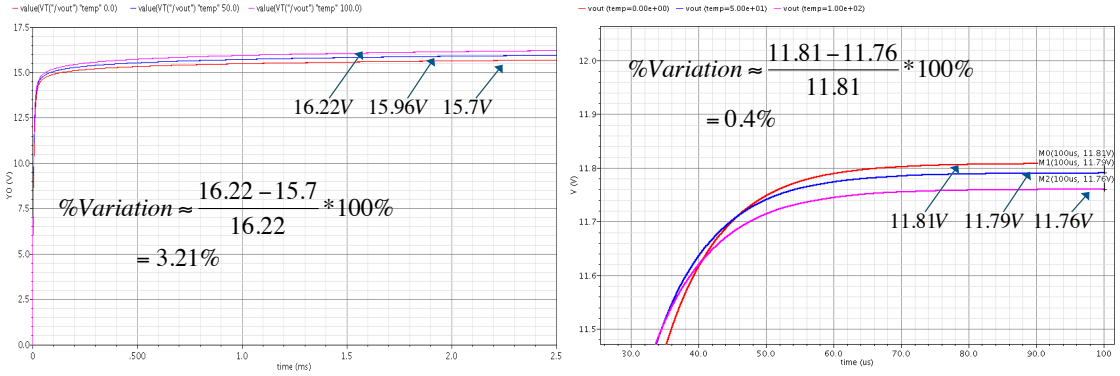

Figure 5-17 – Temperature sensitivity of charge pump in (left) open-loop and (right) closed-loop configurations

5.5.3. Charge Pump Measurement

After completing open- and closed-loop simulation of the charge pump circuitry, two charge pumps – a traditional Dickson charge pump and a negative charge pump – were fabricated on a 0.18µm CMOS process (Fig. 4-24). It was proposed that for CMOS processes with small feature sizes, the use of positive and negative charge pumps would allow a larger total voltage to be used across the gyroscope for both polarization and tuning (Fig. 5-18), increasing the effective voltages V_P and V_{Tune} that could be generated on-chip. Measurements of the closed-loop positive charge pump showed a pump voltage of only $8.7V$ when measured using an oscilloscope instead of the $15V$ expected from simulation (Fig. 5-19, left). However, it was determined that the total voltage of the charge pump was reduced due to the 1MΩ input impedance of the oscilloscope. Measurements were then retaken by connecting the charge pump directly to the gyroscope, measuring the Q and insertion loss (IL), and determining what DC voltage needed to be applied from an external reference (i.e. power supply) to match the reported

Q and IL. From this measurement, the charge pump output voltage was measured at $13V$, closer to what was observed in simulation (Fig. 5-19, right).

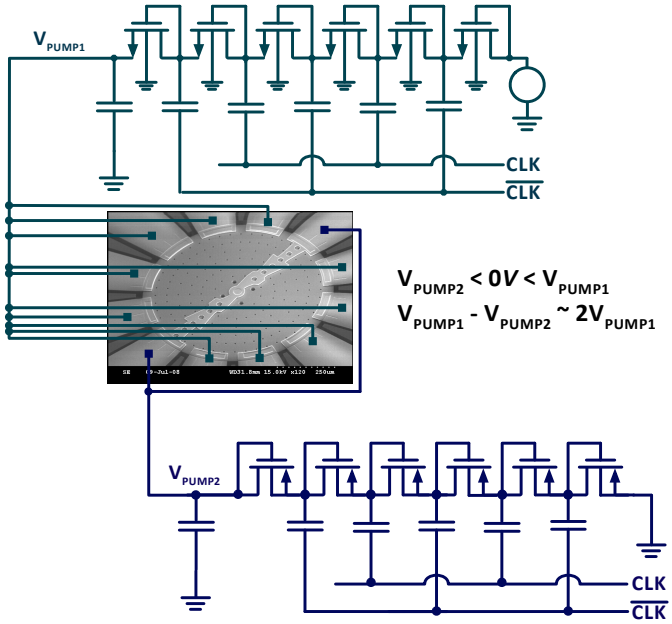

Figure 5-18 – Schematic of two-pump strategy for maximizing V_P and V_{Tune}. The positive and negative pumps provide ~2X the total pump voltage, which can then be applied independently for polarizing the disk or tuning the electrodes.

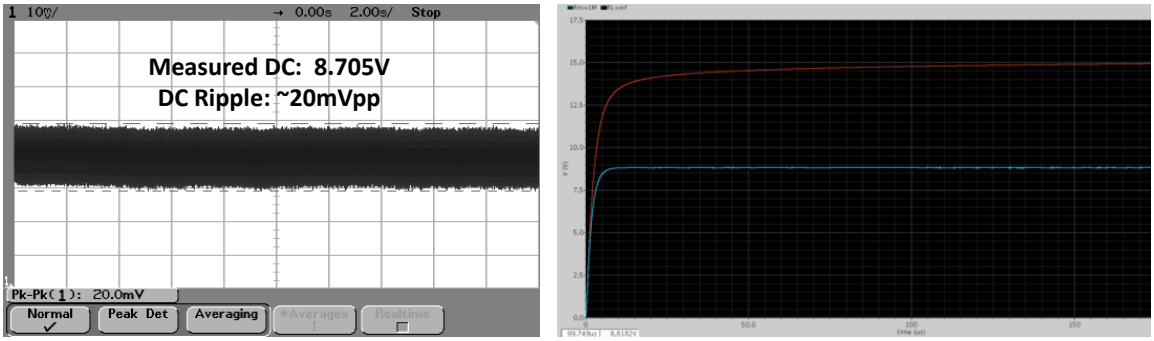

Figure 5-19 – (left) Measured output voltage of Dickson charge pump. The output voltage is attenuated due to the low impedance (1MΩ) of the oscilloscope. (right, red) Expected output voltage of charge pump (assuming no load). (right, blue) Expected output voltage of the charge pump (assuming 1MΩ load).

Unlike the positive Dickson charge pump, the negative charge pump did not reach a high voltage, instead showing on output voltage near -0.7V at the pump output. It was determined through device physics (Fig. 5-20) that the negative charge pump was

affected by latching between the n-well and p-substrate as the voltage dropped to below $0V$. In order to circumvent this problem, it is necessary to use a deep n-well process for the negative pump design to isolate the well from the p-substrate. Currently, these changes are still being made, so the results of the dual-pump operation are not reported in this thesis.

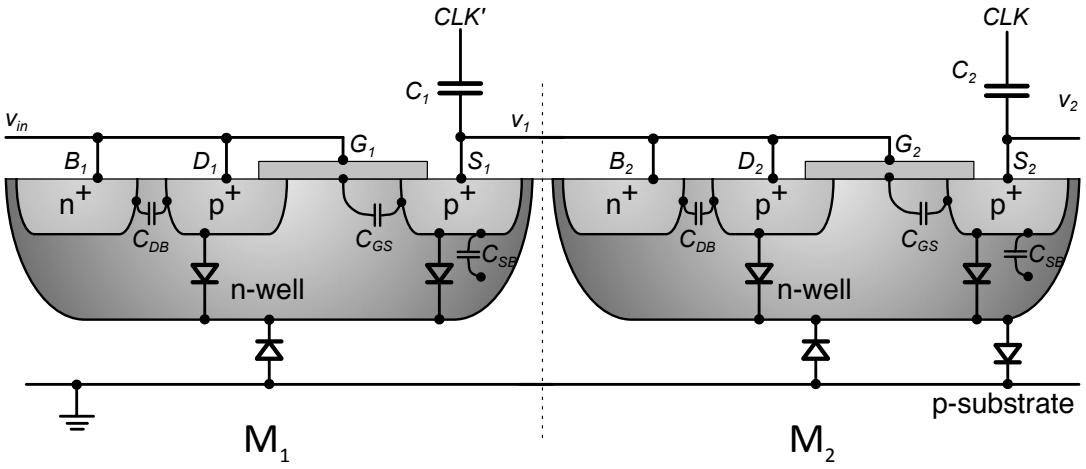

Figure 5-20 – Model of negative Dickson charge pump. As CLK' goes low, the parasitic diode between the p-substrate and n-well turns on, latching the DC output voltage and halting pump operation. This occurs across each stage of the pump whenever the clock voltage across C goes low.

.

CHAPTER 6

PHASE READOUT OF VIBRATORY GYROSCOPES

In recent years, the growing demand for high-precision MEMS gyroscopes has led to the development of new techniques and strategies for measuring device rotation rate. One such strategy involves the measurement of the phase-shift induced by the applied rotation. It has been shown in [93] that applying a Coriolis force induces a phase shift in the responses of the two resonance modes of the gyroscopes. For sufficiently small rotation rates, the phase shift is proportional to the angular velocity of rotation Ω_z. Therefore, it can be used to measure the gyroscope rotation rate using standard phase-detection circuitry.

Most state-of-the-art readout architectures interfaced with vibratory MEMS gyroscopes (including the design described in this thesis) rely on signal amplitude to measure the rotation rate applied to the device [9]. Other architectures have measured rate through a Coriolis-dependent frequency modulation of the output signal [94]. In both schemes, only one of two resonance modes of the device (referred to as the drive or primary mode) is electrically excited. The Coriolis force caused by a rotation around the gyroscope axis creates a coupling between the two modes, so that the amplitude (or frequency) of the second resonance mode (referred to as the sense or secondary mode) is proportional to the angular velocity of rotation Ω_z.

In the phase-shift readout scheme, the drive and sense resonance modes are both excited by forces that are of equal intensity but 90° out-of-phase. Compared to the

aforementioned traditional strategies, phase-based readout has several advantages. First, the amplitude of the output signal remains constant, thus minimizing the effect of additive noise. More importantly, an applied rotating excitation will induce a similar phase shift in the responses of the two resonance modes, mimicking the effect of physical rotation [95]. This fact can be exploited to devise self-calibrating gyroscope architectures [96-98] that do not require the addition of any moving parts to the gyroscope assembly.

In this chapter, an overview of the phase-shift readout scheme is provided. Both the conventional amplitude readout scheme and the phase-shift readout scheme are interfaced with two different 2-DOF mass-spring gyroscopes: a high-frequency bulk acoustic wave (BAW) disk gyroscope and a low-frequency mode-matched tuning fork gyroscope (M^2-TFG). Simulated and experimental data is collected on the performance of each scheme. Based on this data, a comparison of the amplitude and phase-shift readout schemes is performed along with techniques to monolithically integrate the phase-shift architecture. Following this comparison a calibration scheme for the phase-shift readout gyroscope is introduced, followed by simulated and measured results collected from the implemented architecture.

6.1. Theoretical Analysis of Phase Readout

The analysis that follows examines the effect of the Coriolis force on the response of a mode-matched vibratory gyroscope ($f_{drive} = f_{sense} = \omega_0/2\pi$) when excitations 90° out-of-phase with one another are applied to the two resonance modes of the device with matched frequencies. These modes are designated as *I* and *Q*, respectively. It is assumed that the gyroscope rotates around its *z*-axis (the sensitive axis) at a constant angular velocity Ω_z with respect to a fixed inertial frame of reference. Then the behavior of the

gyroscope can be analyzed in terms of its normal mode model, which consists of an equivalent 2-DOF mass-spring system, as described by

$$\begin{aligned} \ddot{x} + \frac{\omega_0}{Q}\dot{x} - 2\lambda\Omega_z y + \omega_0^2 x &= F_1 \cos(\omega_0 t) \\ \ddot{y} + \frac{\omega_0}{Q}\dot{y} + 2\lambda\Omega_z x + \omega_0^2 y &= F_2 \sin(\omega_0 t) \end{aligned} \tag{6-1}$$

where x and y are generalized coordinates, ω_0 is the resonance frequency of the mass-spring system, Q the quality factor, and λ a constant that depends on the gyroscope type and on the index of the resonance mode of the device [99]. The steady-state solution to this set of differential equations can be found using phasor analysis, transforming (6-1) into the following equivalent set of algebraic equations

$$j\omega_0 \begin{bmatrix} \omega_0/Q & -2\lambda\Omega_z \\ 2\lambda\Omega_z & \omega_0/Q \end{bmatrix} \begin{bmatrix} X \\ Y \end{bmatrix} = \begin{bmatrix} F_1 \\ -jF_2 \end{bmatrix} \tag{6-2}$$

The solution to these equations is

$$\begin{aligned} X &= \frac{1}{j\omega_0} \frac{(\omega_0/Q)F_1 - 2j\lambda\Omega_z F_2}{(\omega_0/Q)^2 + (2\lambda\Omega_z)^2} \\ Y &= -\frac{1}{j\omega_0} \frac{2\lambda\Omega_z F_1 - j(\omega_0/Q)F_2}{(\omega_0/Q)^2 + (2\lambda\Omega_z)^2} \end{aligned} \tag{6-3}$$

which corresponds to the following sinusoidal functions

$$\begin{aligned} x(t) &= \frac{Q}{\omega_0} \frac{\sqrt{(F_1\omega_0)^2 + (2F_2 Q\lambda\Omega_z)^2}}{\omega_0^2 + (2Q\lambda\Omega_z)^2} \sin(\omega_0 t - \theta_1) \\ y(t) &= -\frac{Q}{\omega_0} \frac{\sqrt{(F_2\omega_0)^2 + (2F_1 Q\lambda\Omega_z)^2}}{\omega_0^2 + (2Q\lambda\Omega_z)^2} \cos(\omega_0 t - \theta_2) \end{aligned} \tag{6-4}$$

where

$$\theta_1 = \tan^{-1}\left(\frac{2F_2 Q\lambda\Omega_z}{F_1\omega_0}\right),\ \theta_2 = \tan^{-1}\left(\frac{2F_1 Q\lambda\Omega_z}{F_2\omega_0}\right) \tag{6-5}$$

The expressions in (6-4) are the steady-state solutions of (6-1), and it can be seen that the Coriolis force introduces phase shifts θ_1 and θ_2 in the gyroscope response. For small values of Ω_z, these phase shifts are directly proportional to Ω_z.

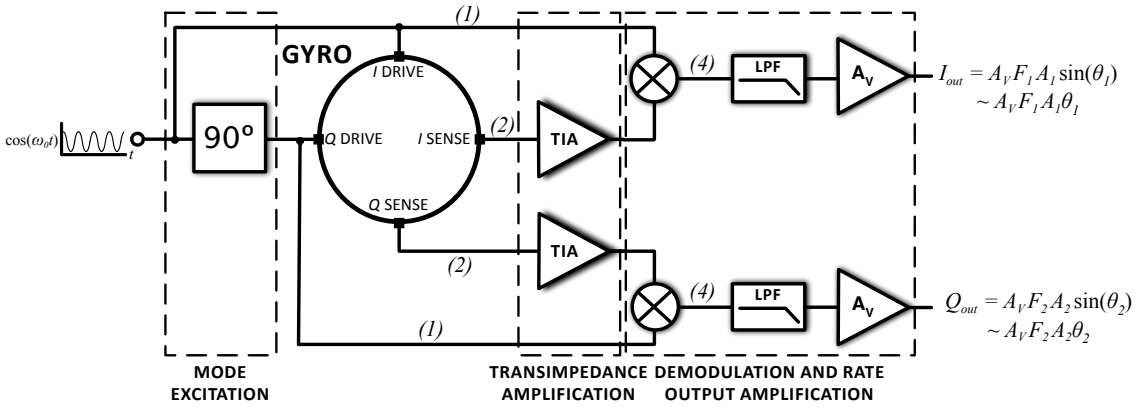

Figure 6-1 – Block diagram of phase readout architecture.

A block diagram of the phase readout architecture is shown in Fig. 6-1, in which the drive forces from (6-1) are applied to the two degenerate resonance modes of the gyroscope through the electrodes identified as I_{Drive} and Q_{Drive}, respectively. The gyroscope responses in (6-4) are seen at output terminals I_{Sense} and Q_{Sense}, which are 90° out-of-phase with each other as well as their respective inputs. After a Coriolis excitation is applied to the z-axis, the drive and sense signals from each complementary mode are multiplied together, giving

$$\begin{aligned} I_{mult}(t) &= F_1 A_1 \cos(\omega_0 t)\sin(\omega_0 t - \theta_1) \\ Q_{mult}(t) &= F_2 A_2 \sin(\omega_0 t)\cos(\omega_0 t - \theta_2) \end{aligned} \tag{6-6}$$

where A_1 and A_2 are the coefficients of the sine and cosine terms in (6-4). Using trigonometric identities, the expressions in (6-6) simplify to

$$I_{mult}(t) = \frac{F_1 A_1}{2}\left[\sin\left(2\omega_0 t - \theta_1\right) - \sin\left(\theta_1\right)\right]$$
$$Q_{mult}(t) = \frac{F_2 A_2}{2}\left[\sin\left(2\omega_0 t - \theta_2\right) + \sin\left(\theta_2\right)\right] \quad (6\text{-}7)$$

Following the low pass filtering and rate output amplification stages, the frequency components at $2\omega_0$ are removed from (6-7), reducing the signal of the phase readout scheme output to

$$I_{out}(t) = -\frac{F_1 A_1}{2}\sin\theta_1,\ Q_{out}(t) = \frac{F_2 A_2}{2}\sin\theta_2 \quad (6\text{-}8)$$

in which $\sin\theta \approx \theta$ for small values of θ.

6.2. Simulation Results

The amplitude and phase-shift responses of the gyroscope to an applied Coriolis signal were verified through ANSYS numerical simulations of the BAW disk gyroscope [5, 100] and M^2-TFG [27]. In these simulations, each respective device was mode-matched and tested using various rotation rates to determine scale factor sensitivity and full-scale range.

In contrast to the BAW, the M^2-TFG is comprised of two proof masses supported by a network of flexural springs anchored to a central post with control electrodes symmetrically distributed around the proof masses [5]. The tuning fork can attain high quality factors because its large proof mass and optimized anchor and flexural mode design reduce device surface and support losses, as well as thermo-elastic damping. However, the large size and flexural actuation of the structure also result in a resonance frequency almost 1000 times lower than that of the BAW disk gyroscope.

To measure the Coriolis-induced amplitude response of the gyroscope, a sinusoidal signal operating at the device's resonance frequency was applied to a single (drive)

electrode on the disk. Simulated rotation rates from 0 to 2100 °/s and from 0 to 10 °/s were applied to the BAW gyroscope and M^2-TFG, respectively, and the Coriolis-induced output current was measured and plotted from a single (sense) electrode. The applied input power and rotation rates were kept identical for each type of gyroscope to ensure that any variation in performance was not caused by any external stimuli but rather due directly to the device response.

Using the criteria outlined above, ANSYS simulations showed a scale factor sensitivity of 127.7 pA/°/s for the BAW gyroscope and 168.0 pA/°/s for the M^2-TFG, respectively (Fig. 6-2, 6-3). Furthermore, the BAW disk was found to have a linear full-scale range beyond 2000 °/s, while the tuning-fork showed a full-scale range of up to 10 °/s. Because simulations of the device mechanical noise floor could not be performed in ANSYS, no dynamic range calculations were made; however, it is assumed that the mechanical noise floor (i.e. Brownian noise contribution) of the gyroscope would be identical regardless of what readout scheme was implemented.

To observe the Coriolis-induced phase-shift response of the gyroscope, sinusoidal input excitations were applied to the drive electrodes aligned with one of the degenerate resonance modes (I_{Drive}). At the same time, excitations of equal amplitude but 90° out-of-phase were applied to the drive electrodes aligned with its complementary degenerate mode (Q_{Drive}). Simulated rotation rates identical to those used in the amplitude readout simulations were applied to the gyroscope, and the phases of the output currents at all the electrodes were obtained and plotted.

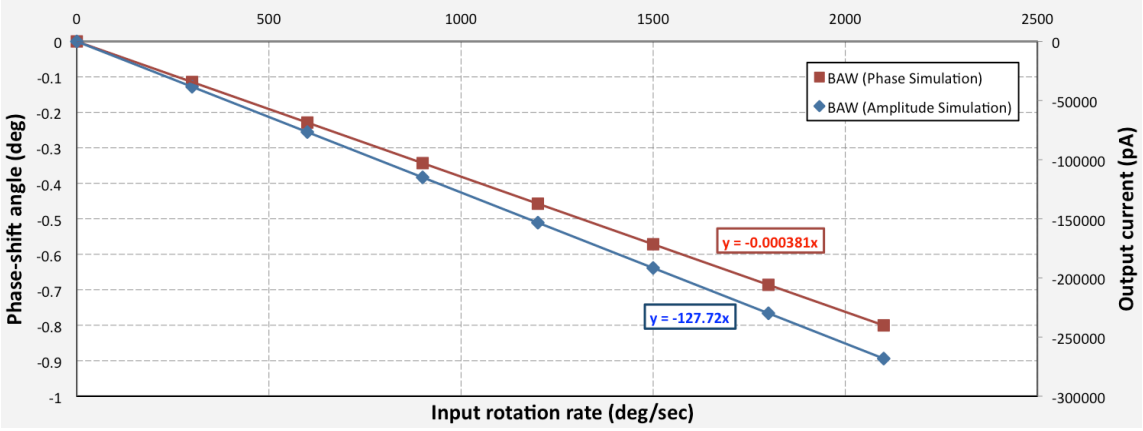

Figure 6-2 – Simulated amplitude (blue) and phase shift (red) response in the BAW disk gyroscope due to Coriolis force, measured relative to its value at zero rotation rate. The solid lines show the best linear fit to the data.

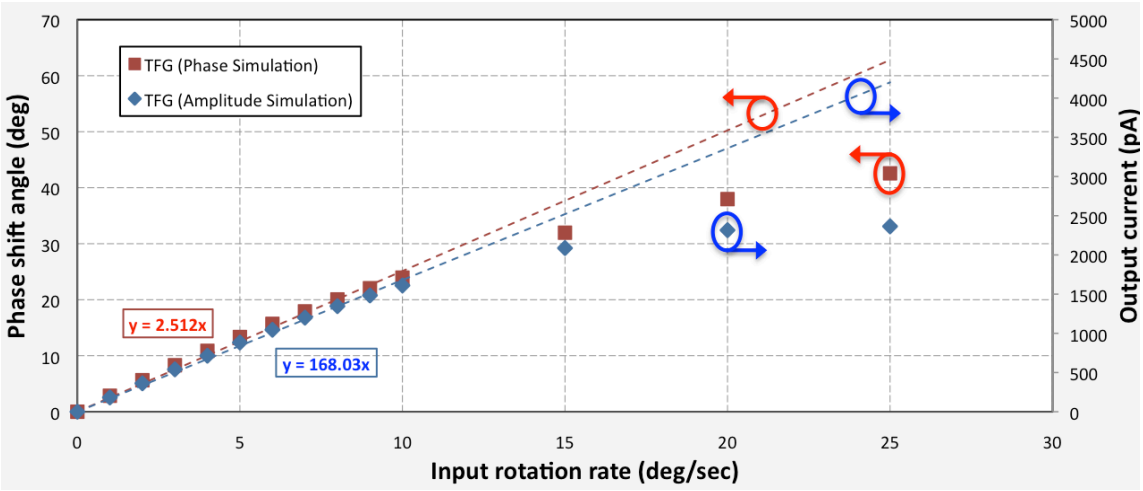

Figure 6-3 – Simulated amplitude (blue) and phase shift (red) response in the M^2-TFG due to Coriolis force, measured relative to its value at zero rotation rate. The solid lines show the best linear fit to the data.

The phase-shift readout scheme showed a linear response to the input excitation, confirming the theoretical analysis described previously. With this scheme, an extracted scale factor sensitivity of 3.81×10^{-4} °/(°/s) was simulated for the BAW gyroscope, while a sensitivity of 2.51 °/(°/s) was simulated for the M^2-TFG. Simulation showed that the phase-shift sensitivity of the device also provided a linear response to rotation rate. Additionally, both schemes were found to have similar full-scale ranges to their

equivalent amplitude readout architectures, with the BAW gyroscope again showing a range above 2000 °/s and the tuning-fork a maximum linear range of ~10 °/s.

6.3. Measured Results

To experimentally compare the amplitude and phase-shift readout schemes and verify the results from theoretical analysis and numerical simulation, 4 separate printed circuit boards (PCBs, Fig. 6-4) were fabricated to test each device (BAW, M^2-TFG) in each configuration (amplitude readout, phase-shift readout). This allowed the unique footprints and traces of each device or readout scheme to be placed without adding complexity and size to the PCB that would only serve to degrade the signal.

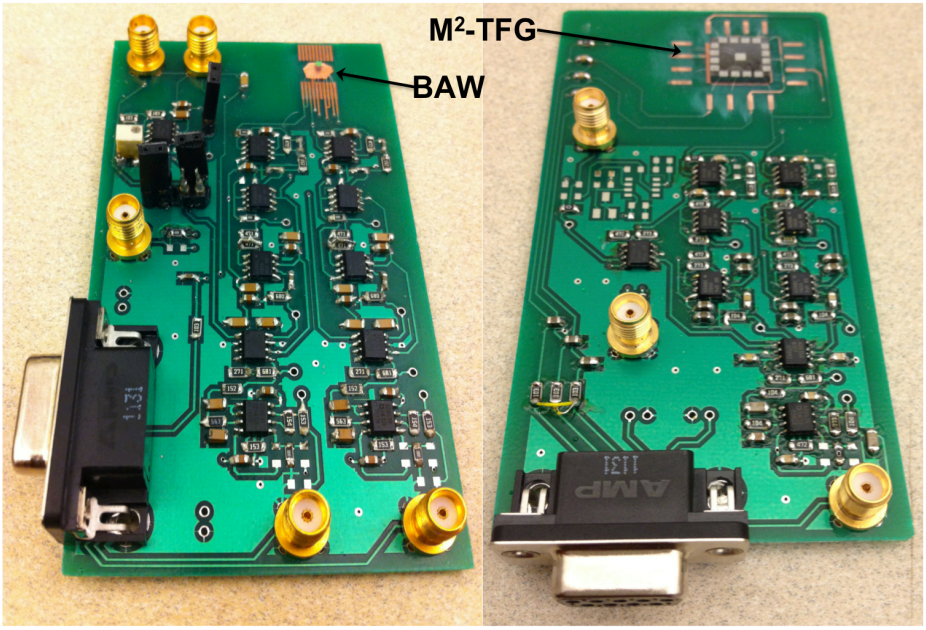

Figure 6-4 – (left) BAW phase-shift readout and (right) M^2-TFG amplitude readout circuit boards.

A schematic of the amplitude readout PCB is shown in Fig. 6-5. The input drive voltage is generated open-loop from an external Agilent 4395A network analyzer locked to the resonance frequency (f_0) of the respective gyroscope. This sinusoid is passed to the input drive electrode of the gyroscope, while a differential sense output is taken from two

180° out-of-phase sense electrodes. With the BAW interface, the differential sense signal was passed to a pair of Texas Instruments (TI) OPA657 [101] trans-impedance amplifiers to provide current-to-voltage conversion and magnification of the amplitude-modulated Coriolis signals. Each signal was then passed through two TI OPA656 [102] voltage amplifiers that provide additional amplification and buffering of the trans-impedance output.

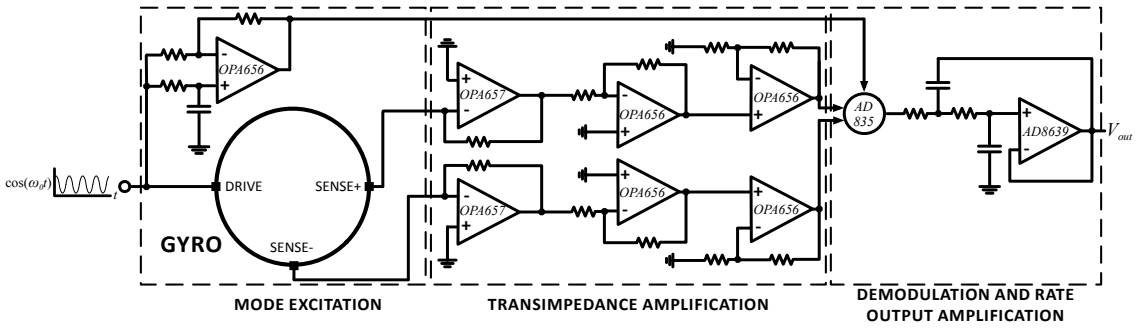

Figure 6-5 – Schematic of amplitude readout interface architecture.

After the initial amplification, the sense signals were mixed with the input carrier signal using an Analog Devices AD835 multiplier [103]. A tunable phase shifter was connected between the input sinusoid and the multiplier to ensure that the drive and sense signals were in-phase during demodulation to maximize the output voltage. After demodulation, the Coriolis signal was extracted through low-pass filtering, re-amplified, and passed to an oscilloscope for measurement. For the M^2-TFG, the input TIA was replaced with an OPA656, which provided higher open-loop gain than the OPA657. The remaining amplifiers on this board matched their counterpart on the BAW PCB; however, the gain and bandwidth of each stage was adjusted for use with a low-frequency gyroscope.

For the amplitude readout configuration, sinusoidally varying rotation rates were applied (0 dBm for BAW, -4dBm for M^2-TFG) via an Ideal Aerosmith rate table until the scale factor of the sensor was no longer linear. The corresponding output signals for the BAW and M^2-TFG are shown in Fig. 6-6 and Fig. 6-7, respectively. From the measurements, the BAW sensor was shown to have a sensitivity of 0.0431 mV/°/s, with linear scale factor up to the maximum rate applied on the rate table (200 °/s). Higher scale-factor measurements could not be performed due to the physical limitations of the wire connections on the rate table. The tuning-fork showed a sensitivity of 26.42 mV/°/s, linear up to 60 °/s. The variation between the simulated and measured linear range of the M^2-TFG is due to the application of a larger drive amplitude from simulation than that from the PCB, permitting higher rotation rates to be applied before the tuning fork output began to saturate.

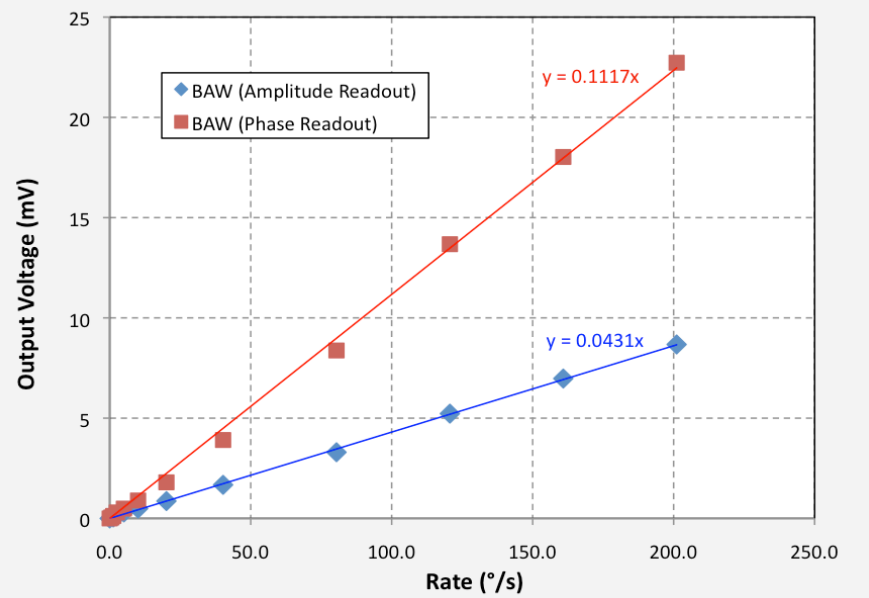

Figure 6-6 – Measured amplitude and phase shift responses due to Coriolis force for the BAW gyroscope, each relative to its value at zero rotation rate. Each solid line shows the best linear fit to the data.

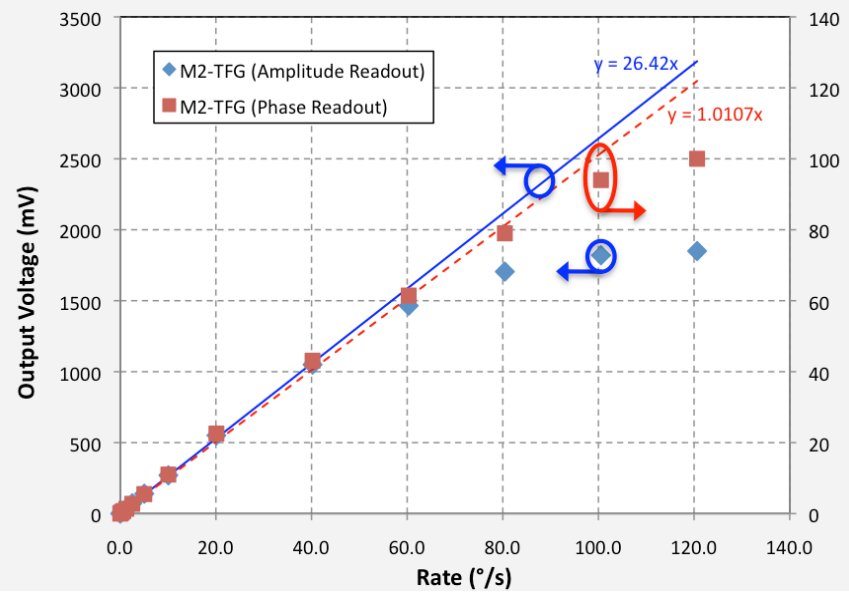

Figure 6-7 – Measured amplitude and phase shift responses due to Coriolis force for the M^2-TFG, each relative to its value at zero rotation rate. Each solid line shows the best linear fit to the data.

Unlike the amplitude readout architecture, separate demodulation and rate amplification chains were used in the phase-shift scheme to read out the *I*-mode and *Q*-mode sense signals. However, identical amplifiers were used on the phase-shift PCBs that matched their complement on the amplitude readout PCB. Furthermore, the gains of the amplifiers, phase shifters, and mixers and the cutoff frequency of the filters were matched for all readout boards of the same device. This ensured that any variations in performance between the two readout schemes would be attributed to the device and not to any associated interface circuitry. For this reason, the PCBs were not optimized to achieve the best performance for either the amplitude or phase-shift readout schemes.

To test the phase-shift architecture, the BAW and tuning-fork devices previously characterized on the amplitude readout PCBs were transferred to their respective phase-shift boards (Fig. 6-8). Sinusoidally varying rotation rates were applied via the rate table until the scale factor of the sensor was no longer linear. From these sinusoidally-applied rotations, sinusoids were also observed at output signals I_{out} and Q_{out} with amplitudes

proportional to the applied rotation rate. At the applied rates, it was derived that θ_1 and θ_2 would remain small enough for (6-5) to operate in the small angle domain. For both devices, the linearity of the collected measurements confirms the response predicted by the theoretical calculations and numerical simulations

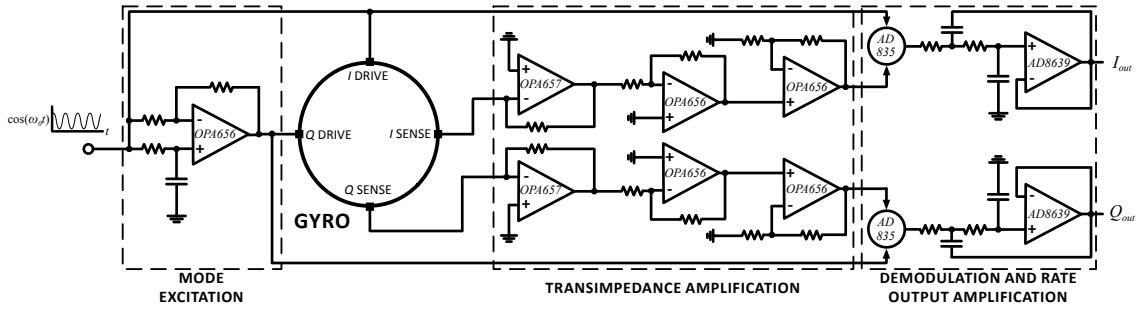

Figure 6-8 – Schematic of phase-shift readout architecture.

Under the phase readout architecture, the measured data points were closely aligned along a straight line with a slope of 0.117 mV/°/s (Fig. 6-6) for the BAW gyroscope and 1.0107 mV/°/s (Fig. 6-7) for the M^2-TFG. As with the amplitude measurements, the BAW gyroscope output remained linear at the maximum applied rate (200 °/s), while the linear range of the M^2-TFG improved slightly to 60 °/s, following the expected tradeoff between sensitivity and full-scale range.

To make accurate comparisons between the amplitude and phase-shift readout schemes, Allan variance measurements were taken for each of the 4 PCBs following the scale factor measurements. Under amplitude readout, the BAW disk and tuning-fork were shown to have bias instabilities of 0.33 °/s and 1.38×10^{-3} °/s (Fig. 6-9), with angle random walk (ARW) of 24.7 °/√hr and 0.12 °/√hr, respectively. With phase-shift readout, the bias instability and ARW of the BAW and M^2-TFG degraded to 0.84 °/s and 4.29×10^{-2} °/s (Fig. 6-9), with angle random walks of 50.3 °/√hr and 2.95 °/√hr, respectively. From these measurements, it can be seen that both techniques perform

comparably to one another, particularly with the BAW gyroscope. Based on the superior sensitivity of the BAW phase-shift readout scheme, improvements in the interface circuitry design can bring the bias instability below that of an amplitude-readout architecture operating under similar conditions. The M^2-TFG, however, has ~30X poorer bias drift performance, suggesting a deterioration in performance due to the asymmetry of the complementary drive forces, along with a reduction in the total sense area when compared with the amplitude readout configuration (as suggested by the improved dynamic range). To improve the phase-shift bias instability for this device, the phase angle θ_N of either the *I*- or *Q*- mode must be amplified by manipulating the drive forces F_1 and F_2 to change θ_1 and θ_2 as described in (6-5).

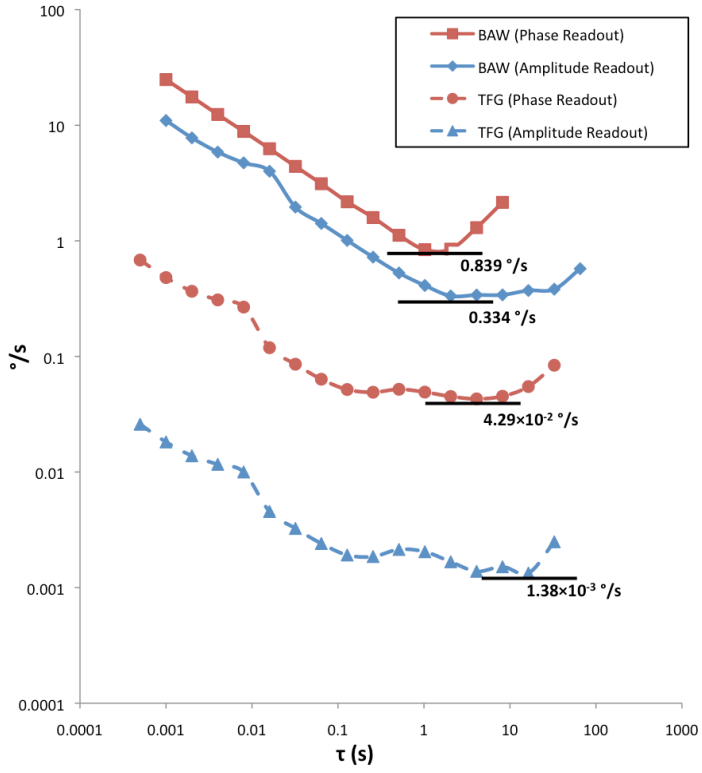

Figure 6-9 – Measured bias drift of BAW gyroscope (solid) and M^2-TFG (dashed) using amplitude (blue) and phase shift (red) readout schemes. Each solid line shows the bias instability of the respective architecture.

6.4. Discussion

The simulated and measured performance of both gyroscopes (Table 6-1) demonstrates that the phase-shift readout scheme can provide comparable performance to conventional amplitude readout architectures while also facilitating on-chip level calibration, particularly for the BAW disk design. In principle, this readout scheme can be applied to any gyroscope that can be modeled by a 2-DOF mass-spring system. As mentioned in [9], the phase readout scheme can be integrated with a calibration scheme that does not require the use of a rotary stage for proper operation. With this in mind, the next challenge becomes monolithically integrating the phase-shift readout scheme on a CMOS IC. Although the sense channels of the two schemes are nearly identical, the phase-shift architecture requires drive excitations of equal amplitude but 90° out-of-phase applied to I_{Drive} and Q_{Drive}, respectively. This requires interface circuitry that can simultaneously actuate the complementary drive modes while maintaining the orthogonality between the two signals.

Table 6-1 – Performance summary of amplitude and phase-shift readout architectures used with BAW and M^2-TFG gyroscopes

	SIMULATION		MEASUREMENT	
	BAW	**M^2-TFG**	**BAW**	**M^2-TFG**
Q	20,000	50,000	32,000	60,000
f_0	10 *MHz*	5.95 *kHz*	9.65 *MHz*	11.7 *kHz*
Amplitude Readout				
Sensitivity	127.7 *pA/°/s*	168.0 *pA/°/s*	0.112 *mV/°/s*	26.42 *mV/°/s*
Full-Scale Range	> 2000 *°/s*	10 *°/s*	> 200 *°/s*	~ 40 *°/s*
Bias Drift	-	-	0.334 *°/s*	1.38×10^{-3} *°/s*
Angle Random Walk	-	-	24.7 *°/√hr*	0.12 *°/√hr*
Phase-Shift Readout				
Sensitivity	3.81×10^{-4} *°/(°/s)*	2.51 *°/(°/s)*	0.043 *mV/°/s*	1.01 *mV/°/s*
Full-Scale Range	> 2000 *°/s*	10 *°/s*	> 200 *°/s*	~ 60 *°/s*
Bias Drift	-	-	0.839 *°/s*	4.29×10^{-2} *°/s*
Angle Random Walk	-	-	50.3 *°/√hr*	2.95 *°/√hr*

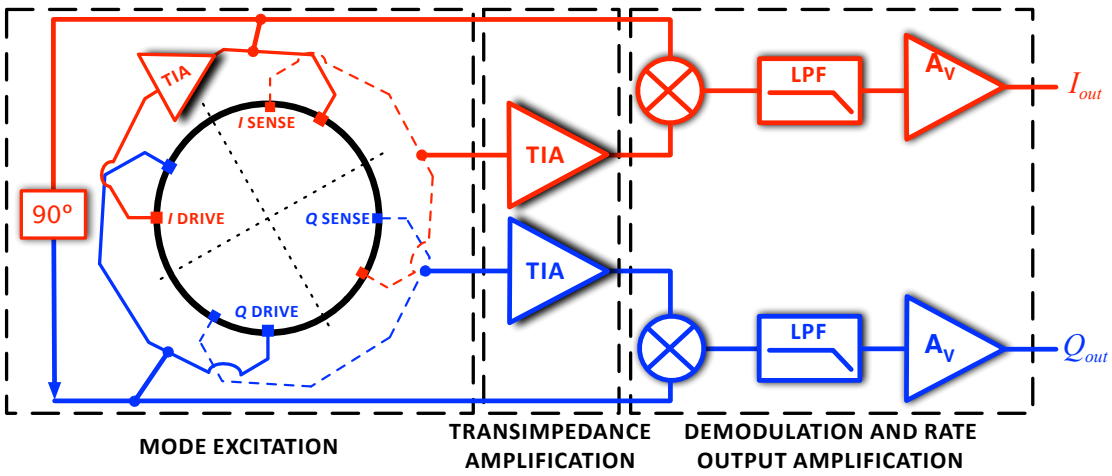

Figure 6-10 – Block diagram of phase-shift readout ASIC.

A block diagram of the phase-shift interface ASIC is shown in Fig. 6-10, in which the *I*- and *Q*-modes of the gyroscope are depicted in red and blue, respectively. Using this architecture, the interface electronics for the sense channel can be brought over directly from amplitude readout ASICs used in identical devices [34, 104]. For the BAW gyroscope, only a single output channel is needed, as the forces F_1 and F_2 acting on the *I*- and *Q*-modes are identical and therefore yield the same output. The drive channel, however, requires additional circuitry to provide the 90° phase shift needed to excite Q_{Drive}, which can be done by inducing self-excitation of *I*-mode through a positive feedback connection between two unique I_{Drive} electrodes (as performed in conventional amplitude readout schemes) and using a PLL, integrator, or supplementary circuit to generate the required phase shift. As a consequence of the drive mode complexity, the circuit may require more area and higher power consumption than amplitude readout ASICs; however, this conclusion cannot be fully reached until after the ASIC has been thoroughly characterized. It is likely that the power consumption of these additional

blocks can be minimized using digital electronics, suggesting that the phase readout scheme can operate at or near the same power as amplitude readout schemes.

6.5. Theoretical Analysis of Calibration

In the calibration state, it is assumed that the gyroscope is fixed in an inertial frame of reference. A sinusoidal excitation is applied to the gyroscope in such a way that the direction of the excitation rotates in the generalized coordinates plane at angular velocity Ω_z. This is equivalent to applying amplitude-modulated excitations in the direction of the coordinate axes, which correspond to the two resonance modes of the device. Under these assumptions the behavior of the gyroscope is described by

$$\begin{aligned} \ddot{x} + \frac{\omega_0}{Q}\dot{x} + \omega_0^2 x &= F_0 \cos(\Omega_z t)\cos(\omega_0 t) \\ \ddot{y} + \frac{\omega_0}{Q}\dot{y} + \omega_0^2 y &= F_0 \sin(\Omega_z t)\sin(\omega_0 t) \end{aligned} \tag{6-9}$$

In contrast to (6-1), the two differential equations are now decoupled and can thus be solved independently. The corresponding solutions can be obtained by exploiting the trigonometric identities

$$\begin{aligned} \cos(\Omega_z t)\cos(\omega_0 t) &= \frac{1}{2}\left[\cos((\omega_0 + \Omega_z)t) + \cos((\omega_0 - \Omega_z)t)\right] \\ \sin(\Omega_z t)\sin(\omega_0 t) &= \frac{1}{2}\left[\cos((\omega_0 + \Omega_z)t) - \cos((\omega_0 - \Omega_z)t)\right] \end{aligned} \tag{6-10}$$

Standard sinusoidal steady-state analysis techniques can then be used to obtain expressions for the gyroscope response, which is determined by

$$H(j\omega) = \omega_0^2 - \omega^2 + j\frac{\omega_0}{Q}\omega \tag{6-11}$$

Assuming that $|\Omega_z| << \omega_0$, the following approximate equality holds:

$$\left|H\left[j\left(\omega_0 + \Omega_z\right)\right]\right| \cong \left|H\left[j\left(\omega_0 - \Omega_z\right)\right]\right| \tag{6-12}$$

It can then be shown that the solutions of (6-9) are given by the following expressions

$$\begin{aligned} x(t) &= \frac{F_0}{A}\cos\left(\Omega_z t - \theta_0\right)\sin\left(\omega_0 t\right) \\ y(t) &= \frac{F_0}{A}\sin\left(\Omega_z t - \theta_0\right)\cos\left(\omega_0 t\right) \end{aligned} \tag{6-13}$$

where

$$\begin{aligned} A &= \left|H\left[j\left(\omega_0 + \Omega_z\right)\right]\right| \cong \left|H\left[j\left(\omega_0 - \Omega_z\right)\right]\right| \\ \theta_0 &= \tan^{-1}\frac{2Q\Omega_z}{\omega_0} \end{aligned} \tag{6-14}$$

It can be seen from (6-13) and (6-14) that the application of amplitude-modulated excitations to the drive and sense modes of the gyroscope induces a phase shift in the modulating envelope of the gyroscope response. For small values of Ω_z, this phase shift is proportional to Ω_z through a constant equal to $(2Q/\omega_0)$. Apart from a factor of λ, this is the same proportionality constant that relates the phase shift in the gyroscope response created by the Coriolis force to the rotation rate Ω_z (assuming $F_1 = F_2$) in (6-5). It follows that a rotating excitation can be substituted for physical rotation for the purpose of calibrating the gyroscope, because for a given type of gyroscope the value of λ depends only on the index of the resonance mode of the device.

Since the 2-DOF mass-spring model describes the behavior of a large class of resonating gyroscopes, the results of this analysis are applicable to a wide variety of devices, such as disk, ring, hemispherical shell and mode-matched tuning-fork gyroscopes.

6.6. Simulations of Phase-Shift Calibration Scheme

Following characterization of the phase-shift readout architecture, the gyroscope response to a rotating excitation - in this case, a rotating electrostatic field - was evaluated in a second set of simulations. In these simulations, amplitude-modulated excitations according to the expressions given in (6-9) were applied to the gyroscope electrodes aligned with the drive and sense modes. The phases of the output currents at all the electrodes were recorded at eight different values of the modulating angular frequency Ω_z, which in this case mimicked the gyroscope rotation rate.

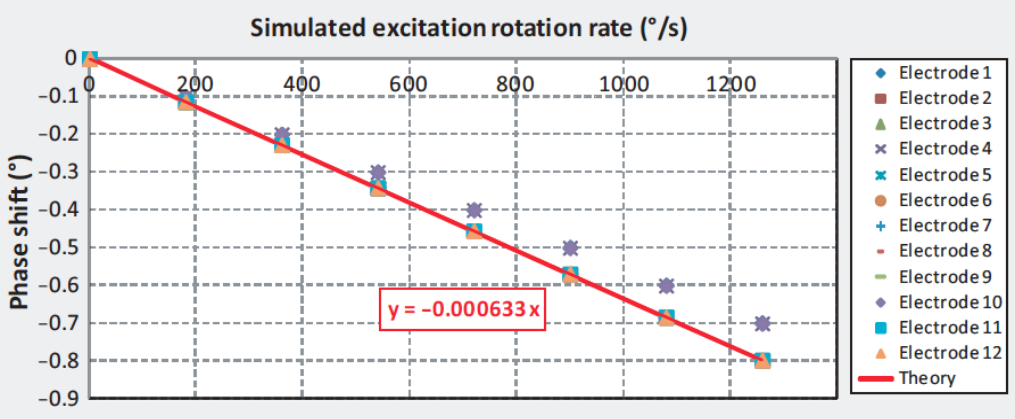

Figure 6-11 – Simulated phase shift in the BAW disk gyro response due to a rotating excitation, measured relative to its value at zero rotation rate. The solid line shows the theoretical analysis predictions.

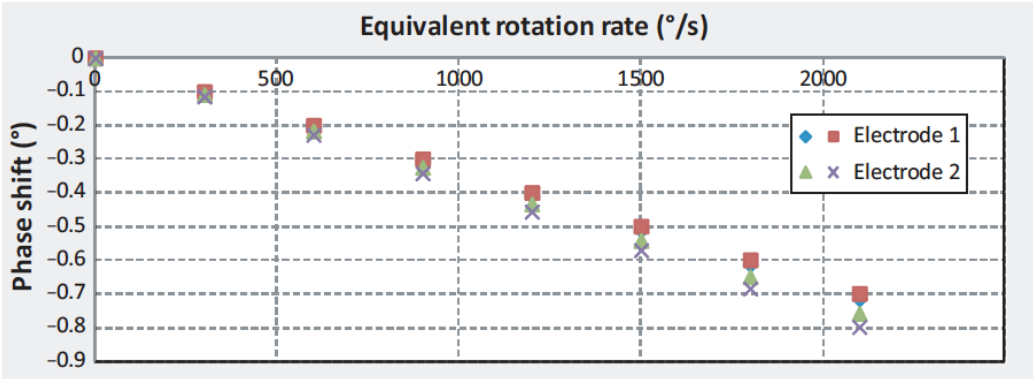

Figure 6-12 – Comparison of the phase shifts in the gyroscope response due to the Coriolis force and a rotating excitation. The angular velocity of the rotating excitation has been rescaled by a factor of $(1/\lambda)$ with respect to Fig. 6-11.

Figure 6-11 shows the changes in the phases of the electrode currents relative to their values at $\Omega_z = 0$, as well as the theoretical relationship given in (6-14) (solid line). It should be kept in mind that the phase shifts at the same value of Ω_z differ by a factor of λ. When this factor is accounted for, the plots in the two figures coincide, as shown in Fig. 6-12, confirming the relationship predicted from the phase shift created by a rotating excitation.

6.7. Measurement of Phase-Shift Calibration Scheme

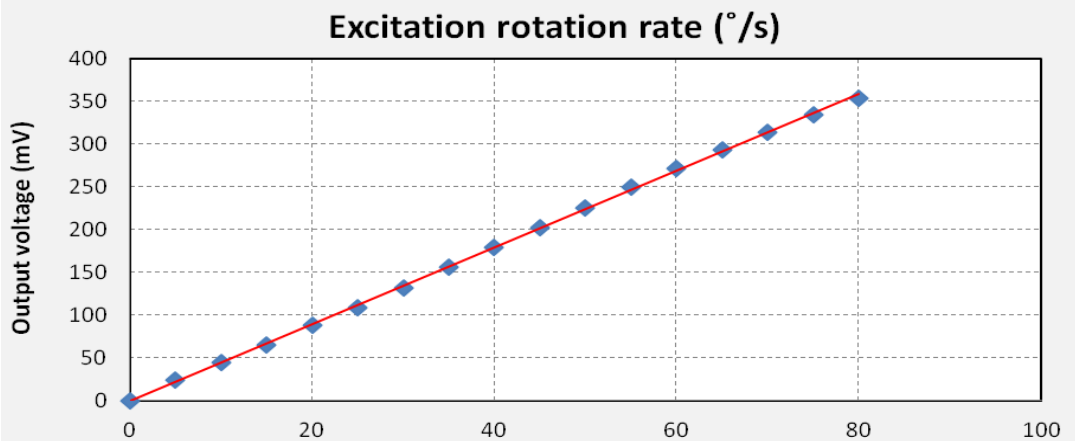

Figure 6-13 – Measured phase shift in the BAW gyroscope response due to a rotating excitation, relative to its value at zero rotation rate. The solid line shows the best linear fit to the data.

Following simulation, analysis of the gyroscope phase-shift response to a rotating excitation was performed through experimental measurement. For this purpose, a low-frequency sinusoidal signal was applied to the phase shifter to generate in-phase and quadrature (90° out of phase) components. Both signals were independently mixed with a sinusoidal signal operating at the resonance frequency of the gyroscope to create the amplitude-modulated excitation sinusoids used to excite the I and Q drive electrodes, according to the expressions in (6-9). The output signal of each mode was again amplified along independent channels, but this time each was passed through a second demodulating stage that was needed to remove the $2\omega_0$ component created by the first

demodulating stage. The corresponding measured phase shifts in the BAW gyroscope response are shown in Fig. 6-13. Here, the data points are again aligned fairly closely along a straight line.

CHAPTER 7

CONCLUSIONS AND FUTURE DIRECTIONS

7.1. Contributions

In this dissertation, the design, implementation and characterization of both amplitude- and phase-based readout schemes were investigated. A summary of technical contributions made in this work is given below:

1. *Optimization of power and noise for rate- and navigation-grade gyroscopes*: Optimal regions of power and noise operation were split into one of two regions depending on the frequency of operation of the gyroscope, . For low frequency gyroscopes, the optimal region is defined by the flicker noise corner frequency, which can be minimized by increasing transistor size (or using PMOS input transistors to reduce K_f) and reducing process minimum feature length (increasing C_{ox}). With high frequency gyroscopes, the optimal region is defined by the corner between the thermal noise and the gain attenuation regions. With the optimal noise region defined, it was determine that noise and power could be optimized by cancelling any quadrature-induced signal offsets and increasing R_F to its maximum value. Through the use of this technique the noise of the gyroscope can be scaled down to navigation-grade performance levels while minimizing the power needed at the desired level of performance.

2. *Development of CMOS ASIC interface for BAW disk gyroscope:* A complete CMOS interfacing ASIC was developed in TSMC 0.18 μm that featured a single-ended drive loop and fully-differential sense channel, amplitude level control, and quadrature cancellation. The ASIC operated with a power consumption of 1.6 mW, well below the power reported for most commercial gyroscopes. The quadrature cancellation technique was shown in measurement to reduce the quadrature component of the input sense current, improving the gain of the TIA and increasing the voltage of the rate signal by 4X. However, the noise and gain attenuation introduced by the signal path showed a measured noise increase of ~5X from 1.74 pA/√Hz to 9.36 pA/√Hz, suggesting that a buffer should be added between the cancellation circuitry and the input sense amplifier to preserve superior noise performance and low minimum levels of detection. Through rate testing, a scale factor of 1.15 mV/°/s was measured for the sensor with a bias drift of 0.095°/s, suggesting that the sensor is capable of providing rate grade performance. This ASIC represents the first comprehensive sensor interface for the BAW disk gyroscope, expanding upon the simplified design presented in [34].

3. *Implementation of the high frequency BAW disk gyroscope as a timing device*: It was suggested in this thesis that the BAW disk gyroscope has the distinct capability of providing both high-performance timing and rate sensing functionality. To support this assertion, the drive loop was locked into oscillation at f_0=9.65 MHz with a peak to peak voltage of ~700 mV_{PP} and 4.18% amplitude variation. The oscillator was shown to have a phase noise of ~-104 dBc at 1kHz from carrier, comparable to the state-of-the-art which are used as timing elements

only. Additionally, the oscillator is found to have a TCF of ~-27 ppm/°C, similar to what is expected for an uncompensated silicon device.

4. *Design of charge pumps for on-chip DC voltage generation for MEMS devices*: This dissertation introduced and explored the use of CMOS charge pumps in providing DC polarization and tuning voltages for MEMS gyroscopes or other capacitive devices. An outline of the advantages of high-DC voltage generators and the drawbacks of large DC ripple to MEMS device performance were presented, followed by an analysis and comparison of several pump design techniques including gate-voltage boosting, charge transfer switching, and clock doubling. Closed-loop charge pump techniques were also presented for maintaining level control on the pump output voltage, and the components needed to design the closed loop scheme were identified and simulated in Cadence. Finally, a strategy was presented to maximize the output DC voltage provided to a MEMS capacitive device using separate positive and negative charge pumps. Although the positive charge pump was able to provide a positive DC charge pump voltage of $13V$, the negative pump showed no significant voltage generation due to activation of the parasitic diode between the *n*-well and *p*-substrate. This issue can be fixed after modifying the layout of the negative charge pump, creating a system that can sustain large DC voltage generation for capacitive device as CMOS process sizes are reduced from 0.18 μm to 90 nm and beyond.

5. *Implementation of phase-shift readout scheme for rotation readout of 2-DOF mass-spring gyroscopes:* A new scheme was introduced for measuring the Coriolis excitation of the gyroscope in which identical signals 90° out-of-phase

with one another were used to excite the complementary modes of the gyroscope and measure a linear change in the phase-shift of the Coriolis signal rather than the signal amplitude. Equations modeling the drive forces and sense amplitudes were derived, and simulations were run to show the linear response of the phase readout scheme to any change in the input excitation of the gyroscope. A discrete phase readout ASIC was designed and fabricated onto a PCB, after which measurements were performed for both high frequency BAW gyroscopes and low frequency TFGs. For the BAW gyroscope, measurements of the phase readout showed a scale factor of 0.112 mV/°/s and a bias instability of 0.839 °/s, while and amplitude readout architecture designed with the same gain and BW as the phase readout system showed a scale factor of 0.043 mV/°/s and a bias instability of 0.334 °/s, indicating comparable performance from the two readout schemes. Performance tradeoffs between the phase readout scheme and amplitude scheme were analyzed to identify possible design challenges and bottlenecks in the monolithic integration of a phase readout sensor, after which it was concluded that the phase-shift scheme could be monolithically integrated at or near the same power consumption as the amplitude readout scheme.

6. *Modification of phase-shift scheme for calibration of 2-DOF mass-spring gyroscopes:* Following discussion of the phase-shift readout scheme, an overview of a calibration technique was presented that could track the variation of the readout scale factor over time. In this scheme, a rotating excitation was applied to the *I*- and *Q*-drive inputs while the gyroscope was held at zero rotation. It was shown in simulation that the rotating excitation only differed from the readout

scheme by a constant factor λ, the index of the resonance mode of the gyroscope. Measurement results also show a linear change in the DC output voltage as the rotating excitation is increased. Using this scheme, it is possible to track the variation of the readout scale factor over time, allowing on-demand calibration of rate- and navigation-grade gyroscopes without the need for an external rotary stage.

7.2. Future Directions

Additions and modifications to the BAW interface circuitry must still be made if the gyroscope is to remain competitive with the state-of-the-art gyroscopes commercially available today. In this chapter, some of the main tasks are outlined and briefly discussed.

7.2.1. 3-Axis and IMU Implementation of Navigation-Grade BAW ASIC

The ASIC presented in this thesis is designed to interface and readout a single-axis high-frequency gyroscope. However, state-of-the-art (SoA) gyroscopes and IMUs offer 3-axis sensing for any and all commercial needs. Therefore, a 3-axis ASIC must be developed (along with a 3-axis gyroscope) to compete with other commercial designs.

Before beginning 3-axis design, focus should be placed on developing a navigation-grade single-axis gyroscope solution (ASIC + device). The following assumptions are made about the design: (1) it is possible to fabricate a BAW disk that generates 60 nA/°/s Coriolis current (based on ANSYS simulations), (2) a 1.2V CMOS ASIC will be used to interface with the device, and (3) the quadrature of the ASIC has been cancelled or reduced significantly. Based on these assumptions and the design criteria for navigation-

grade gyroscopes described in Table 1-2 (Full-Scale Range: 400 °/s, Bias Drift: 0.01 °/hr), the input referred current noise and R_F of the sense TIA can be calculated.

The input referred current noise can be calculated by scaling the sensitivity of the gyroscope down for 0.01 °/hr, which yields

$$\begin{aligned} i_{n,in-NAV} &= \left(60\frac{nA/\sqrt{Hz}}{°/s}\right)\left(\frac{1}{3600}\frac{°/s}{°/hr}\right)(0.01°/hr) \\ &= 166.7\frac{fA}{\sqrt{Hz}} \end{aligned} \tag{7-1}$$

This solution will be reduced to 100fA/√Hz to simplify calculations and account for any small non-linearities in the system. R_F can be calculated by assuming rail-to-rail operation at the maximum full-scale range

$$\begin{aligned} R_F &= \left(\frac{V_{out-MAX}}{\left(60\frac{nA}{°/s}\right)(400°/s)}\right)\left(\frac{1.2}{24000}\frac{V}{nA}\right) \\ &= 50000\,\Omega \end{aligned} \tag{7-2}$$

Substituting (7-1) and (7-2) into (4-2) yields an estimated ASIC transconductance of

$$\begin{aligned} g_m &= \left(\frac{8kT}{3i_{n,in-NAV}^2 R_F^2}\right)\left(\frac{3.2\times10^{-20}}{3\left(100\times10^{-15}\right)^2\left(50\times10^3\right)^2}\right) \\ &\approx 427\,\mu S \end{aligned} \tag{7-3}$$

Assuming $g_m \approx \sqrt{I_D}$, the estimated current required for such an TIA is 20.66 mA.

If lower power consumption is desired over dynamic range, the TIA can also be re-designed using the same calculations. Assuming that only a FSR of 10 °/s, (7-2) can be rewritten as

$$R_F = \left(\frac{V_{out-MAX}}{\left(60 \frac{nA}{°/s} \right)(10°/s)} \right) \left(\frac{1.2}{24000} \frac{V}{nA} \right) = 2\,M\Omega \tag{7-4}$$

which provides a 40X increase in the maximum feedback resistance of the TIA. Because I_D is proportional to R_F, a 40X increase in resistance results in a 40X reduction in current consumption, and the current needed by the TIA now reduces to 516.6 μA.

Converting a single-axis ASIC into a 3-axis implementation is fairly simple – up to 3 copies of the single-axis ASIC are needed (depending on how the device integration is done). However, in order to design an ASIC that conforms with the strict power and noise requirements of SoA gyroscopes requires integrating the 3 systems together to include cross-sensitivity suppression, power minimization, noise optimization, and size reduction. Techniques such as multiplexing of the sense channel should be considered to reduce the overall power budget of the chip, while new architectures for level control and quadrature cancellation will add to the overall sophistication of the next-generation circuit architecture.

Once a 3-axis design is implemented, efforts should be focused on developing an IMU (3-axis gyroscope + 3-axis accelerometer) for full inertial sensing and dead reckoning applications. Although initially it may be best to simply incorporate both systems in the same package using mutually independent AXL and gyro ICs, work should also begin using sensor fusion, in which the data collected by the gyroscope ASIC is used to clean the signal of the AXL, and visa versa.

7.2.2. Implementation of Automatic Mode-Matching and Automatic Quadrature Cancellation Algorithms for BAW Gyroscopes

Because the sensitivity and dynamic range of the sensor is significantly dependent upon the separation of the drive and sense modes along with the magnitude of the quadrature component of the gyroscope, quadrature cancellation and mode-matching are necessary to obtain the best system performance in terms of resolution and range. However, the magnitude of the quadrature signal as well as the separation of the drive and sense peaks may change if environmental or non-environmental variations cause the gyroscope to drift. In such a case, it is important to have on-chip calibration materials that can both match the modes of the gyroscope and reduce the quadrature signal to its minimum while the sensor remains in operation. Earlier schemes have been presented for lower frequency gyroscopes, but the BAW may require additional circuit sophistication in order to get these algorithms to operate at its resonance frequency.

7.2.3. Digitization of Sense Output

Digitization of the gyroscope output signal opens the door for signal processing of the signal, which can assist through digital filtering/calibration in reducing the presence of unwanted noise in the gyroscope, thus improving performance markers such as bias instability and ARW. However, the digitization process can itself be noisy, and is therefore best if performed as early along the analog chain to offer the cleanest signal after digitization. Therefore, it is necessary to identify the best location to perform A-D conversion along with determine which ADCs (SAR, ΣΔ, etc) are needed to sample the sense Coriolis signal at such a high frequency.

7.2.4. On-chip Implementation of Phase Readout/Calibration Scheme

Although the phase readout and calibration schemes have shown to offer comparable performance to traditional amplitude-based measurement schemes, the system cannot be fully characterized until monolithic integration has been performed. However, there are two challenges to the on-chip implementation that need to be addressed. First, in the traditional amplitude readout IC, only a single set of electrically identical drive electrodes are actuated for self-oscillation. In the phase scheme, the two modes of the gyroscope must be operated simultaneously, using an architecture designed to ensure that the *I* mode and the *Q* mode have identical signals with 90° phase separation. One possible solution involves the use of a PLL to lock into the resonance frequency of the gyroscope, upconvert the signal to $4f_0$, and then downconvert the signal back to f_0 using flip-flops to generate 4 identical signals with 90° phase difference from one another. It may also be possible to lock into two identical electrodes (positive/negative) of the same mode (drive/sense) using a feedback TIA design. Secondly, it is necessary that low frequency signals (and filters with low cutoff frequencies) can be generated on-chip when the system is switched from readout mode to calibration mode (<100 Hz for BAW, <1 Hz for TFG). Should the filtering be too high, the phase calibration will be unable to read the DC change in θ_0 when the sinusoidal excitation is applied to the drive *I* and *Q* inputs. Additionally, if lower frequencies cannot be generated at the drive inputs, the scale factor of θ_0 may not be linear. It is possible to generate low frequency signals using flip-flops and g_m-*C* filters, but there could be an area cost associated if either strategy is implemented.

APPENDIX A

DERIVATION OF DRIVE AMPLITUDE, CORIOLIS AMPLITUDE, AND ENEΩ

Consider the gyroscope to be a coupled resonator system in which the sense mode is linked to the drive mode through rotation-induced Coriolis acceleration [105, 106]. Each resonator can be represented using a damped mass-spring model, which under Newton's 2nd law of motion can be written as (Equation A-1):

$$F_{Drive}(t) = M\frac{\partial^2 x}{\partial t^2} + D_x\frac{\partial x}{\partial t} + k_x x \tag{A-1}$$

for the drive mode, and

$$F_{Sense}(t) = M\frac{\partial^2 y}{\partial t^2} + D_y\frac{\partial y}{\partial t} + k_y y \tag{A-2}$$

for the sense mode. It should be noted here that because (A-1) and (A-2) are identical, the derivations in Appendix A.1 can also be applied to the y-axis, and will be referred to later in Appendix A.2 for such a purpose.

A.1 Drive Amplitude

To solve for the drive amplitude of the gyroscope, a Laplace transform is applied to (A-1), giving

$$F_{Drive}(s) = \left(Ms^2 + D_x s + k_x\right)X(s) \tag{A-3}$$

where M, D, k, and x represent the mass, damping force, spring constant, and displacement of the drive mode, respectively. Equation (A-2) can be rewritten as

$$\frac{X(s)}{F_{Drive}(s)} = \frac{1}{M}\frac{1}{s^2 + 2\xi_d\omega_{n_d}s + \omega_{n_d}^2} \tag{A-4}$$

where $\omega_n = \sqrt{\frac{k_x}{M}}$, $\xi_d = \frac{D}{2\sqrt{k_x M}}$, and $Q_d = \frac{1}{2\xi_d}$. Solving for the magnitude of (A-4) gives:

$$\left|\frac{X(j\omega)}{F_{Drive}(j\omega)}\right| = \frac{1/M\omega_{n_d}^2}{\left(1 - \frac{\omega^2}{\omega_{n_d}^2}\right)^2 + \left(2\xi_d\frac{\omega_{n_d}}{\omega}\right)^2} = \frac{Q}{M\omega_{n_d}^2} \tag{A-5}$$

In addition to being a function of displacement, the force of the drive mode F_{drive} can also be defined as a function of the charge on the disk, given by

$$F_{Drive} = (V_d - V_P)^2\frac{\partial C}{\partial x} \tag{A-6}$$

where

$$V_d = v_{ac}\sin(\omega t) \tag{A-7}$$

$$\frac{\partial C}{\partial x} = \frac{\varepsilon A}{(x - g_0)^2} \tag{A-8}$$

V_d and V_P represent the input drive and DC polarization voltages, respectively, and $\frac{\partial C}{\partial x}$ denotes the changing distance between parallel plates of a capacitor. If a Taylor series expansion of (A-7) is implemented and we make the assumption $x << g_0$, it can be reduced to:

$$\frac{\partial C}{\partial x} = \frac{\varepsilon A}{g_0^2} + \frac{2\varepsilon A}{g_0^3}x + \frac{3\varepsilon A}{g_0^4}x^2 + \ldots = \frac{\varepsilon A}{g_0^2} = \frac{C_0}{g_0} \tag{A-9}$$

where C_0 is the rest capacitance and g_0 is the rest gap distance between the parallel plates. By combining Equations (A-3) and (A-5), the drive displacement $x(t)$ is determined to be:

$$x(t) = \frac{Q_d C_0}{2M\omega_{n_d}^2 g_0}\left(V_P^2 - 2v_{ac}V_P \sin(\omega_{n_d} t)\right) \tag{A-10}$$

where Q_d, ω_d, and v_{ac} are the drive mode quality factor, drive mode resonance frequency, and AC drive voltage, respectively. The V_P^2 term of Equation A-10 remains constant and does not vary with time, meaning that the vibration amplitude of the drive signal becomes:

$$x(t) = -\frac{Q_d C_0}{M\omega_{n_d}^2 g_0} v_{ac}V_P \sin(\omega_{n_d} t) \tag{A-11}$$

A.2 Coriolis Signal

As described earlier, the sense mode displacement is coupled to the drive mode through the application of a Coriolis-induced acceleration. As a result, the applied force in the sense direction can be equated to:

$$F_{Drive} = -2M\vec{\Omega}_z \times v_{Drive} = -2M\vec{\Omega}_z \times \frac{\partial x}{\partial t} \tag{A-12}$$

Combining Equations (A-5), (A-6), and (A-10), the y-axis Coriolis-induced displacement is calculated to be:

$$y(t) = \frac{Q_s}{M\omega_{n_s}^2}\left(2M\vec{\Omega}_z\right)\frac{v_{ac}V_P Q_d C_0}{M\omega_{n_d}^2 g_0}\left(\omega_{n_d}\cos(\omega_{n_d}t)\right) \tag{A-13}$$

Which, after assuming mode-matched operation ($\omega_d^2 = \omega_s^2 = \omega_0^2$, $Q_d^2 = Q_s^2 = Q_{eff}^2$), reduces to:

$$y(t) = \frac{2v_{ac}V_P Q_{eff}^2 C_0 \vec{\Omega}_z}{M\omega_0^3 g_0}\cos(\omega_0 t) \tag{A-14}$$

where V_P, Q_{eff}, C_0, M, ω_0, and g_0 are constant.

A.3 Electrical Noise Equivalent of Rotation (ENEΩ)

The BAW gyroscope is a capacitive resonator; therefore, the output current at the sense amplifier can be measured as a change in capacitance, given by:

$$I_S(t) = \left(V_P - V_S\right)\frac{\partial C}{\partial t} \tag{A-15}$$

where V_s is the voltage at the sense electrode. Equation A-15 can be re-written as:

$$I_S(t) = \left(V_P - V_S\right)\frac{\partial C}{\partial y}\frac{\partial y}{\partial t} \tag{A-16}$$

If the capacitor created by the sense electrode and the gyroscope can be modeled as a parallel plate, then $\frac{\partial C}{\partial t}$ becomes $\frac{C_0}{g_0}$ as discussed in (A-9). With this in mind and assuming that $V_s = 0$, I_S becomes:

$$I_S(t) = V_P\frac{C_0}{g_0}\frac{\partial y}{\partial t} \tag{A-17}$$

Combining (A-14) and (A-17) then gives:

$$I_S(t) = \frac{-2v_{ac}V_P^2 C_0^2 Q_{eff}^2}{M\omega_0^2 g_0^2}\vec{\Omega}_z\sin(\omega_0 t) \tag{A-18}$$

The minimum detectable signal of the IC is defined as the smallest signal that can be distinguished from the input noise floor of the circuit. Therefore, to solve for ENEΩ, I_s is replaced by $I_{noise}\sqrt{(BW)}$. Solving for Ω_z, (A-18) becomes:

$$ENE\Omega_z = \frac{M\omega_0^2 g_0^2}{2v_{ac}V_P^2 C_0^2 Q_{eff}^2} i_{noise}\sqrt{BW} \qquad \text{(A-19)}$$

APPENDIX B

ALLAN VARIANCE

Allan variance (AVAR) is a statistical measurement used to characterize and identify noise-related error sources and their contribution to the overall noise statistics. It was developed in 1966 to characterize the phase and frequency instability of precision oscillators by representing RMS random drift error as a function of averaging time [107]. Until that time, the drift of these systems was specified in terms of a single RMS number was inadequate for predicting system performance, particularly due to the inherent deviation of the clock signal over time due to non-white noise sources of error such as flicker noise. Frequency domain analysis (i.e. autocorrelation and PSD) proved effective in determining the sources of error and evaluating performance, but the results proved difficult to interpret or understand. Today, Allan variance is widely used to characterize the underlying processes that are responsible for noise in clocks or clocked systems, such as amplifiers and sensors, particularly in inertial sensors such as gyroscopes and accelerometers [15].

B.1 Calculating Allan Variance

The Allan variance $\sigma^2(\tau)$ is formally defined in Equation B-1 as [107]

$$\sigma^2(\tau) = \frac{1}{2(n-1)} \sum_{i=1} \left(y(\tau)_{i+1} - y(\tau)_i \right)^2 \qquad \text{(B-1)}$$

where τ is the averaging time, y_i is the average value of the measurement in bin i, and n is the total number of bins. Its calculation is based on the repeated averaging of the

collected data over several different clusters (bins) through a process known as cluster analysis (binning), which is described in further detail in the steps listed below [40].

B.1.1 Data Collection

In this step, output data from the device under test (DUT) is sampled at a fixed interval τ_0 over a given period of time. Typically the data is collected through an external measurement tool such as a multimeter, oscilloscope, or computer. A high sampling rate (f_s) is necessary for clustering several bins across a small time-span for quantization noise and angle random walk (ARW) computation, while a long collection time (on the order of several hours) allows measurement of rate ramp and rate random walk (RRW).

B.1.2 Data Clustering

During data clustering, the data (consisting of N points) is divided into τ = 1,2,..,n clusters of M samples/cluster based on an averaging time τ. This τ will be a multiple of the initial sampling interval, τ_0.

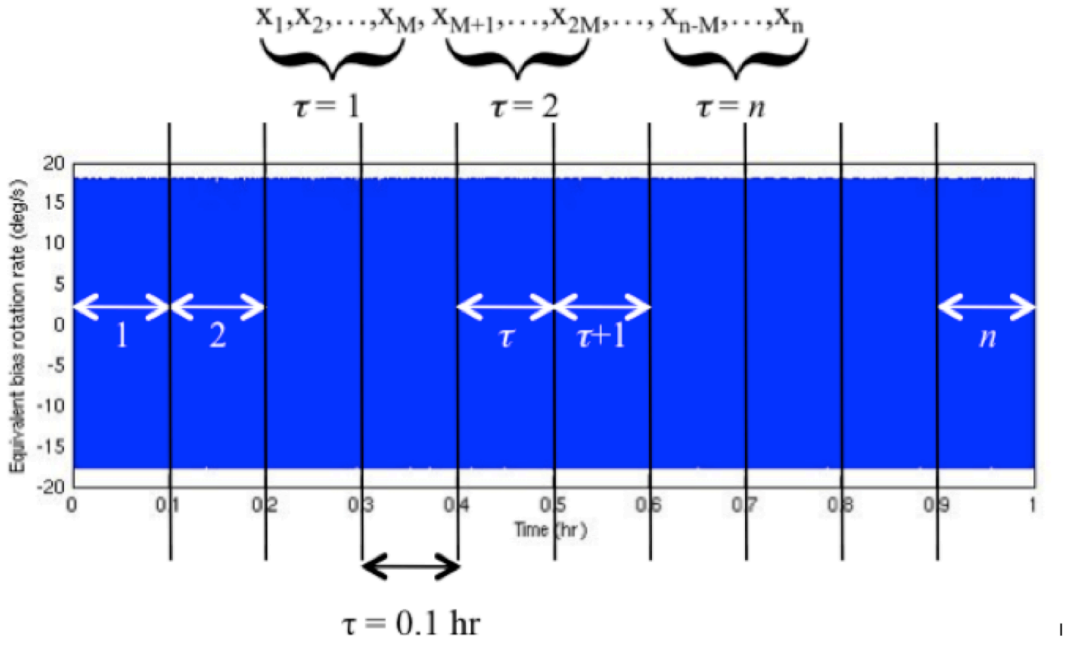

Figure B-1 – Data clustering of sampled data

B.1.3 Data Averaging

After data clustering, the data in each cluster is averaged over the length of the cluster τ. This average may be expressed as:

$$y(\tau) = \frac{1}{M} \sum_{i=1}^{M} x_{(\tau-1)M+i} \tag{B-2}$$

where x represents the dataset contained within each cluster. Data processing software (MATLAB, C++, etc.) is used to collect data from external equipment, process the data, and calculate the mean of each cluster, and can also be used to for calculating and plotting the Allan variance. The MATLAB code used in this thesis for calculating the gyroscope AVAR is shown in Section B.3 of this Appendix.

B.1.4 Computing Variance

During the computing step, the difference in average between successive clusters is first squared and summed together, after which it is divided by the rescaling factor. The square root of the result gives the Allan deviation or root Allan variance, a quantitative measure of how much the average changed at that particular value of averaging time.

B.1.5 Repeated Averaging

In the final step, τ is changed and Steps 1 through 4 are repeated until several time clusters have been averaged and their Allan deviations computed. The AVAR calculations are then plotted against τ to identify the major sources of error of the system.

B.2 Sources of Error

As stated earlier, the computation of non-white noise sources of error can be also performed through frequency domain analysis by calculation of the power spectral density (PSD) of the collected data, given by

$$\sigma^2(\tau) = 4\int_0^\infty S_\Omega(f)\frac{\sin^4(\pi f \tau)}{(\pi f \tau)^2} \qquad \text{(B-3)}$$

Here, τ represents the clustered correlation time, and $S_\omega(f)$ is the PSD of the system output. This can be interpreted as the Allan variance being directly proportional to the output noise power of the DUT when the output is passed through a filter with a transfer function $\frac{\sin^4(\pi f \tau)}{(\pi f \tau)^2}$, which arises due to the nature of cluster analysis [40]. The filter bandwidth depends on the sampling time τ. By varying τ, different types of random processes (and therefore different properties associated with the noise) can be studied.

A typical Allan variance curve is shown in Fig. B-2 below:

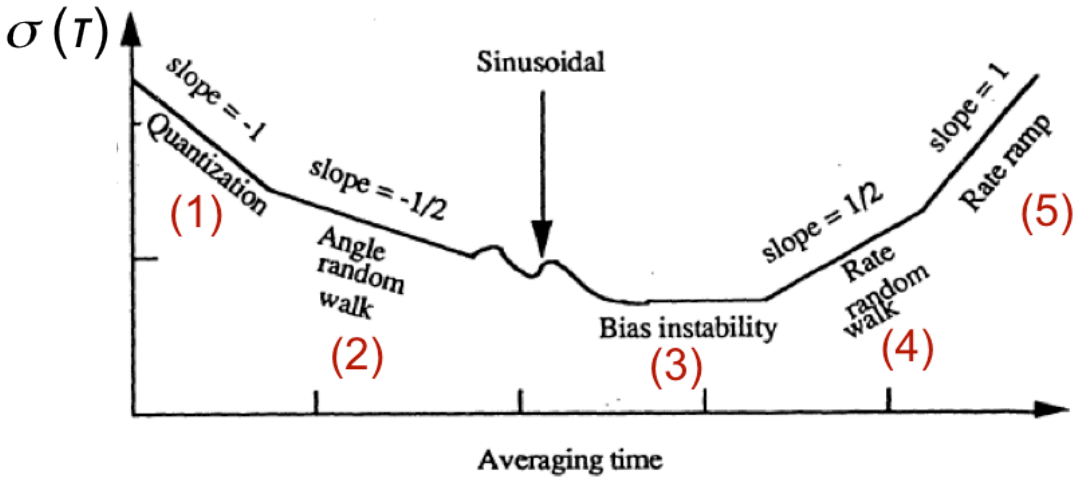

Figure B-2 – Allan variance plot showing major sources of error

The time domain data contains contributions from different noise terms that have been computed across different averaging times (τ). It is seen in Fig. B-2 that there are several distinct regions in the Allan variance curve, which correspond to the following noise terms [40, 108]:

1. Quantization Noise (Q)
2. Angle Random Walk (ARW)

3. Bias Instability
4. Rate Random Walk (RRW)
5. Rate Ramp (RR)

Because sinusoidal noise seen in the Allan variance plot is typically characterized by several distinct frequencies and generated from periodic environmental changes, it is better identified through a PSD plot than through Allan variance computation [15].

Excluding sinusoidal noise, the remaining 5 terms correspond to different portions on the Allan variance curve that can be identified by their slope. Additional components of noise that can be measured through Allan variance are provided in [16]. The processes that contribute to these noise terms are uncorrelated, meaning that the total Allan variance at a given τ can be determined from summing the magnitude of each of the noise components at τ, given by

$$\sigma^2(\tau) = \sigma_Q^2(\tau) + \sigma_{ARW}^2(\tau) + \sigma_{Bias}^2(\tau) + \sigma_{Sine}^2(\tau) + \sigma_{RRW}^2(\tau) + \sigma_{RR}^2(\tau) \qquad \text{(B-4)}$$

The relationship between noise and slope can also be expressed in the frequency domain by equating Equations B-1 and B-2. From this we can see that the slope of the different noise sources can also be expressed as different powers of τ.

B.2.1 Quantization Noise

Quantization noise represents the minimum resolution of the sensor; it is strictly due to the discrete/quantized sampling at the amplifier or sensor output to record the value of the bias over time [108]. Since sampling occurs is at a higher frequency than other system time constants in the time domain, this noise term corresponds to small values of τ.

The PSD of quantization noise is calculated to be (B-4), with a root Allan variance expression given by (B-5)

$$S_Q(f) = \frac{4Q_N^2}{\tau}\sin^2(\pi f \tau) \quad \text{(B-5)}$$

$$\sigma_Q^2(\tau) = \frac{3Q_N^2}{\tau} \quad \text{(B-6)}$$

where Q_N denotes the quantization term coefficient. Quantization noise can be evaluated on any point in the Allan variance plot as the portion of the curve with a slope of -1 (proportional to τ^{-2} when plotted on a log-log scale.

B.2.2 Angle Random Walk

Angle random walk (ARW) is a measure of angular error build-up over time that is due to white noise in angular rate [40]. This component is referred to as random walk because it is a non-stationary random process with a mean of zero and a mean-square error that grows linearly with time [40]. However, because ARW is a measure of white noise, the component corresponds to the flat region of the PSD plot, given by

$$S_{ARW}(f) = N^2 \quad \text{(B-7)}$$

where N represents the angle random walk coefficient. In an AVAR measurement, ARW is given by [108]

$$\sigma_{ARW}^2(\tau) = \frac{N^2}{\tau} \quad \text{(B-8)}$$

with a slope of -½ (proportional to τ^{-1}) on a log-log scale. The ARW coefficient N can be obtained directly by reading slope line where τ=1.

ARW is an important figure of merit in the characterization of inertial sensors, particularly gyroscopes. Not only does it track the contribution of white noise over time, but it can also describe any deviation or error that occurs when the rate signal is integrated for angular measurement [17].

B.2.3 Bias Instability

Typically, bias instability consists of the noise components subject to random flickering, such as *1/f* noise. The PSD and Allan variance components of this noise are given by [108]

$$S_{Bais}(f) = \begin{cases} \frac{B^2}{2\pi}\frac{1}{f}; \; f \le f_0 \\ \\ 0; \; f > f_0 \end{cases} \tag{B-9}$$

and

$$\sigma^2_{Bias}(\tau) = \left(\frac{B}{0.6648}\right)^2 \tag{B-10}$$

where B represents the bias instability coefficient. The root Allan variance curve for this noise is flat (zero-slope), representing the best achievable bias stability for the system. For gyroscopes, the value that corresponds to this minimum on the Allan variance curve is quoted as the bias drift of the sensor [17].

B.2.4 Rate Random Walk

Rate random walk represents the drift rate error build-up over time due to wideband acceleration due to white noise [40, 108]. The exact origins of rate random walk noise are unknown, but consist of exponentially correlated noise with long correlation times. The PSD associated with RRW is given by

$$S_{RRW}(f) = \left(\frac{K}{2\pi}\right)^2 \frac{1}{f^2} \tag{B-11}$$

where K represents the rate random walk coefficient. On the Allan variance plot, RRW is given by

$$\sigma^2_{RRW}(\tau) = \frac{K^2}{3}\tau \quad \text{(B-12)}$$

with a slope of ½ (proportional to τ) on a log-log scale.

B.2.5 Rate Ramp

Rate ramp is more of a deterministic error than a random noise component. Its presence in the Allan variance plot can indicate a very slow monotonic change in signal intensity that persists over a long period of time, usually several hours. It appears as a genuine input to the sensor, given by:

$$\omega(t) = Rt \quad \text{(B-13)}$$

where R represents the rate ramp coefficient. On an Allan variance plot, rate ramp is characterized by

$$\sigma^2_{RR}(\tau) = \frac{R^2\tau^2}{2} \quad \text{(B-14)}$$

with a slope of 1 (proportional to τ^2) on a log-log scale.

B.3 Allan Variance MATLAB Code

```
% This is the matlab to calculate the bias stability for XL device + IC
% file to simulate the TD response of the gyro using matlab and simulink
% this file aims to generate the Allan variance plot of the data collected.
% we use simulink to obtain the TD noise and then generate the Allan variance for the same.
% function [sig,sig2,osig,msig,tsig,tau]=avar(y,tau0)
% INPUTS:
%  y = signal
%  tau0 = sampling period (s)
%
% OUTPUTS:
% sig =  N samples STD DEV
% sig2 = Normal Allan STD DEV, 2 samples STD DEV.
% osig = Sigma(y)(tau) = Allan Standard Deviation with Overlapping estimate
% msig = Modified Allan Standard Deviation
% tsig = Time Allan Standard Deviation
% tau = measurement time (s).
```

```
%
clear all;
close all;
clc;

format long e;
%
s=[];
x=[];
sig2 = [];
tau = [];
%
tic
vavg = [];
vavg_mean = [];
zro1 = [];
zro = [];
data = [];
%
% perform the TD simulation and collect drifG:\9_6_board_2_driftt data over time.

load -ascii vdc.dat  %CHANGE THIS LINE WITH VARNAME
vp = vdc;            %CHANGE THIS LINE WITH VARNAME
load -ascii time.dat %CHANGE THIS LINE WITH VARNAME
time = time;         %CHANGE THIS LINE WITH VARNAME

tau0=time/length(vp);
fs=1/tau0;
%vavg_all = load('./vdc_set6.dat');

vavg=vp';

%
vavg_mean = vavg - mean(vavg);
time_hour=(1:length(vavg_mean))/(fs*3600);
%
%sens = 0.160000;     % sensitivity of gyroscope (V/deg/sec)
%
zro = vavg_mean./sens;
y=zro;
%
n=length(y);
jj=floor( log((n-1)/3)/log(2) );
%tau0 = 0.43;

%
```

```
figure
subplot(2,1,1);plot(time_hour,vavg_mean);
hold on;
grid on;
xlabel('Time (hr)');
ylabel('Normalized bias voltage (V)');
title('Navigational Grade TFG Bias Drift Measurement (@RT)')
subplot(2,1,2);plot(time_hour,y);
hold on;
grid on;
xlabel('Time (hr)');
ylabel('Equivalent bias rotation rate (deg/s)');
%
for j=0:jj
  fprintf('.');
  m=2^j;
  tau(j+1)=m*tau0;
  D=zeros(1,n-m+1);
  for i=1:n-m+1
     D(i)=sum(y(i:i+m-1))/m;
  end
  %N sample
  sig(j+1)=std(D(1:m:n-m+1));

%AVAR
  sig2(j+1)=sqrt(0.5*mean((diff(D(1:m:n-m+1)).^2)));

 %OVERAVAR
  z1=D(m+1:n+1-m);
  z2=D(1:n+1-2*m);
  u=sum((z1-z2).^2);
  osig(j+1)=sqrt(u/(n+1-2*m)/2);

  %MVAR
  u=zeros(1,n+2-3*m);
  for L=0:n+1-3*m
     z1=D(1+L:m+L);
     z2=D(1+m+L:2*m+L);
     u(L+1)=(sum(z2-z1))^2;
  end
 %
  uu=mean(u);
  msig(j+1)=sqrt(uu/2)/m;
 %
  %TVAR
  tsig(j+1)=tau(j+1)*msig(j+1)/sqrt(3);
```

```
end

% CREATE PLOTS

 figure(2);

 semilogx(tau,sig2*3600,'b.-');
 xlabel('\tau (s)');
 ylabel('deg/hr');
 title('Navigational Grade TFG Bias Drift Measurement (@RT)');
 grid on;

 toc
 min(sig2(1:length(tau))*3600)  %Print lowest point (Bias Drift)
```

REFERENCES

[1] N. Yazdi, F. Ayazi, and K. Najafi, "Micromachined inertial sensors," *Proceedings of the IEEE,* vol. 86, pp. 1640-1659, 1998.

[2] M. F. Zaman, A. Sharma, and F. Ayazi, "The Resonating Star Gyroscope: A Novel Multiple-Shell Silicon Gyroscope With Sub-5 deg/hr Allan Deviation Bias Instability," *Sensors Journal, IEEE,* vol. 9, pp. 616-624, 2009.

[3] *Status of the MEMS Industry 2010* [Online]. Available: http://www.sensortips.com/category/hot-topic/market-research. Accessed January 2012.

[4] M. J. Dalal, J. L. Fu, and F. Ayazi, "Simultaneous dual-mode excitation of piezo-on-silicon micromechanical oscillator for self-temperature sensing," in *Micro Electro Mechanical Systems (MEMS), 2011 IEEE 24th International Conference on*, 2011, pp. 489-492.

[5] H. Johari and F. Ayazi, "Capacitive Bulk Acoustic Wave Silicon Disk Gyroscopes," in *Electron Devices Meeting, 2006. IEDM '06. International*, 2006, pp. 1-4.

[6] I. P. Prikhodko, S. A. Zotov, A. A. Trusov, and A. M. Shkel, "Foucault pendulum on a chip: angle measuring silicon MEMS gyroscope," in *Micro Electro Mechanical Systems (MEMS), 2011 IEEE 24th International Conference on*, 2011, pp. 161-164.

[7] M. Zaman, "Degree-Per-Hour Mode-Matched Micromachined Silicon Vibratory Gyroscopes," Ph. D Dissertation, Electrical and Computer Engineering, Georgia Institute of Technology, Atlanta, GA, 2008.

[8] "MEMS motion sensor: 3 axis analog output gyroscope," ST Microelectronics, Geneva, Switzerland, Datasheet LYPR540AH, 2009.

[9] F. Ayazi and K. Najafi, "A HARPSS polysilicon vibrating ring gyroscope," *Journal of Microelectromechanical Systems,* vol. 10, pp. 169-179, 2001.

[10] J. A. Geen, S. J. Sherman, J. F. Chang, and S. R. Lewis, "Single-chip surface-micromachined integrated gyroscope with 50º/hour root allan variance," in *International Solid-State Circuits Conference (ISSCC)*, 2002, pp. 346-539.

[11] M. F. Zaman, A. Sharma, B. V. Amini, and F. Ayazi, "The Resonating Star Gyroscope," in *International Conference on Micro Electro Mechanical Systems (MEMS)*, 2005, pp. 355-358.

[12] F. Ayazi, "Multi-DOF inertial MEMS: From gaming to dead reckoning," in *Solid-State Sensors, Actuators and Microsystems Conference (TRANSDUCERS), 2011 16th International*, 2011, pp. 2805-2808.

[13] *IMU & High Performance Inertial MEMS* [Online]. Available: http://www.i-micronews.com/reports/IMU-High-Performance-Inertial-MEMS-2011/1/160/. Accessed January 2012.

[14] R. Neul, U. M. Gomez, K. Kehr, W. Bauer, J. Classen, C. Doring, E. Esch, S. Gotz, J. Hauer, B. Kuhlmann, C. Lang, M. Veith, and R. Willig, "Micromachined Angular Rate Sensors for Automotive Applications," *IEEE Sensors Journal,* vol. 7, pp. 302-309, 2007.

[15] W. Stockwell, "Bias Stability Measurement: Allan Variance," Milpitas, CA, 2004.

[16] "IEEE Standard Specification Format Guide and Test Procedure for Single-Axis Interferometric Fiber Optic Gyros," ed, 1998.

[17] W. Stockwell, "Angle Random Walk," Milpitas, CA.

[18] IEEE, "IEEE Standard for Inertial Sensor Terminology," ed, 2001.

[19] J. Raman, E. Cretu, P. Rombouts, and L. Weyten, "A Digitally Controlled MEMS Gyroscope With Unconstrained Sigma-Delta Force-Feedback Architecture," in *International Conference on Micro Electro Mechanical Systems (MEMS)*, 2006, pp. 710-713.

[20] S. J. Dixon-Warren. *Motion sensing in the iPhone 4: MEMS gyroscope* [Online]. Available: http://www.memsinvestorjournal.com/2011/01/motion-sensing-in-the-iphone-4-mems-gyroscope.html. Accessed January 2012.

[21] "MPU-6000 and MPU-6050 Product Specification, Revision 1.0," Invensense, Sunnyvale, CA, Datasheet MPU-60xx, 2010.

[22] "High Performance, Digital Output Gyroscope," Analog Devices, Inc., Norwood, MA, Datasheet ADXRS453, 2011.

[23] "Angular rate sensor for rollover applications," Bosch, Gerlingen, Germany, Datasheet SMG06x, 2011.

[24] "KGY13 Series - Gyroscopes," Kionix, Ithaca, NY, Datasheet KGY13x, 2011.

[25] H. Johari and F. Ayazi, "Silicon-On-Insulator Bulk Acoustic Wave Disk Resonators," in *IEEE International SOI Conference*, 2006, pp. 153-154.

[26] M. S. Weinberg and A. Kourepenis, "Error sources in in-plane silicon tuning-fork MEMS gyroscopes," *Microelectromechanical Systems, Journal of,* vol. 15, pp. 479-491, 2006.

[27] M. F. Zaman, A. Sharma, H. Zhili, and F. Ayazi, "A Mode-Matched Silicon-Yaw Tuning-Fork Gyroscope With Subdegree-Per-Hour Allan Deviation Bias Instability," *Journal of Microelectromechanical Systems,* vol. 17, pp. 1526-1536, 2008.

[28] Z. Hao, M. F. Zaman, A. Sharma, and F. Ayazi, "Energy Loss Mechanisms in a Bulk-Micromachined Tuning Fork Gyroscope," in *Sensors, 2006. 5th IEEE Conference on*, 2006, pp. 1333-1336.

[29] Y. Mochida, M. Tamura, and K. Ohwada, "A micromachined vibrating rate gyroscope with independent beams for the drive and detection modes," *Sensors and Actuators A: Physical,* vol. 80, pp. 170-178, March 2000.

[30] M. F. Zaman, A. Sharma, and F. Ayazi, "High Performance Matched-Mode Tuning Fork Gyroscope," in *Micro Electro Mechanical Systems, 2006. MEMS 2006 Istanbul. 19th IEEE International Conference on*, 2006, pp. 66-69.

[31] H. Johari and F. Ayazi, "High-frequency capacitive disk gyroscopes in (100) and (111) silicon," in *International Conference on Micro Electro Mechanical Systems (MEMS)*, 2007, pp. 47-50.

[32] D. Hopkin, C. P. Fell, K. Townsend, and T. R. Mason, "Vibrating Structure Gyroscope," U.S. Patent 5932804, August 1999.

[33] H. Johari, "Micromachined Capacitive Silicon Bulk Acoustic Wave Gyroscopes," Ph. D Dissertation, Electrical and Computer Engineering, Georgia Institute of Technology, Atlanta, GA, 2008.

[34] J. Shah, H. Johari, A. Sharma, and F. Ayazi, "CMOS ASIC for MHz silicon BAW gyroscope," in *International Symposium on Circuits and Systems (ISCAS)*, 2008, pp. 2458-2461.

[35] W. K. Sung, M. Dalal, and F. Ayazi, "A mode-matched 0.9 MHz single proof-mass dual-axis gyroscope," in *International Solid-State Sensors, Actuators and Microsystems Conference (TRANSDUCERS)*, 2011, pp. 2821-2824.

[36] H. Zhili and F. Ayazi, "Support loss in micromechanical disk resonators," in *International Conference on Micro Electro Mechanical Systems (MEMS)*, 2005, pp. 137-141.

[37] A. Sharma, M. F. Zaman, and F. Ayazi, "A Sub-0.2 °/hr Bias Drift Micromechanical Silicon Gyroscope With Automatic CMOS Mode-Matching," *IEEE Journal of Solid-State Circuits,* vol. 44, pp. 1593-1608, 2009.

[38] A. Sharma, M. F. Zaman, and F. Ayazi, "A Smart Angular Rate Sensor System," in *Sensors, 2007 IEEE*, 2007, pp. 1116-1119.

[39] C. D. Ezekwe and B. E. Boser, "A Mode-Matching ΔΣ Closed-Loop Vibratory Gyroscope Readout Interface With a 0.004 °/s/√Hz Noise Floor Over a 50 Hz Band," *IEEE J. Solid-State Circuits,* vol. 43, pp. 3039-3048, 2008.

[40] A. Sharma, "CMOS Systems and Circuits for Sub-Degree Per Hour MEMS Gyroscopes," Ph. D Dissertation, Electrical and Computer Engineering, Georgia Institute of Technology, Atlanta, GA, 2007.

[41] E. Tatar, S. E. Alper, and T. Akin, "Effect of quadrature error on the performance of a fully-decoupled MEMS gyroscope," in *International Conference on Micro Electro Mechanical Systems (MEMS)*, 2011, pp. 569-572.

[42] M. Saukoski, L. Aaltonen, and K. A. I. Halonen, "Zero-Rate Output and Quadrature Compensation in Vibratory MEMS Gyroscopes," *IEEE Sensors Journal,* vol. 7, pp. 1639-1652, 2007.

[43] S. Gunthner, M. Egretzberger, A. Kugi, K. Kapser, B. Hartmann, U. Schmid, and H. Seidel, "Compensation of parasitic effects for a silicon tuning fork gyroscope," *IEEE Sensors Journal,* vol. 6, pp. 596-604, 2006.

[44] V. P. Veiko, "Laser-Assisted Microshaping," *Proc. SPIE,* vol. 4157, pp. 93-104, August 2000 2000.

[45] D. Joachim and L. Liwei, "Selective polysilicon deposition for frequency tuning of MEMS resonators," in *International Conference on Micro Electro Mechanical Systems (MEMS)*, 2002, pp. 727-730.

[46] L. Aaltonen, A. Kalanti, M. Pulkkinen, M. Paavola, M. Kamarainen, and K. A. I. Halonen, "A 2.2 mA 4.3 mm2 ASIC for a 300 °/s 2-Axis Capacitive Micro-Gyroscope," *IEEE Journal of Solid-State Circuits,* vol. 46, pp. 1682-1692, 2011.

[47] J. Seeger, A. J. Rastegar, and M. T. Tormey, "Method and Apparatus for Electronic Cancellation of Quadrature Error," U.S. Patent 0180908, 2007.

[48] L. Prandi, C. Caminada, L. Coronato, G. Cazzaniga, F. Biganzoli, R. Antonello, and R. Oboe, "A low-power 3-axis digital-output MEMS gyroscope with single drive and multiplexed angular rate readout," in *International Solid-State Circuits Conference (ISSCC)*, 2011, pp. 104-106.

[49] S. Pourkamali, H. Zhili, and F. Ayazi, "VHF single crystal silicon capacitive elliptic bulk-mode disk resonators-part II: implementation and characterization," *Journal of Microelectromechanical Systems,* vol. 13, pp. 1054-1062, 2004.

[50] J. Danny, R. Ralf, Y. Yi, and F. Jorg, "Characterization and Modeling of Wire Bond Interconnects up to 100 GHz," in *IEEE Compound Semiconductor Integrated Circuit Symposium (CSIC)*, 2006, pp. 111-114.

[51] A. A. Seshia, M. Palaniapan, T. A. Roessig, R. T. Howe, R. W. Gooch, T. R. Schimert, and S. Montague, "A vacuum packaged surface micromachined resonant accelerometer," *Journal of Microelectromechanical Systems,* vol. 11, pp. 784-793, 2002.

[52] R. Tabrizian, M. Pardo, and F. Ayazi, "A 27 MHz temperature compensated MEMS oscillator with sub-ppm instability," in *International Conference on Micro Electro Mechanical Systems (MEMS)*, 2012, pp. 23-26.

[53] G. K. Ho, K. Sundaresan, S. Pourkamali, and F. Ayazi, "Micromechanical IBARs: Tunable High-Q Resonators for Temperature-Compensated Reference Oscillators," *Journal of Microelectromechanical Systems,* vol. 19, pp. 503-515, 2010.

[54] D. Murphy, M. P. Kennedy, J. Buckley, and Q. Min, "The optimum power conversion efficiency and associated gain of an LC CMOS oscillator," in *Circuits and Systems, 2006. ISCAS 2006. Proceedings. 2006 IEEE International Symposium on*, 2006, p. 4 pp.

[55] B. Razavi, *Design of Integrated Circuits for Optical Communications*: McGraw-Hill, 2003.

[56] D. B. Leeson, "A simple model of feedback oscillator noise spectrum," *Proc. IEEE,* vol. 54, pp. 329-330, 1966.

[57] V. Re, M. Manghisoni, L. Ratti, V. Speziali, and G. Traversi, "Survey of noise performances and scaling effects in deep submicrometer CMOS devices from different foundries," *Nuclear Science, IEEE Transactions on,* vol. 52, pp. 2733-2740, 2005.

[58] M. Manghisoni, L. Ratti, V. Re, V. Speziali, and G. Traversi, "Noise Performance of 0.13 μm CMOS Technologies for Detector Front-End Applications," *Nuclear Science, IEEE Transactions on,* vol. 53, pp. 2456-2462, 2006.

[59] M. Manghisoni, L. Ratti, V. Re, V. Speziali, and G. Traversi, "Noise Characterization of 130 nm and 90 nm CMOS Technologies for Analog Front-end

Electronics," in *Nuclear Science Symposium Conference Record, 2006. IEEE*, 2006, pp. 214-218.

[60] P. Allen and D. Holberg, *CMOS Analog Circuit Design*: Oxford University Press, 2002.

[61] B. Gilbert, "A precise four-quadrant multiplier with subnanosecond response," *Solid-State Circuits, IEEE Journal of,* vol. 3, pp. 365-373, 1968.

[62] J. Crols and M. S. J. Steyaert, "A 1.5 GHz highly linear CMOS downconversion mixer," *IEEE Journal of Solid-State Circuits,* vol. 30, pp. 736-742, 1995.

[63] R. J. Baker, *CMOS: Circuit Design, Layout, and Simulation*: IEEE Press, 2008.

[64] S. Maniktala, "Simple Switcher PCB Layout Guidelines," National Semiconductor, Santa Clara, CA, Application Note 1229, 2002.

[65] "High-Speed Board Designs," Altera, Duluth, GA, Application Note 75, 2001.

[66] "PCB Design Guidelines for Reduced EMI," Texas Instruments, Dallas, TX, Application Note SZZA009, 1999.

[67] "RF Design Guidelines: PCB Layout and Circuit Optimization," Semtech, Camarillo, CA, Application Note 1200.04, 2006.

[68] M. Gonzalez, A. Iourdain, B. Vandevelde, and H. A. C. Tilmans, "Effect of thermomechanical stress on resonant frequency shift of a silicon MEMS resonator," in *International Conference on Thermal, Mechanical and Multi-Physics Simulation and Experiments in Microelectronics and Micro-Systems (EuroSimE)*, 2008, pp. 1-5.

[69] M. Hossain, B. M. Frank, and Y. M. Antar, "Performance of a low voltage highly linear 24 GHz down conversion mixer in 0.18µm CMOS," in *Topical Meeting on Silicon Monolithic Integrated Circuits in RF Systems*, 2006, p. 4 pp.

[70] S. Rai and B. Otis, "A 1V 600μW 2.1GHz Quadrature VCO Using BAW Resonators," in *Solid-State Circuits Conference, 2007. ISSCC 2007. Digest of Technical Papers. IEEE International*, 2007, pp. 576-623.

[71] H. M. Lavasani, R. Abdolvand, and F. Ayazi, "A 500MHz Low Phase-Noise A1N-on-Silicon Reference Oscillator," in *CICC 2007*, 2007, pp. 599-602.

[72] F. Nabki and M. N. El-Gamal, "A high gain-bandwidth product transimpedance amplifier for MEMS-based oscillators," in *ESSCIRC 2008*, 2008, pp. 454-457.

[73] Z. Chengjie, J. Van der Spiegel, and G. Piazza, "1.05 GHz MEMS oscillator based on lateral-field-excited piezoelectric AlN resonators," in *IEEE International Frequency Control Symposium 2009*, 2009, pp. 381-384.

[74] H. J. Lee, K. K. Park, P. Cristman, O. Oralkan, M. Kupnik, and B. T. Khuri-Yakub, "A Low-Noise Oscillator based on a Multi-Membrane CMUT for High Sensitivity Resonant Chemical Sensors," in *MEMS 2009*, 2009, pp. 761-764.

[75] G. K. Ho, K. Sundaresan, S. Pourkamali, and F. Ayazi, "Temperature Compensated IBAR Reference Oscillators," in *MEMS 2006*, 2006, pp. 910-913.

[76] H. Wen-Lung, R. Zeying, L. Yu-Wei, C. Hsien-Yeh, J. Lahann, and C. T. C. Nguyen, "Fully monolithic CMOS nickel micromechanical resonator oscillator," in *MEMS 2008*, 2008, pp. 10-13.

[77] L. Yu-Wei, L. Seungbae, L. Sheng-Shian, X. Yuan, R. Zeying, and C. T. C. Nguyen, "60-MHz wine-glass micromechanical-disk reference oscillator," in *ISSCC 2004*, 2004, pp. 322-530 Vol.1.

[78] K. Bongsang, M. Akgul, L. Yang, L. Wei-Chang, R. Zeying, and C. T. C. Nguyen, "Acceleration sensitivity of small-gap capacitive micromechanical resonator oscillators," in *IEEE International Frequency Control Symposium (IFCS)*, 2010, pp. 273-278.

[79] J. S. Brugler, "Theoretical performance of voltage multiplier circuits," *IEEE Journal of Solid-State Circuits,* vol. 6, pp. 132-135, 1971.

[80] A. K. Samarao, G. Casinovi, and F. Ayazi, "Passive TCF compensation in high Q silicon micromechanical resonators," in *International Conference on Micro Electro Mechanical Systems (MEMS)*, 2010, pp. 116-119.

[81] K. Bult, "Analog design in deep sub-micron CMOS," in *European Solid-State Circuits Conference (ESSCIRC)* 2000, pp. 126-132.

[82] H. Lin and N.-H. Chen, "New four-phase generation circuits for low-voltage charge pumps," in *International Symposium on Circuits and Systems (ISCAS)*, 2001, pp. 504-507 vol. 1.

[83] F. Pan and T. Samadar, *Charge Pump Circuit Design*: McGraw-Hill, 2006.

[84] J.-T. Wu and K.-L. Chang, "MOS charge pumps for low-voltage operation," *IEEE Journal of Solid-State Circuits,* vol. 33, pp. 592-597, 1998.

[85] M.-D. Ker and S.-L. Chen, "Ultra-High-Voltage Charge Pump Circuit in Low-Voltage Bulk CMOS Processes With Polysilicon Diodes," *IEEE Transactions on Circuits and Systems-II: Express Briefs,* vol. 54, pp. 47-51, 2007.

[86] W. C. Huang, P. C. Liou, K. Y. Lin, and J. C. Cheng, "A charge pump circuit by using voltage-doubler as clock scheme," in *IEEE Conference on Industrial Electronics and Applications (ICIEA)*, 2009, pp. 112-116.

[87] K.-H. Choi, J.-M. Park, J.-K. Kim, T.-S. Jung, and K.-D. Suh, "Floating-well Charge Pump Circuits For Sub-2.0V Single Power Supply Flash Memories," in *IEEE Symposium on VLSI Circuits*, 1997, pp. 61-62.

[88] S.-Y. Lai and J.-S. Wang, "A high-efficiency CMOS charge pump circuit," in *International Symposium on Circuits and Systems (ISCAS)*, 2001, pp. 406-409 vol. 4.

[89] R. Pelliconi, D. Iezzi, A. Baroni, M. Pasotti, and P. L. Rolandi, "Power efficient charge pump in deep submicron standard CMOS technology," *IEEE Journal of Solid-State Circuits,* vol. 38, pp. 1068-1071, 2003.

[90] H. Zhili, S. Pourkamali, and F. Ayazi, "VHF single-crystal silicon elliptic bulk-mode capacitive disk resonators-part I: design and modeling," *Journal of Microelectromechanical Systems,* vol. 13, pp. 1043-1053, 2004.

[91] J.-Y. Lee, S.-E. Kim, S.-J. Song, J.-K. Kim, S. Kim, and H.-J. Yoo, "A regulated charge pump with small ripple voltage and fast start-up," *IEEE Journal of Solid-State Circuits,* vol. 41, pp. 425-432, 2006.

[92] L. Jae-Youl, K. Sung-Eun, S. Seong-Jun, K. Jin-Kyung, K. Sunyoung, and Y. Hoi-Jun, "A regulated charge pump with small ripple voltage and fast start-up," *Solid-State Circuits, IEEE Journal of,* vol. 41, pp. 425-432, 2006.

[93] M. Dalal, A. N. Shirazi, W. K. Sung, G. Casinovi, and F. Ayazi, "Novel Readout Scheme for MEMS Vibratory Gyroscopes Based on Signal Phase Shift," presented at the Proc. Solid-State Sens., Actuators Microsyst. Workshop Hilton Head, USA, 2012.

[94] A. A. Seshia, R. T. Howe, and S. Montague, "An integrated microelectromechanical resonant output gyroscope," in *Micro Electro Mechanical Systems, 2002. The Fifteenth IEEE International Conference on*, 2002, pp. 722-726.

[95] G. Casinovi, W. K. Sung, M. Dalal, A. N. Shirazi, and F. Ayazi, "Electrostatic self-calibration of vibratory gyroscopes," in *Micro Electro Mechanical Systems (MEMS), 2012 IEEE 25th International Conference on*, 2012, pp. 559-562.

[96] K. Bauer, M. Aikele, W. Ficker, K. Koppenhagen, F. Neubauer, E. Stenzel, and J. Schalk, "Self-Test for Resonant Structure Sensors Applied to a Tuning Fork Gyro and a Resonant Accelerometer," in *International Solid-State Sensors, Actuators*

and Microsystems Conference (TRANSDUCERS), Munich, Germany, 2001, pp. 468-471.

[97] M. Aikele, K. Bauer, W. Ficker, F. Neubauer, U. Prechtel, J. Schalk, and H. Seidel, "Resonant Accelerometer with Self-Test," *Sensors and Actuators A: Physical,* vol. 92, pp. 161-167, August 2001 2001.

[98] T. Link, I. Simon, M. Trachtler, A. Gaisser, M. Braxmaier, Y. Manoli, and H. Sandmaier, "A new self-test and self-calibration concept for micro-machined gyroscopes," in *Solid-State Sensors, Actuators and Microsystems, 2005. Digest of Technical Papers. TRANSDUCERS '05. The 13th International Conference on*, 2005, pp. 401-404 Vol. 1.

[99] B. J. Gallacher, J. S. Burdess, and A. J. Harris, "Principles of a three-axis vibrating gyroscope," *Aerospace and Electronic Systems, IEEE Transactions on,* vol. 37, pp. 1333-1343, 2001.

[100] W. K. Sung, M. Dalal, and F. Ayazi, "A 3MHz spoke gyroscope with wide bandwidth and large dynamic range," in *Micro Electro Mechanical Systems (MEMS), 2010 IEEE 23rd International Conference on*, 2010, pp. 104-107.

[101] "1.6GHz, Low-Noise, FET-Input Operational Amplifier," Texas Instruments, Dallas, TX, Datasheet OPA657, 2001.

[102] "Wideband, Unity-Gain Stable, FET-Input Operational Amplifier," Texas Instruments, Dallas, TX, Datasheet OPA656, 2002.

[103] "250 MHz, Voltage Output, 4-Quadrant Multiplier," Analog Devices, Inc., Norwood, MA, Datasheet AD835, 2003.

[104] A. Sharma, M. F. Zaman, and F. Ayazi, "A 104-dB Dynamic Range Transimpedance-Based CMOS ASIC for Tuning Fork Microgyroscopes," *IEEE Journal of Solid-State Circuits,* vol. 42, pp. 1790-1802, 2007.

[105] A. Sharma, "CMOS Systems and Circuits for Sub-Degree Per Hour MEMS Gyroscopes," Ph. D, Electrical and Computer Engineering, Georgia Institute of Technology, Atlanta, 2007.

[106] M. F. Zaman, "Degree-per-hour mode-matched micromachined silicon vibratory gyroscopes," Ph. D, Electrical and Computer Engineering, Georgia Institute of Technology, Atlanta, 208.

[107] D. W. Allan, "Statistics of Atomic Frequency Standard," *Proceedings of the IEEE,* vol. 54, pp. 221-231, 1966.

[108] L. Ng, "On the application of Allan variance method for Ring Laser Gyro performance characterization," Livermore, CA 1993.